7-2020

Characterizing peridotite xenoliths from southern Vietnam: insight into the underlying lithospheric mantle

Kirby Hobbs
University of Nebraska - Lincoln, kirhobb@gmail.com

CHARACTERIZING PERIDOTITE XENOLITHS FROM SOUTHERN VIETNAM: INSIGHT INTO THE UNDERLYING LITHOSPHERIC MANTLE

by

Kirby P. Hobbs

A THESIS

Presented to the Faculty of

The Graduate College at the University of Nebraska

In Partial Fulfillment of Requirements

For the Degree of Master of Science

Major: Earth and Atmospheric Sciences

Under the Supervision of Professor Lynne J. Elkins

Lincoln, Nebraska

CHARACTERIZING PERIDOTITE XENOLITHS FROM SOUTHERN VIETNAM: INSIGHT INTO THE UNDERLYING LITHOSPHERIC MANTLE

Kirby P. Hobbs, M.S.

University of Nebraska, 2020

Advisor: Lynne J. Elkins

Extrusion tectonics has been invoked to explain the extensive basaltic magmatism that has erupted over Indochina within the last 17 Ma. The basalts display two-stage eruptive cycles consisting of tholeiites followed by alkaline basalts. Lithospheric mantle xenoliths recently sampled from the alkaline basalts of two volcanic centers, Pleiku and Xuan Loc, primarily consist of fertile spinel lherzolites, and Xuan Loc also contains refractory spinel harzburgites. We measured major elements in xenolith mineral separates, trace elements in clinopyroxenes and orthopyroxenes, and Pb-Sr-Nd isotopic compositions in clinopyroxenes to determine the origin and history of the subcontinental lithospheric mantle (SCLM) beneath Vietnam. Most peridotites from Pleiku and Xuan Loc exhibit fertile major element compositions, “depleted” and “spoon-shaped” rare earth element (REE) patterns, and isotopic signatures ranging from typical depleted MORB mantle to an even more depleted source ($^{87}Sr/^{86}Sr$ = 0.702381 - 0.703365 and ε_{Nd} = +8.84 - +30.28). A smaller group of peridotites from Xuan Loc show distinct refractory major element compositions, “enriched” REE patterns, and more incompatible-element enriched isotopic signatures ($^{87}Sr/^{86}Sr$ = 0.704050 and ε_{Nd} = +3.16 in one

sample) than the fertile peridotites. Based on their major and trace element compositions, Pleiku and Xuan Loc xenoliths have calculated equilibrium temperatures of 807-1052 °C which indicate extraction depths of 30 to 45 km. We interpret the fertile peridotites from Pleiku and Xuan Loc to sample recently emplaced lithospheric mantle from the convecting asthenosphere, whereas the refractory peridotites from Xuan Loc may represent partial melting residues derived from older SCLM. We conclude that the extrusion of Indochina initiated regional asthenospheric upwelling, resulting in the partial removal and replacement of the lithospheric mantle.

Acknowledgements

The completion of my thesis would not have been possible without the support and guidance of my advisor Dr. Lynne Elkins. During my undergraduate, Dr. Elkins inspired my interest in geochemistry and provided me ample opportunity and encouragement to grow and develop as an inspiring researcher. She brought me into the extrusion tectonics project, during which, I worked with amazing group of scientists and was able to develop both my field and laboratory skills. She always made time for her students, no matter how busy she was, and was patient and understanding when I needed help or had questions.

I am also thankful my committee members for providing me with direction with my thesis. Dr. Caroline Burberry was always available to provide insight into the tectonic implications of my research. Dr. Richard Kettler helped sharpen my skills as a geochemist and taught me the importance of explaining my ideas in a clear but concise manner.

I would also like to thank our collaborators Dr. John Lassiter and Dr. Nguyen Hoang. Dr. Lassiter provided me with valuable input throughout my master's degree from sample processing to data interpretation. He also graciously hosted me at UT Austin when doing the geochemical analysis of my samples. I also appreciate the assistance from Dr. Aaron Satkoski, Dr. Staci Loewy, Dr. Nathaniel Miller, and Dr. Omero Orlandini in getting my samples through geochemical analyses during my

visit. I would like to thank Dr. Hoang for hosting us in Vietnam when doing field work and collecting samples.

This research was funded by the National Science Foundation in the form of grant EAR-1758972.

I am thankful for the insight and assistance from the UNITE lab research group students: Yitong Lv, Nick Richard, and Juliet Messer. Finally, I would like to thank my family for their encouragement throughout my academic studies. I couldn't have done this without the love and support of my fiancée, KyRae. She has endured many late nights and frustrations and always manages to brighten up my day while taking care of me.

Table of Contents

1. Introduction 1

2. Background 4

2.1 Geologic Background 4

2.2 Tracking magmatic processes in the SCLM 8

3. Analytical Methods 10

3.1 Electron microprobe analysis 10

3.2 In-situ trace element analysis 11

3.3 Sr-Nd-Pb isotope geochemistry 12

4. Results 14

4.1 Petrology 14

4.2 Major elements 15

4.3 Trace elements 18

4.4 Sr-Nd-Pb isotopes 25

4.5 Thermometry and barometry 30

5. Discussion 33

5.1 History of magmatic processes beneath Indochina 33

5.1.1 Extent of partial melting 34

5.1.2 Metasomatism of the SCLM beneath Vietnam 40

5.2 Thermal state of the SCLM and equilibration depths of Vietnam xenoliths 45

5.4 Implications for extrusion tectonics 48

5.5 Working model for the SCLM beneath Vietnam 49

6. Conclusions 50

7. References 52

APPENDIX A. Mineral Major Element Data 64

APPENDIX B. Clinopyroxene and Orthopyroxene Trace Element Data 77

APPENDIX C. T_{REE} Inversion Diagrams 84

List of Tables

Table 1. Table of Sr-Nd-Pb isotopic compositions of Vietnam xenoliths 27

Table 2. Table of equilibrium temperatures and pressures..... 32

List of Figures

Figure 1. Diagram of extrusion due to the Indo-Eurasia collision..... 3

Figure 2. Map of study area and sample collection localities..... 7

Figure 3. Fertile versus refractory samples types..... 15

Figure 4. Compositional variation between clinopyroxene rims and cores 17

Figure 5. Clinopyroxene trace element spider diagrams 20

Figure 6. Orthopyroxene trace element spider diagram..... 24

Figure 7. Pb isotope compositions of clinopyroxenes 28

Figure 8. Sr versus Pb and Nd isotopic compositions of clinopyroxenes..... 29

Figure 9. Comparison of calculated equilibrium temperatures 33

Figure 10. Major elements as a proxy for melt depletion 38

Figure 11. Extents of partial melting determined from spinel Cr#..... 39

Figure 12. Plots of spinel Cr# versus titanium and Nd isotopes versus trace element ratios 44

Figure 13. Model of the geothermal gradients below Pleiku and Xuan Loc..... 47

Figure 14. Diagram of lithospheric erosion beneath Vietnam..... 50

1. Introduction

The diffuse igneous province of Indochina is a collision-adjacent, complex tectonic region with extensive basaltic magmatism (Hoang et al., 1996; Hoang and Flower, 1998). The Vietnamese plateau basalts record two-stage eruptive cycles starting at ~17 Ma and consist of large volumes of tholeiites followed by smaller quantities of alkaline basalts, many of which host lithospheric mantle xenoliths. Prior geochemical analysis of basalts has included major element, trace element, and Sr-Nd-Pb isotopes and suggests that early-stage tholeiitic volcanism records contributions from a subcontinental lithospheric mantle (SCLM) source while later-stage volcanism reflects an asthenospheric source (Hoang et al., 1996, Hoang and Flower, 1998). Hoang et al. (2013) suggests that the early-stage volcanism may have been enriched by crustal assimilation. Traditional tectonic regimes of mantle upwelling, such as regional extension, do not adequately explain the observed abundance (70,000 km^2) of volcanism (Hoang and Flower, 1998). Previous studies have proposed a role for extrusion tectonics, positing that the adjacent Himalayan collision extruded Southeast Asia eastward and caused mantle upwelling beneath Indochina (Fig. 1) (Hoang et al., 1996; 2013; Flower et al., 1998; Hoang and Flower, 1998; Jolivet et al., 2018). However, the origin and character of the mantle upwelling has not been well explained.

Lithospheric mantle xenoliths provide a chance to constrain the depth, temperature, and composition of local SCLM. Subcontinental lithospheric mantle is typically an ancient, cold layer variably enriched in trace elements that separates

the continental crust from the convecting asthenosphere (McDonough, 1990). Mantle lithospheric xenoliths are typically thought to represent the SCLM or recently emplaced asthenosphere and may track magmatic processes such as partial melting, melt enrichment, and metasomatic events. Diffusion of major and trace elements can be used to calculate the temperature and pressure of the underlying SCLM (Brey and Kohler, 1990; Ballhaus et al., 1991; Liermann and Ganguly, 2003; Putirka, 2008; Liang et al., 2013). Mantle xenoliths thus provide a "window" into the SCLM, and by characterizing the SCLM spatially and temporally, we can further constrain the mantle dynamics and provide more realistic tectonic models.

To date, mantle xenoliths from Vietnam have not been adequately studied to achieve such constraints on regional tectonics and dynamics. One study in central Vietnam (the Pleiku volcanic center) by Nguyen and Kil (2019) has suggested that the mantle beneath Indochina has experienced a prior melt depletion event and various chemical re-enrichment processes. Based on their major element data, Pleiku lithospheric mantle xenoliths from Vietnam have calculated equilibrium temperatures ranging from 841-1131ºC and may have experienced 1-20% fractional melting (Nguyen and Kil, 2019). The current study expands this previously limited dataset and further characterizes the SCLM using measured major/trace elements and Sr-Nd-Pb isotopic compositions in xenoliths collected from the Pleiku and Xuan Loc volcanic centers, comprising a total of 25 spinel peridotite samples. The three objectives of this study are to: (1) track magmatic processes in local SCLM; (2) compare the SCLM sampled by xenoliths at two sites in

Vietnam to characterize its spatial variability (Pleiku and Xuan Loc); and (3) constrain mantle evolution beneath an extruding Indochina.

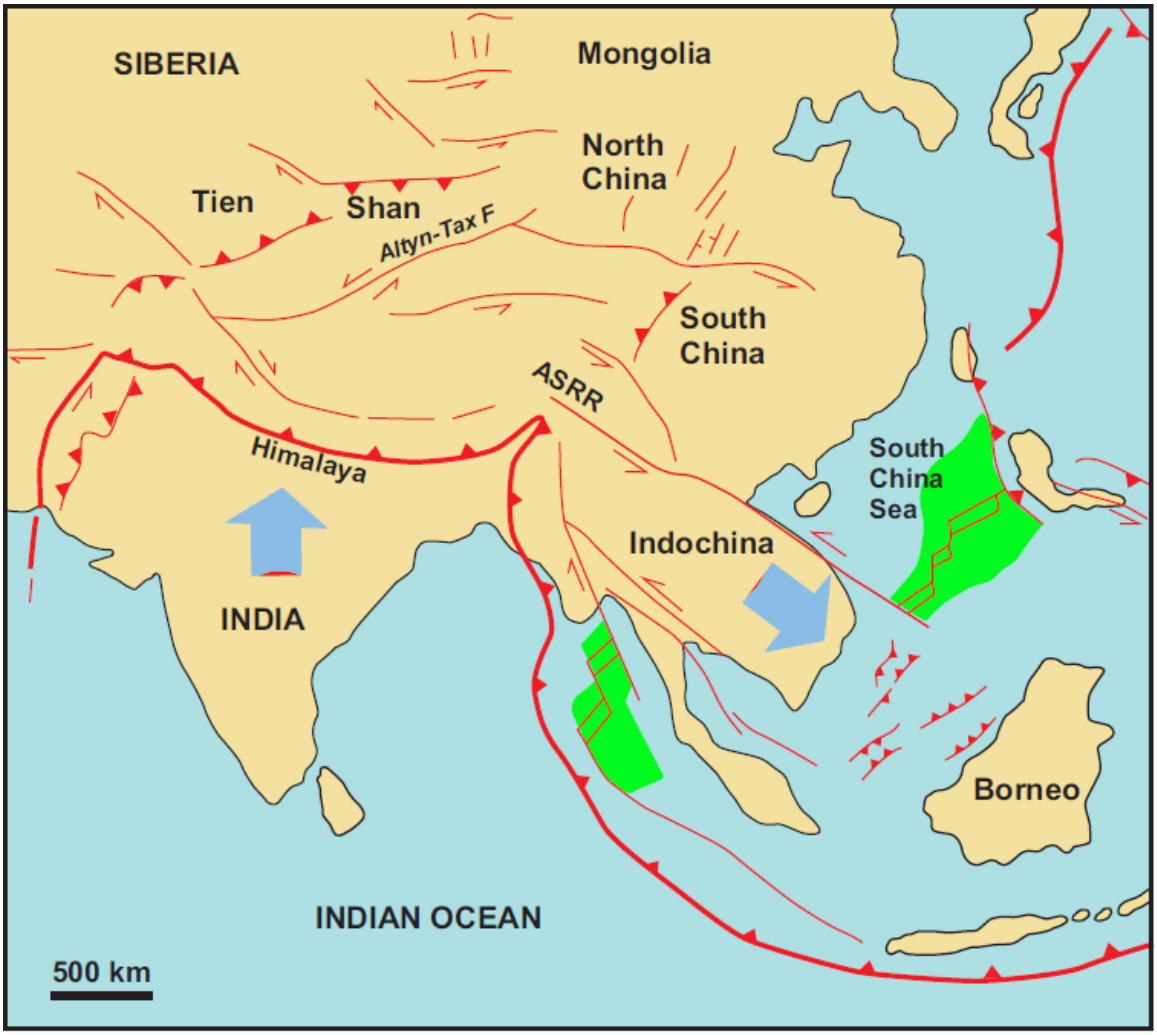

Figure 1. Extrusion of Indochina due to the India-Eurasia collision (Phach and Anh, 2018). ASRR = Ailao Shan-Red River Fault Zone.

2. Background

2.1 Geologic Background

Indochina was rifted from Gondwana and then was sutured to Asia during the closure of a series of Tethyan ocean basins in the Permian and Triassic (Metcalfe, 2013). Subsequent subduction-related magmatism occurred over Indochina during the Cretaceous as a result of northward subduction of the Tethyan seafloor, emplacing Cordilleran-type granitic batholiths (Shellnutt et al., 2013; Gibbons et al., 2015). The initial collision of Indian continental lithosphere with Eurasia occurred at ~50 Ma in the Miocene (Gibbons et al., 2015). The continued movement of the Indian block northward (~3000 km) after the initial continental collision led to the onset of extrusion tectonics in Asia, which is thought to have occurred before 35 Ma (Royden et al., 2008; Rohrmann et al., 2012). The extrusion and clockwise rotation of Indochina occurred as left-lateral movement along large-scale transform faults (Fig. 1) (e.g., Ailao Shan-Red River Fault Zone, Mae Ping Fault Zone) until ~17 Ma, when motion along the transform faults became right-lateral concurrent with the cessation of South China Sea rifting (Zhu et al., 2009; Li et al., 2015). This reconfiguration event was followed by the onset of diffuse volcanic activity in Indochina at ~17 Ma, which has continued through the Holocene and peaked within the last three million years (Hoang et al., 1996; Hoang and Flower, 1998). The dominant driving mechanism of the anomalous Cenozoic basaltic magmatism across Indochina has previously been attributed to either extrusion tectonics or extension tectonics (Flower et al., 1998; Hoang and Flower, 1998;

Cullen et al., 2010). The extrusion tectonic model was applied to Indochina Cenozoic volcanism as an explanation for the sequence of 1) early-stage tholeiites, thought to be partial melts sourced from melting of refractory SCLM due to upwelling asthenosphere, followed by 2) alkali basalts, thought to be partial melts sourced from the decompressing asthenosphere.

The basaltic plateaus across central and southern Vietnam cover an area of 23,000 km^2 and have an estimated volume of ~8,000 km^3 (Hoang and Flower, 1998). The Pleiku basaltic plateau (Fig. 2) covers an area of ~4,000 km^2 and is characterized by the two-stage eruptive cycle typical of most eruptive centers in southern Vietnam (Hoang and Flower, 1998; Hoang et al., 2013). The Xuan Loc basalts (Fig. 2) are younger (5.0 - 0.3 Ma) than the Pleiku basalts (6.5-0.2 Ma) and cover an area of ~2400 km^2 (Hoang et al., 2013). The earlier stage eruptives at both localities consist of quartz and olivine tholeiites (with high SiO_2 (48-55 wt%) and low FeO (8-10.5 wt%)) and have been dated at Pleiku from 6.5-3.4 Ma using Ar/Ar methods (Hoang et al., 1996, 2013; Hoang and Flower, 1998). In both locations, tholeiites are overlain by smaller eruptions of predominantly alkali basalts (with relatively low SiO_2 (40-50 wt%) and high FeO (9-14.5 wt%)) that have been dated at Pleiku from 2.4-0.2 Ma (Hoang et al., 1996, 2013; Hoang and Flower, 1998). Alkali basalts from both volcanic plateaus host numerous mantle-derived xenoliths including garnet lherzolites, spinel lherzolites, spinel harzburgites, wehrlites, websterites, and pyroxenites (Hoang and Flower, 1998; Hoang et al., 2013). Basalts from both localities have $^{206}Pb/^{204}Pb$, $^{207}Pb/^{204}Pb$, $^{208}Pb/^{204}Pb$, $^{87}Sr/^{86}Sr$, and ε_{Nd}

that plot from the Indian MORB field towards an enriched mantle 2 (EM2) composition (where "enriched" refers to elevated time-integrated incompatible element concentrations recorded as relatively high $^{206}Pb/^{204}Pb$, $^{207}Pb/^{204}Pb$, $^{208}Pb/^{204}Pb$, $^{87}Sr/^{86}Sr$ and low ε_{Nd}), with slightly more enriched isotopic compositions in Pleiku basalts relative to Xuan Loc; more silica-rich basalts (i.e., quartz and olivine tholeiites) likewise exhibit more enriched isotopic compositions relative to silica-poor basalts (alkali basalts) (Hoang et al., 1996, 2013).

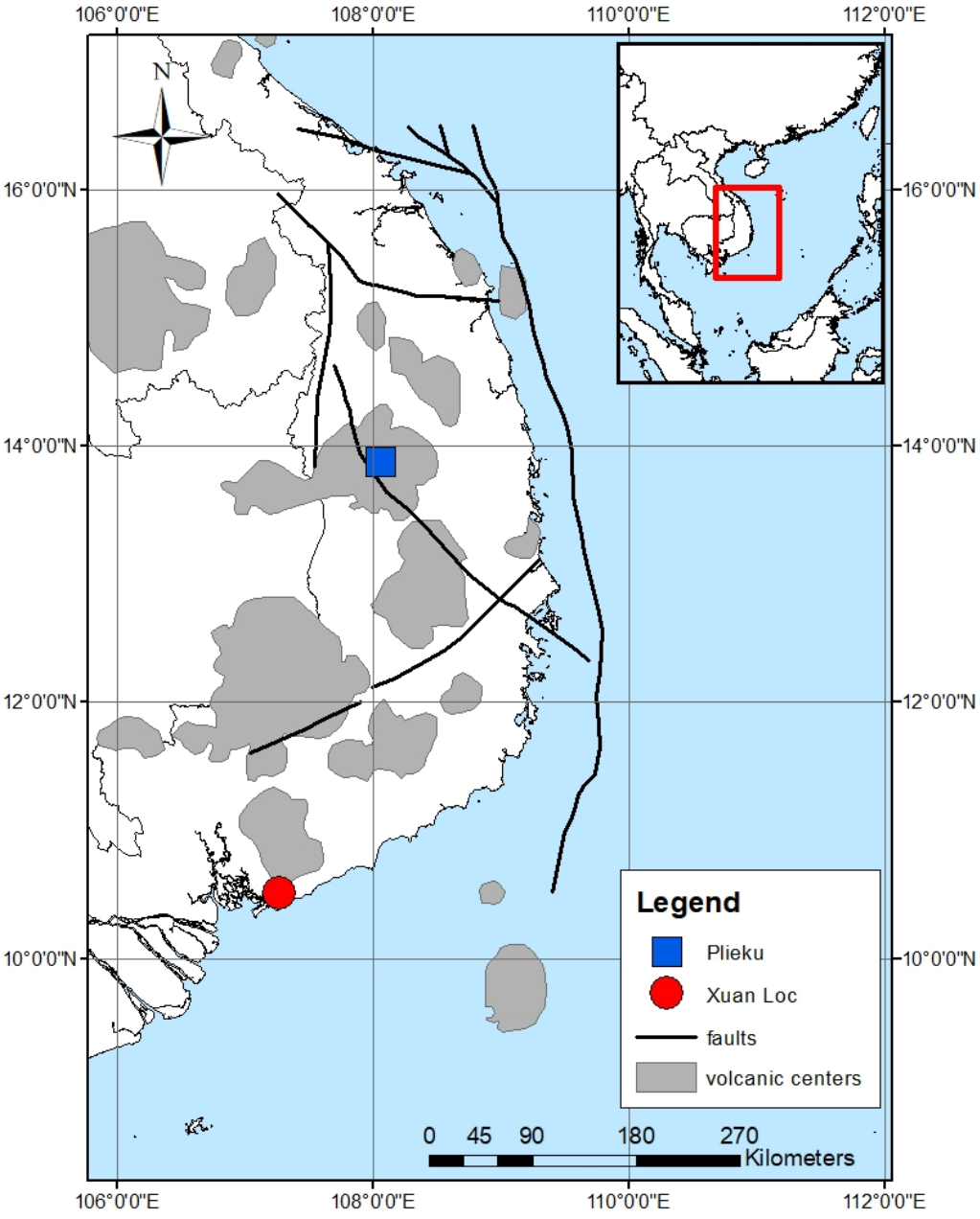

Figure 2. Map of study area and sample collection localities. Major mapped faults and volcanic centers are modified from published literature (Hoang et al., 2013; Phach and Anh, 2018).

2.2 Tracking magmatic processes in the SCLM

The compositions of mantle xenoliths provide insight into magmatic processes that have affected the local lithospheric mantle, such as the nature of prior melt extraction (e.g., the degree of melting). During partial melting and melt extraction, incompatible elements are preferentially distributed into the melt, leaving residual peridotites depleted in these elements and where the relative degree of each element's depletion strongly correlates with its incompatibility in residual minerals (Frey and Green, 1974; Michael and Bonatti, 1985). Melting models can help to relate the incompatible element concentrations of the residual rock to the degree of prior melting. The evolution of the solid composition in response to melting can also vary significantly depending on the type of melting assumed (e.g., fractional or batch melting). The fractional melting model assumes that each infinitesimal increment of melt is produced and instantaneously removed from the system, whereas in batch melting the residue and melt are in chemical equilibrium throughout the melting process. To apply these methods to the study of residual rocks, Johnson et al. (1990) revised the basic melting equations of Gast (1968) and Shaw (1970) to describe melting as the change of element concentration in clinopyroxene (cpx) during melting of mantle peridotites, because cpx hosts the highest concentrations of trace elements and is therefore typically analyzed for empirical concentration measurements. They suggested that the extreme fractionation of rare earth elements (REE) in cpx in mantle peridotites could only be achieved by realistic degrees of near fractional melting (Johnson et al., 1990).

Metasomatism is an additional process that occurs when an external fluid component is brought into the system and causes the enrichment of incompatible elements in the affected rock through fluid-rock chemical interactions and reequilibration. Metasomatic agents can be magmas or volatile-rich aqueous and carbonitic fluids. Typically, metasomatism is classified as "modal" when the metasomatic agent introduces new phases (i.e., precipitates new minerals along reactive pathways) and "cryptic" when metasomatism is only recorded in trace element compositions (Dawson, 1984). Tracking the characteristics (e.g., source, timing, and melt/fluid compositions) of metasomatism is complicated due to possible overprinting of previous magmatic events and the multiple processes that control elemental fractionation mechanisms (Ionov, 2002). The composition of the metasomatic agent is one of the main controlling factors over observed variations in trace elements in the host rock, as the external fluid may be enriched in some incompatible elements but not others. Variable metasomatic enrichment can also be the product of chromatographic fractionation of elements with time and distance from the chromatographic "column" (e.g., interstitial fluid-filled veins in peridotites) and may also preferentially re-enrich harzburgites over lherzolites in trace elements (Toramaru and Fujii, 1986; Navon and Stolper, 1987). From modelling results, Ionov et al. (2002) found that chromatographic fractionation effects can cause a large range of trace element patterns in host rocks during a single metasomatic event, and that the location of a mineral/rock within this "column" determines whether the trace element patterns produced are primarily controlled by the composition of the

metasomatic agent or by trace element fractionation between coexisting phases. While this system is complex, we can still use the relative enrichment or depletion of elements interpreted from REE patterns and isotopic compositions (i.e., the time-integrated incompatible element concentrations) to better understand the magmatic history of the SCLM.

3. Analytical Methods

3.1 Electron microprobe analysis

The analytical techniques for this study were conducted at the University of Texas at Austin. Major elements for spinel (sp), orthopyroxene (opx), cpx, and olivine (ol) were measured on mineral separates in epoxy mounts with a JEOL JXA-8200 electron microprobe analyzer (EPMA) that uses wavelength dispersive spectrometry (WDS). Generally, at least one core and rim measurement was analyzed per grain and five grains were measured for each sample. Spot size was a diameter of 2 μm with a beam voltage of 15 kV and current of 50 nA. Elemental concentrations were acquired using Kα peak signals with analyzing crystal detectors and were assigned as follows: LiFH – Mn, Ti, Cr; LiF – Fe, Ni; PETH – Ca; TAP – Na, Mg, Al, Si. The on-peak count times were variable for elements in each mineral (40-120 s on-peak with equal time spent measuring background signals) and correspond to expected element concentrations, with minor elements having longer count times than major elements. The off-peak correction method was linear

for all elements in ol and opx (except Ti, for which we used an exponential correction in ol). Spinel was calibrated using the mean atomic number (MAN) background intensity calibration curve. For cpx we conducted the measurements across two rounds, one using the linear off-peak correction method and the other using the MAN background intensity calibration curve. Natural and synthetic crystalline solids with known major element compositions were used as standards, and the matrix corrections used were ZAF and $\phi(\rho Z)$ (Armstrong, 1988). Average calculated major element concentrations have standard deviations commonly within 5% (Appendix 1).

3.2 In-situ trace element analysis

Trace element measurements were performed for the same cpx and opx epoxy mounts prepared for major element analysis, using an Agilent 7500ce inductively-coupled plasma mass spectrometer (LA-ICP-MS) with a NWR193-FX laser ablation system. The analytical spot size was a diameter of 150 μm to increase the signal intensity of the low trace element concentrations in opx and overlapped the EPMA spot locations. Samples were pre-ablated, with a dwell time of 60 s and washout time of 30 s. The Si wt.% from the EPMA measurements was used as the internal standard, NIST 612 was used as the primary analytical standard, and NIST 610, BHVO-2G, and NIST 616 were used as secondary standards. Analysis of NIST 610 and BHVO2G for all elements was generally within 5% of accepted values (for

NIST 610, [Tm] was < 10 %; for BHVO2G, [Na] and [Nd] were within <10% and [Ca] and [Pb] were <20%). Results of NIST 616 analysis for all elements were within 10 % of expected values, except for elements with concentrations near detection limits (i.e., Nd, Gd, Dy, Ho, and Er, which were within 20 % of expected values). [Ti] and [Yb] for NIST 616, however, did not agree with expected values within 20%. NIST 610 concentrations are reproducible in all elements to within 5% (2σ) (Appendix 2).

3.3 Sr-Nd-Pb isotope geochemistry

Strontium, Nd, and Pb isotopes were measured in cpx separates. After hand-picking, the cpx separates were leached using a 2 N HCl solution in an ultrasonic bath for 5 minutes to remove surface coatings. 100 mg of separates from each sample were then dissolved in 5 mL concentrated HF and 1 mL concentrated HNO_3 in an oven at 105°C. After the initial dissolution, the samples were dried and then dissolved in 6 N HCl in an oven at 105°C. The samples were dissolved in HCl + HBr and passed through AG 1-X8 anion exchange resin to separate Pb. The washes containing Sr and Nd were then dried down and redissolved in HNO_3. The samples were passed through Sr-Spec resin to separate Sr followed by RE-Spec resin to separate the rare earth elements. Finally, the rare earth portions were converted to a HCl solution and passed through LN-Spec resin to separate Nd from other REE (procedures after Lassiter et al., 2003).

Lead isotopes were measured using a Nu Plasma 3D multi-collector ICP-MS. Lead separates were diluted to concentrations of 10 ppb in 2% HNO_3 and doped with 2 ppb Tl for pseudo-internal standard normalization. ^{203}Tl and ^{205}Tl were used to correct for mass fractionation of Pb and Hg isotopes using an exponential law. NBS 981 was used for standard-sample-bracketing to correct for analytical drift using the accepted values of $^{206}Pb/^{204}Pb$ = 16.9405, $^{207}Pb/^{204}Pb$ = 15.4967, and $^{208}Pb/^{204}Pb$ = 36.7220. Standard-sample-bracketing consists of standard runs before and after each unknown or secondary standard and is used to linearly interpolate analytical drift of unknown samples using the inferred drift from the standard runs. BCR-2 and BHVO-2 were used as secondary standards and were measured within 0.21% of accepted values (Table 1). Five samples with low Pb concentrations were additionally diluted to a concentration of 0.25 ppb and analyzed using a multi-Daly detector array.

Strontium and Nd isotopes were measured using a Triton thermal ionization mass spectrometer as metals precipitated on Re filaments. We measured NBS 987 $^{87}Sr/^{86}Sr$ = 0.701254 ± 0.000009 (2σ; n=33). BCR-2 and BHVO-2 were measured as secondary standards and are within 0.000008 of accepted values (Table 1). The Nd standard is JNdi-1 and we measured a $^{143}Nd/^{144}Nd$ ratio of 0.512114 ± 0.000013 (2σ; n=15). The cpx separates generally contained 2.5-50 ng of Pb, 1,000-10,000 ng of Sr, and 100-1,000 ng of Nd making the impact of the procedural blanks (<130 pg Pb; <140 pg Sr; < 200 pg Nd) negligible.

4. Results

4.1 Petrology

Mantle peridotite xenoliths from Pleiku and Xuan Loc are classified as group-1 xenoliths based on the classification scheme by Frey and Prinz (1978) and consist of sp, cpx, opx, and ol (Fig. 3). By definition, group-1 xenoliths are typically lherzolites, harzburgites, and dunites that contain Cr-rich, Al_2O_3-poor and TiO_2-poor sp and pyroxenes (Frey and Prinz, 1978). All samples from Pleiku for this study are lherzolites; however the Pleiku basaltic plateau has also produced harzburgite and dunite xenoliths (Hoang et al., 2013; Nguyen and Kil, 2019). Xuan Loc samples are more diverse, containing lherzolites, harzburgites, and dunites. Sample XL-1 is a dunite and only contains ol with minor cpx and sp. Samples have been further subdivided into two groups based on sp Cr# (molar Cr / (Al + Cr)) after methods from Byerly and Lassiter (2012). Type-F (fertile) samples have a sp Cr# <0.25 and type-R (refractory) samples have sp Cr# ≥0.25, where the relative "fertility" of the peridotite refers to how readily and productively it generates magma upon partial melting (Fig. 3). Based on this Cr# definition, Pleiku samples from this study are all type-F peridotites, while Xuan Loc samples are both type-F and type-R peridotites.

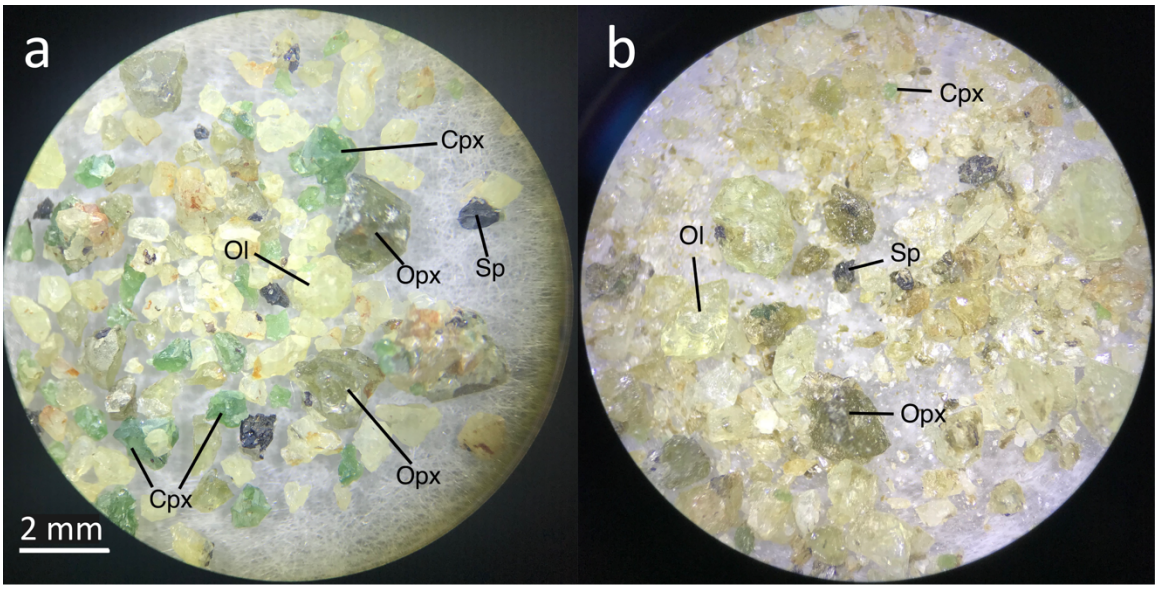

Figure 3. Olivine (Ol), orthopyroxene (Opx) clinopyroxene (Cpx), and spinel (Sp) mineral separates of a) a fertile sample (PL-2) and b) a refractory sample (XL-12). Fertile samples have higher modal cpx and, therefore, have higher potential to generate melting. Refractory samples have lower modal cpx, likely due to previous melt extraction.

4.2 Major elements

Major element data for ol, opx, cpx, and sp mineral separates from Pleiku and Xuan Loc peridotites are given in Appendix A. Clinopyroxene and opx display variations between rim and core measurements in all samples except PL-5 and XL-11. The core-to-rim variation is present across all localities and sample types (Fig. 4). Clinopyroxene Al_2O_3 and Cr_2O_3 concentrations are lower in the rims by ~0.2 to 1.0 wt % and ~0.1 to 0.2 wt %, respectively. Similarly, opx grains have rims that are lower by ~0.1 to 0.6 wt % in Al_2O_3 and by up to 0.1 wt % in Cr_2O_3. Samples PL-1 and XL-14 also display rims with slightly higher CaO (0.75 wt % and 0.94 wt %,

respectively). Due to this variation, average core and rim compositions of each mineral are presented as separate data sets (Appendix A). Averaged core measurements are expected to best preserve the compositions of the peridotites prior to entrainment and exhumation and, thus, have been used to characterize the SCLM.

The Mg# (molar Mg / (Mg + Fe^{2+})) of ol from Pleiku and Xuan Loc xenoliths are between 0.86 and 0.92 (Appendix A), which lies within the compositional range of SCLM (Arai, 1994). Lherzolites have overlapping but slightly higher ol Mg# (0.89-0.92) than harzburgites and dunites (0.86-0.91). Olivine Mg# correlates with cpx Mg#, opx Mg#, and sp Cr#. The CaO content of ol is less than 0.06 wt% and NiO is between 0.3 to 0.42 wt % for all samples.

We find that sp compositions are highly variable across Vietnam peridotites. Spinel grains in lherzolites have Al_2O_3 and MgO ranges of 52.86 to 60.04 wt% and 19.28 to 20.88 wt%, respectively. Harzburgite and dunite samples have lower Al_2O_3 (32.32-34.56 wt%) and lower MgO (12.95-16.70 wt%) than lherzolites. One dunite sample, XL-1, has notably higher FeO (26.10 wt%) and lower Al_2O_3 (23.98 wt%) than the other refractory, i.e., harzburgite and dunite samples (13.50 wt. % and 33.08 wt. %, respectively). Spinel Cr# for the lherzolites (0.08-0.17) and harzburgites/dunites (0.40-0.50) all lie within the compositional range previously documented for SCLM-derived xenoliths (Arai, 1994).

Lherzolites from Pleiku and Xuan Loc have cpx with high Al_2O_3 (5.52-7.2 wt%), low Cr# (0.06-0.13), and high Na_2O (1.18-1.93 wt%). Clinopyroxene grains from harzburgites generally exhibit comparatively low Al_2O_3 (1.72-3.15 wt%), high Cr# (0.20-0.25), and high Na_2O (1.18-1.93 wt%). Orthopyroxene displays a similar trend to cpx, with lherzolite-hosted grains exhibiting high Al_2O_3 (3.39-4.43 wt%) and low Cr# (0.04-0.98 wt%), while opx in harzburgites exhibits relatively low Al_2O_3 (1.86-2.16 wt%) and high Cr# (0.11-0.14).

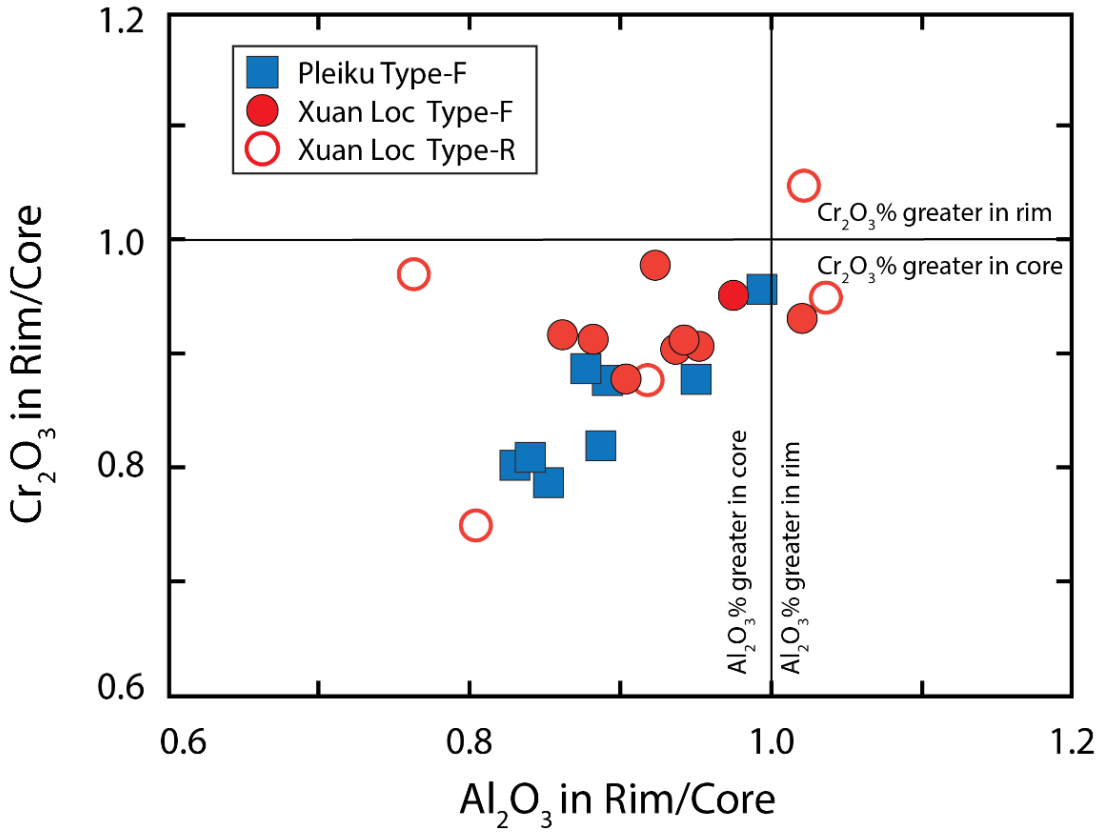

Figure 4. Clinopyroxene Al_2O_3 rim/core ratio versus cpx Cr_2O_3 rim/core ratio.

4.3 Trace elements

Average trace element data for cpx and opx from Pleiku and Xuan Loc peridotites are given in Appendix B. The primitive mantle normalized trace element concentrations and REE patterns (REE_{PM}) for cpx are shown in Fig. 5. Type-F cpx from Pleiku and Xuan Loc display depleted and spoon-shaped REE_{PM} patterns. The "depleted" and "spoon-shaped" patterns for Pleiku xenoliths are generally more steeply sloped than those for Xuan Loc samples, with a median $(Ce/Yb)_{PM}$ of 0.17 for Pleiku versus 0.51 for Xuan Loc. All type-F xenoliths have a relatively flat slope from the middle rare earth elements (MREE) to heavy rare earth elements (HREE), with Pleiku and Xuan Loc having $(Sm/Yb)_{PM}$ from 0.53 to 1.04 and 0.60 to 1.22, respectively. "Depleted" patterns show a positive steep slope from LREEs to light rare earth elements (MREE) with Pleiku and Xuan Loc showing $(La/Sm)_{PM}$ from 0.10 to 0.14 and 0.33 to 0.61, respectfully. "Spoon-shaped" patterns are similar, but also exhibit a LREE enrichment with $(La/Ce)_{PM}$ 1.08 to 1.79 (Pleiku) and 1.22 and 1.38 (Xuan Loc). XL-8 has an "enriched" REE_{PM} pattern exhibiting a negative slope from LREE to MREE ($(La/Sm)_{PM}$ = 1.55).

The Type-R cpx have enriched REE_{PM} patterns and, in this study, are only present in the Xuan Loc suite of samples but similar REE patterns are exhibited by the published refractory samples from Pleiku (Fig. 5a) (Nguyen and Kil, 2019). Clinopyroxenes from the refractory xenoliths have elevated LREE and low HREE with steep negative slopes from LREEs to HREEs. These enriched patterns exhibit $(Ce/Yb)_{PM}$ from 6.14 to 9.15. Clinopyroxene from sample XL-1 has an S-shaped

REE_{PM} pattern and a positive slope from the MREEs to HREEs but has $(La/Sm)_{PM}$ of 0.71.

Additional trace element compositions show that incompatible elements in cpx (Rb, Nb, Pb, Sr, Ti) are fractionated from the surrounding REE (Fig. 5). Rubidium in cpx is depleted in almost all samples, with concentrations near or below analytical detection limits. Titanium, Pb, and Nb display negative anomalies across all samples compared to neighboring REE (Fig. 5). Sample PL-2 has a steep negative slope from U_{PM} to Pb_{PM}. Strontium is variably enriched and depleted when compared to surrounding REE_{PM}, with high-Sr samples roughly correlating with the spoon-shaped REE_{PM} patterns.

Orthopyroxenes display REE_{PM} patterns that strongly correlate with cpx patterns (Fig. 6). Type-F opx have REE_{PM} that exhibit depleted and spoon-shaped patterns. Some samples have opx LREEs that are near or below analytical detection limits. Type-R opx have convex downward REE_{PM} patterns with a negative slope from LREE to MREE and a positive slope from MREE to HREE. Moderately incompatible elements (Ti, Zr, and Hf) have positive anomalies relative to REE. The Lu/Hf ratios in opx are systematically higher by a factor of 3.8 than those in coexisting cpx.

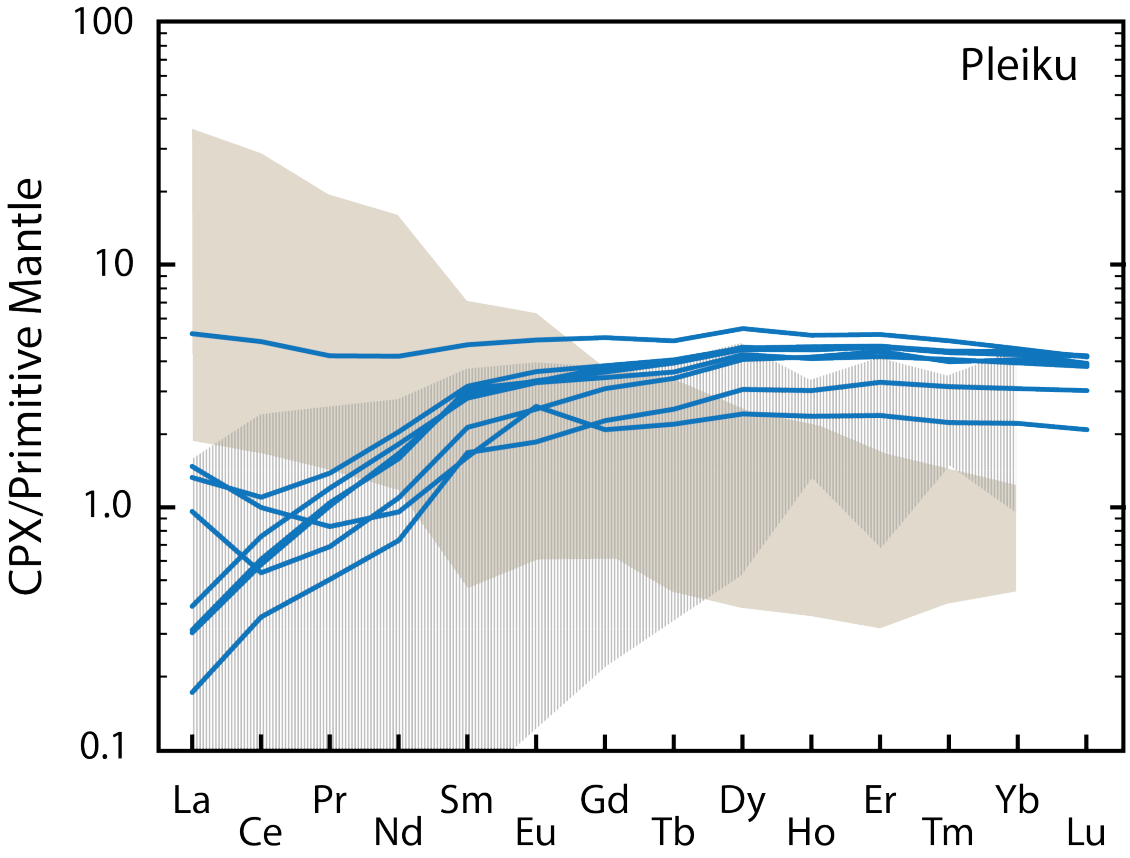

Figure 5a. Clinopyroxene rare earth element concentrations of Pleiku peridotites (blue lines) normalized to primitive mantle (Sun and McDonough, 1989) The tan field shows Type-R sp harzburgites from Pleiku (Nguyen and Kil, 2019) and the grey field is the range of cpx compositions in abyssal peridotites (Warren, 2016).

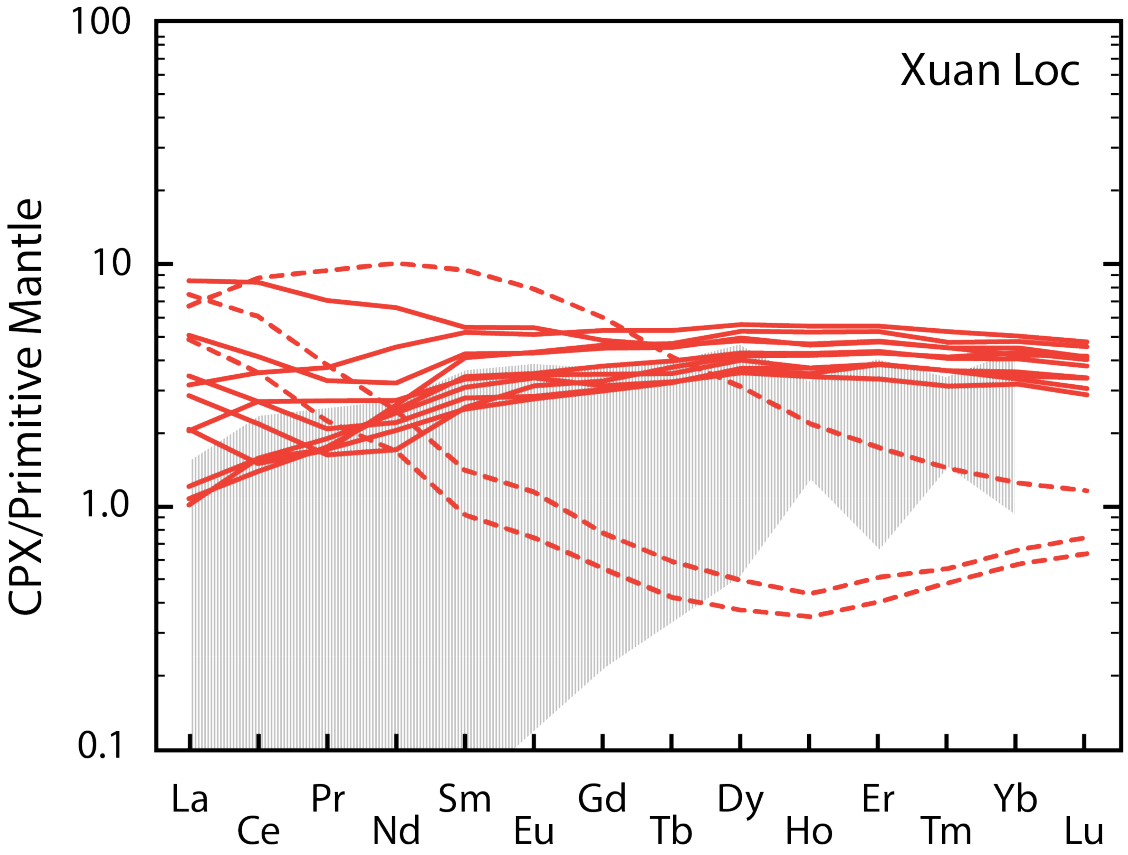

Figure 5b. Clinopyroxene rare earth element concentrations of Xuan Loc peridotites normalized to primitive mantle (Sun and McDonough, 1989). Type-R peridotites are shown by red dashed lines and Type-F peridotites are shown by solid red lines. The grey field is the range of cpx compositions in abyssal peridotites (Warren, 2016).

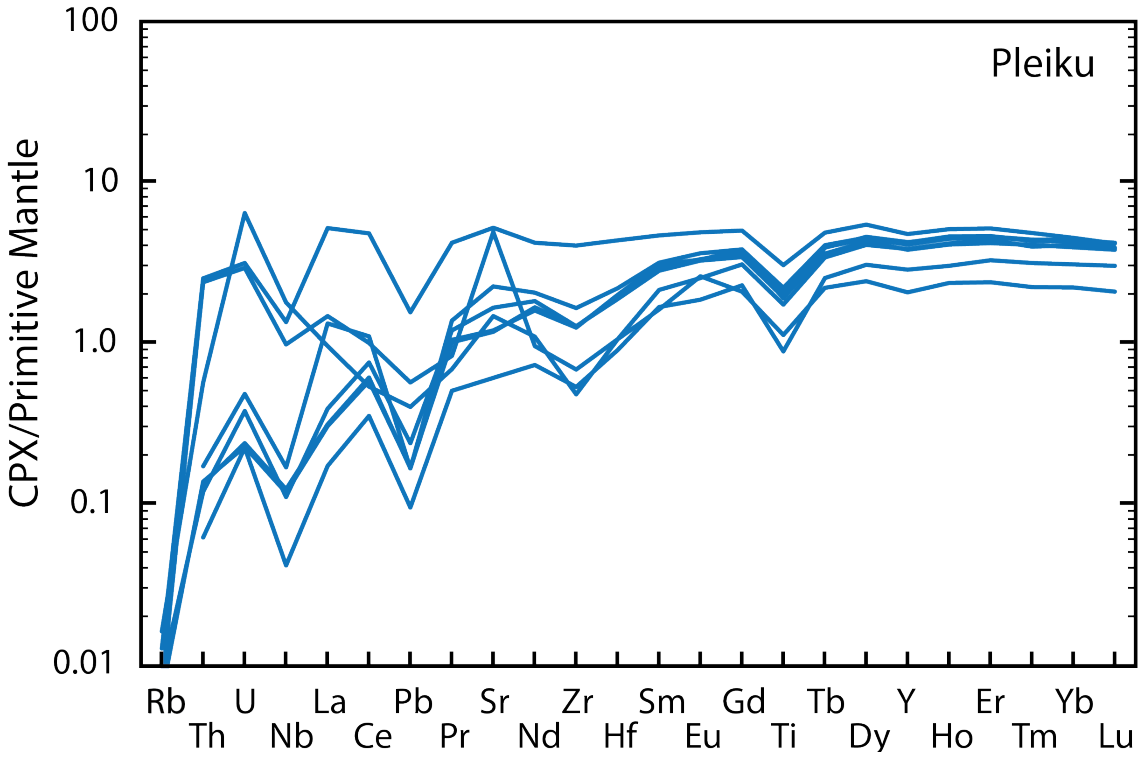

Figure 5c. Clinopyroxene trace element concentrations of Pleiku peridotites normalized to primitive mantle (Sun and McDonough, 1989).

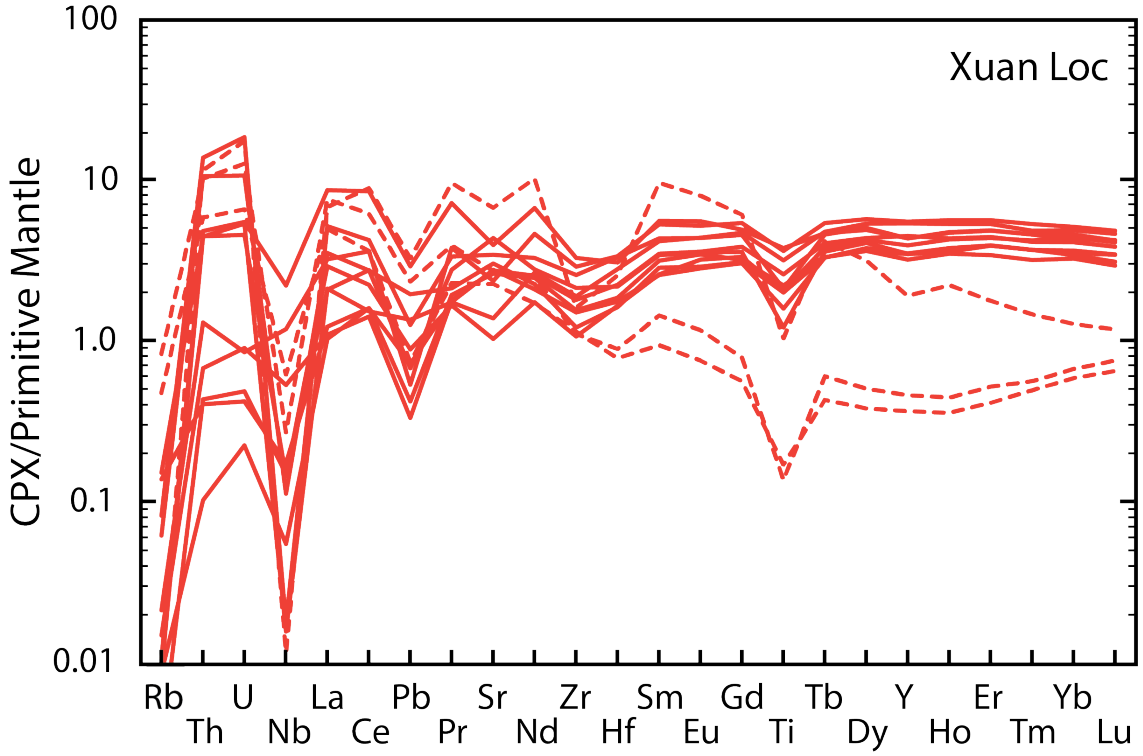

Figure 5d. Clinopyroxene trace element concentrations of Xuan Loc peridotites normalized to primitive mantle (Sun and McDonough, 1989). Type-R peridotites are shown by red dashed lines and Type-F peridotites are shown by solid red lines.

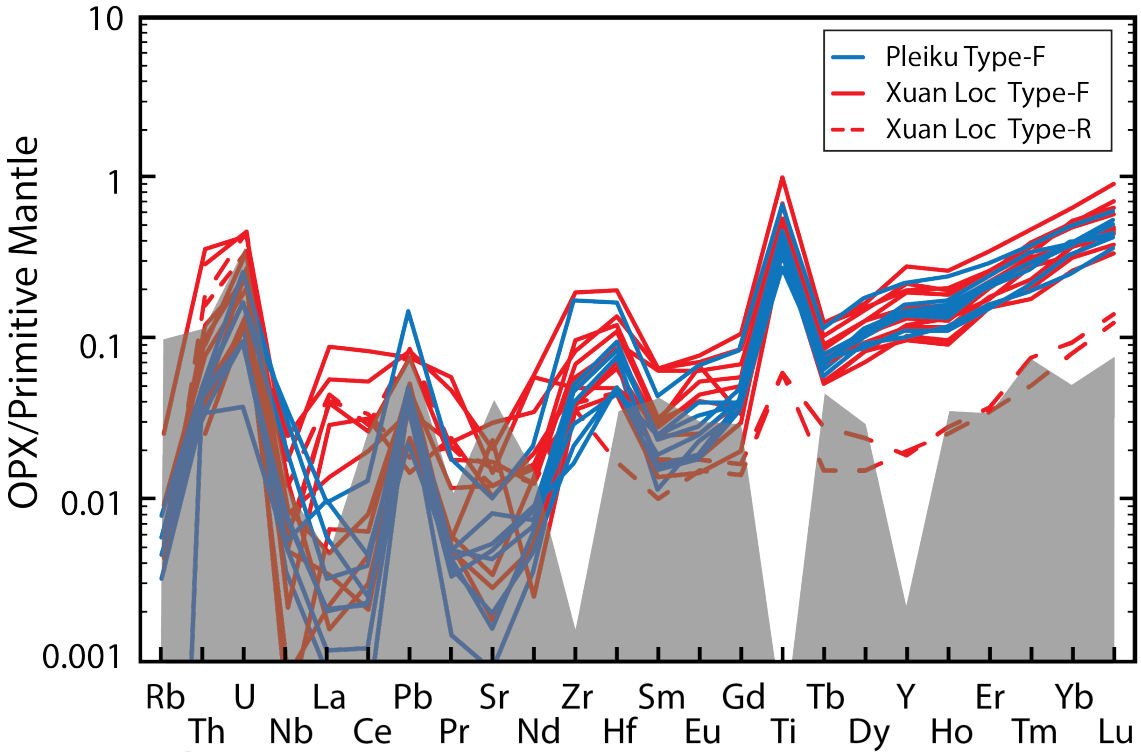

Figure 6. Orthopyroxene trace element concentrations of Pleiku and Xuan Loc peridotites normalized to primitive mantle (Sun and McDonough, 1989). The grey field represents the detection limits for each element.

4.4 Sr-Nd-Pb isotopes

The Sr, Nd, and Pb isotopic compositions of cpx mineral separates from Pleiku and Xuan Loc are given in Table 1 and Figures 7 and 8. Samples PL-1, PL-3, and PL-6 contained <2 ng of Pb, which is near analytical detection limits, and thus will not be used for interpretation. Clinopyroxene from Pleiku lherzolites exhibit highly variable isotopic compositions: $^{206}Pb/^{204}Pb$ = 17.39-18.86, $^{207}Pb/^{204}Pb$ = 15.48-15.58, $^{208}Pb/^{204}Pb$ = 37.30–38.85, $^{87}Sr/^{86}Sr$ = 0.702381-0.703365, and ε_{Nd} = +8.84 - +30.28 ($^{143}Nd/^{144}Nd$ = 0.513091-0.514190) (Fig. 7; 8). Where ε_{Nd} describes $^{143}Nd/^{144}Nd$ in terms of the deviation from the chondritic uniform reservoir (CHUR) evolution line:

$$\varepsilon_{Nd} = \left[\frac{\left({}^{143}Nd/{}_{144}Nd \right)_{sample}}{\left({}^{143}Nd/{}_{144}Nd \right)_{CHUR}} - 1 \right] \times 10^4$$

Clinopyroxene from the Xuan Loc peridotites display a similar range of isotopic compositions to those from Pleiku: $^{206}Pb/^{204}Pb$ = 17.13-18.37, $^{207}Pb/^{204}Pb$ = 15.44-15.57, $^{208}Pb/^{204}Pb$ = 37.08–38.64, $^{87}Sr/^{86}Sr$ = 0.702565-0.704050, and ε_{Nd} = +3.16 - +14.29 ($^{143}Nd/^{144}Nd$ = 0.512800-0.513371).

The Pb isotopic compositions mostly lie within the Indian-MORB field and form positive correlations between $^{206}Pb/^{204}Pb$ and both $^{207}Pb/^{204}Pb$ and $^{208}Pb/^{204}Pb$ that plot above the northern hemisphere reference line (NHRL) (Fig. 7).

The Xuan Loc cpx compositions have systematically more radiogenic $^{208}Pb/^{204}Pb$ than Pleiku cpx on a plot of $^{206}Pb/^{204}Pb$ versus $^{208}Pb/^{204}Pb$ (Fig. 7).

Lead and Sr isotopes do not exhibit well-defined correlations with trace element data or with each other. Clinopyroxene $^{87}Sr/^{86}Sr$ and ε_{Nd} exhibit a negative correlation extending from the Indian-MORB field to highly radiogenic $^{143}Nd/^{144}Nd$ and unradiogenic $^{87}Sr/^{86}Sr$ (Fig. 8). The one type-R xenolith with $^{87}Sr/^{86}Sr$ and $^{143}Nd/^{144}Nd$ measurements (XL-1) plots to the right of the type-F xenoliths within the MORB field. Type-F xenoliths also have highly variable $^{143}Nd/^{144}Nd$ (0.512921-0.348419) with many samples plotting to the left of and above the MORB field in Figure 6.

Table 1. Isotopic composition of Vietnam xenoliths.

	Type	$^{87}Sr/^{86}Sr$	$^{143}Nd/^{144}Nd$	ε_{Nd}	$^{206}Pb/^{204}Pb$	$^{207}Pb/^{204}Pb$	$^{208}Pb/^{204}Pb$
Pleiku							
PL-1*	F	0.703267 ±5	-	-	16.92 ±1	15.45 ±1	36.90 ±3
PL-2	F	0.703365 ±6	0.514190 ±7	30.28	18.86	15.58	38.85
PL-3*	F	0.702447 ±6	0.513637 ±7	19.48	16.69 ±1	15.34 ±1	36.48 ±2
PL-5	F	0.702919 ±5	0.513091 ±4	8.84	18.59	15.52	38.58
PL-6*	F	0.702425 ±6	0.513776 ±5	22.19	18.29 ±1	15.49 ±1	38.28 ±3
PL-7	F	0.702988 ±7	-	-	17.39 ±1	15.48 ±1	37.30 ±2
PL-8	F	0.702463 ±6	-	-	18.18	15.56	38.20
PL-9	F	0.702381 ±5	0.513821 ±5	23.08	18.27 ±1	15.50 ±1	38.27 ±3
Xuan Loc							
XL-1	R	0.704050 ±6	0.512800 ±5	3.16	18.18	15.55	38.44
XL-3	F	0.702645 ±5	0.513196 ±5	10.89	17.35	15.46	37.42
XL-5	R	-	-	-	18.37	15.57	38.64
XL-8	F	0.703724 ±6	0.512921 ±5	5.51	18.28	15.54	38.51
XL-9	F	0.703162 ±6	0.513036 ±5	7.77	17.88	15.49	38.07
XL-11	R	-	-	-	18.32	15.57	38.61 ±1
XL-14	F	0.702952 ±6	0.513176 ±4	10.49	18.02	15.51	38.25
XL-15	F	0.702565 ±6	0.513358 ±12	14.04	17.13	15.44	37.08
XL-18	F	0.702995 ±6	0.513087 ±5	8.77	18.23	15.53	38.41
XL-19	F	0.702967 ±6	0.513371 ±5	14.29	17.87	15.51	38.03
XL-20	F	0.703070 ±6	0.513110 ±5	9.21	18.03	15.52	38.28
Standards							
NBS 987	n = 33	0.701254 ±9	-		-	-	-
Jndi-1	n = 15	-	0.512114 ±13		-	-	-
NBS 981	n = 90	-	-		16.94 ±1	15.50 ±3	36.72 ±4
BCR-2	n = 2	-	-		18.76	15.63	38.74 ±1
BHVO-2	n = 1	-	-		18.62	15.54	38.25

Note: Deviation values indicate 2σ standard error for the last digits expressed.
*Pb concentrations are near detection limits.

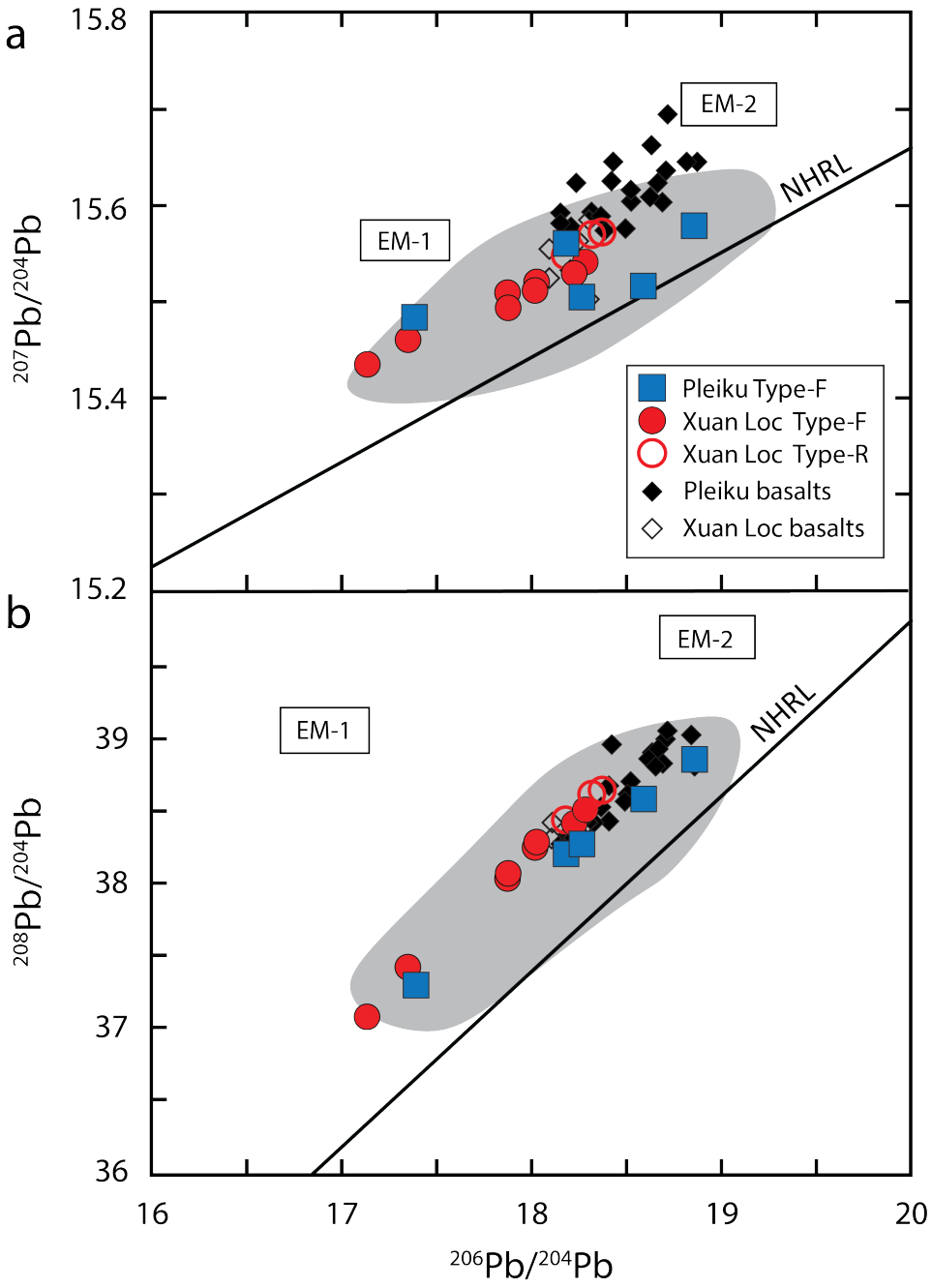

Figure 7. (a) $^{207}Pb/^{204}Pb$ and (b) $^{208}Pb/^{204}Pb$ versus $^{206}Pb/^{204}Pb$ of cpx from Pleiku and Xuan Loc peridotites for this study. Error bars (2σ) are smaller than symbol size. Grey field shows Indian-MORB field range. MORB fields and enriched mantle (EM-1 and EM-2) compositions are from literature data (Hofmann, 2007) and the northern hemisphere reference line (NHRL) is from Hart (1984). Pleiku and Xuan Loc basalts are from Hoang et al. (1996; 2013).

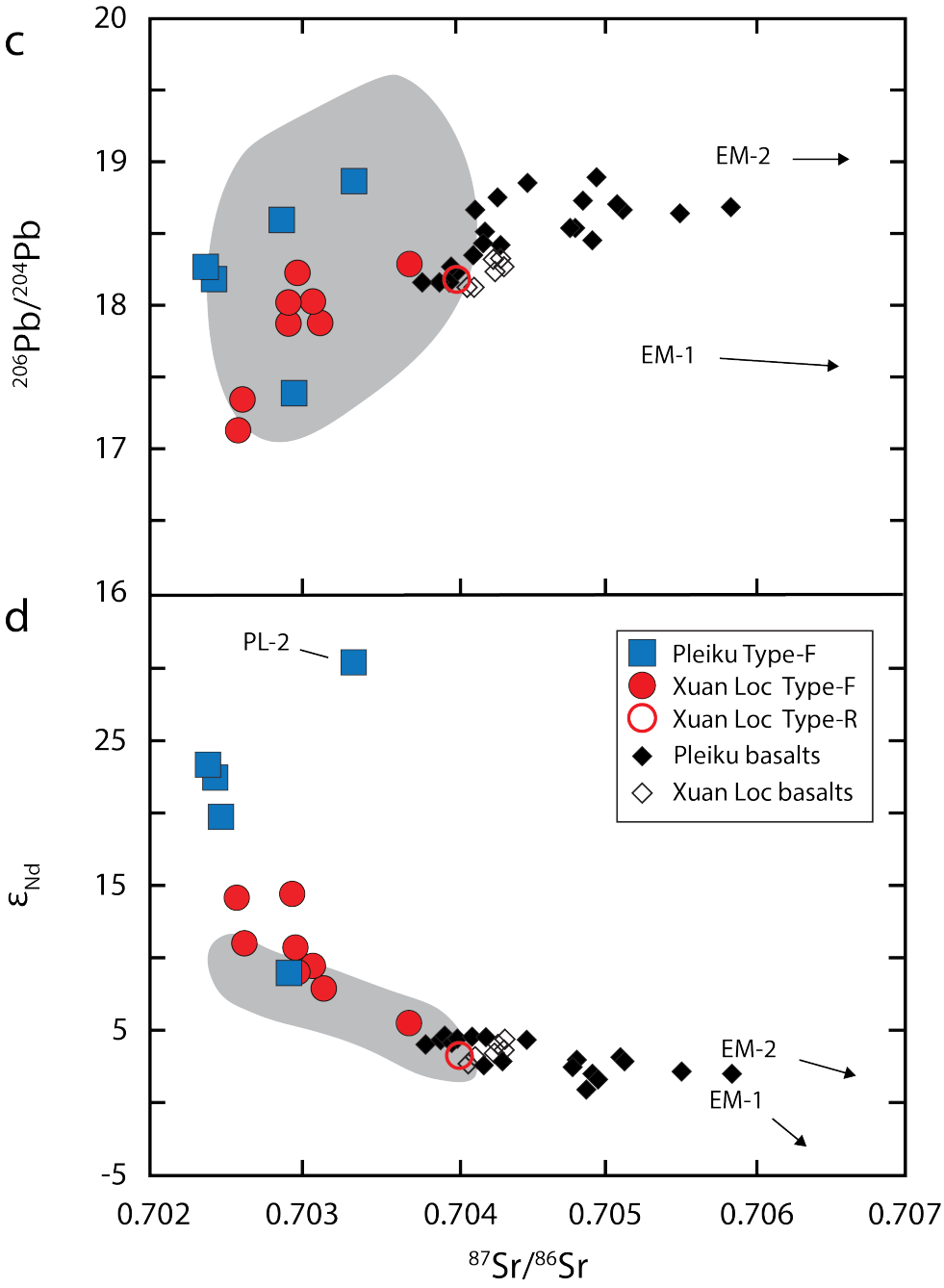

Figure 8. (a) $^{206}Pb/^{204}Pb$ and (b) ε_{Nd} versus $^{87}Sr/^{86}Sr$ of cpx in Pleiku and Xuan Loc peridotites. Error bars (2σ) are smaller than symbol size. Grey field shows Indian-MORB field range. MORB fields and enriched mantle (EM) compositions are from literature data (Hofmann, 2007). Pleiku and Xuan Loc basalts are from Hoang et al. (1996; 2013).

4.5 Thermometry and barometry

Calculated equilibrium temperatures and pressures for Vietnam xenoliths are presented in Table 2. Temperatures based on major element composition were calculated using the two-pyroxene thermometer (T_{BKN}) of Brey and Kohler (1990) at an assumed pressure of 15 kbar and temperatures based on REE + Y compositions were calculated using the two-pyroxene thermometer (T_{REE}) of Liang et al. (2013). For T_{BKN}, a ±5 kbar change in pressure results in a 10 °C difference. Differences between T_{BKN} are noticeable between calculations made with average core measurements and calculations made with average rim measurements for samples PL-1 and XL-14, with the core temperatures being higher by 345 °C and 155°C, respectively. This temperature difference corresponds to an increase in CaO wt% from the core to the rim, indicating that Ca-Mg-Fe exchange between pyroxene pairs was likely not in equilibrium. We thus do not consider the temperatures derived from these two samples to be robust. All other samples have core and rim temperatures that internally agree within 100 °C. T_{REE} values exhibit low uncertainties (determined from the linear fit of the inversion diagram; Table 2), except for samples PL-1, XL-5, and XL-11, which exhibit poorer fits (Appendix C). Samples XL-5 and XL-11 also have low HREE concentrations in opx (Fig. 5), indicating that the higher temperature uncertainty derives from lower analytical precision.

The equilibrium T_{BKN} temperatures are highly variable for Pleiku and Xuan Loc xenoliths, with ranges of 601-1005 °C and 721-930 °C, respectively. T_{REE} has a narrower range, with Pleiku xenoliths having a calculated range of 862-996 °C and Xuan Loc xenoliths having temperatures of 807-1052 °C. Many samples from Xuan Loc and one sample from Pleiku have T_{REE} temperature estimates much higher than T_{BKN}, and two Xuan Loc samples (XL-3 and XL-9) have higher T_{BKN} temperatures than T_{REE} (Fig. 9). Temperatures do not correlate with sample type or other fertility indices.

Equilibrium pressures of Vietnam xenoliths were calculated using major element compositions with the two-pyroxene barometer (P_{P38}) of Putirka (2008) using equation 38, which is temperature-independent. Calculated pressures from Pleiku xenoliths range from 8.9-13.3 kbar, while type-F peridotites from Xuan Loc display pressures of 10.1-14.1 kbar and type-R xenoliths are lower with a range of 7.4-8.7 kbar. The uncertainty for calculated P_{P38} values (±3.7 kbar) is relatively high for the estimated pressures of the Vietnam xenoliths, but there is nonetheless a calculated pressure difference of ~4 kbar between fertile and refractory samples.

Table 2. Equillibrium temperatures (°C) and pressures (kbars) of Vietnam xenoliths.

	Type	T_{BKN}	T_{REE}	(1σ)	P_{P38}
Pleiku					
PL-1	F	686	920	±100	8.9
PL-2	F	864	889	±37	13.6
PL-3	F	873	888	±26	13.0
PL-5	F	948	985	±32	11.6
PL-6	F	601	875	±32	10.7
PL-7	F	897	892	±48	11.9
PL-8	F	1005	996	±16	12.2
PL-9	F	876	862	±18	13.3
Xuan Loc					
XL-3	F	926	821	±52	12.8
XL-4	R	812	-		8.7
XL-5	R	856	969	±86	8.0
XL-7	F	903	1052	±51	14.0
XL-8	F	833	1043	±36	11.7
XL-9	F	930	853	±41	14.1
XL-11	R	767	984	±95	7.4
XL-12	R	833	-		8.3
XL-14	F	832	807	±11	13.3
XL-15	F	838	807	±20	12.0
XL-16	F	888	970	±47	11.9
XL-18	F	848	898	±22	11.6
XL-19	F	721	903	±51	10.1
XL-20	F	775	880	±45	11.3

Major element equilibrium temperatures are calculated from the two-pyroxene thermometer (T_{BKN}) of Brey and Kohler (1990). T_{BKN} has an error (1σ) of ±15 °C. Trace element equilibrium temperatures are calculated rom the two-pyroxene REE thermometer (T_{REE}) of Liang et al. (2013) and the uncertainties are from the linear fit of the inversion diagrams. Equillibration pressures (P_{P38}) are calculated from the two-pyroxene barometer of Putirka (2008) which has an error of ±3.7 kbars.

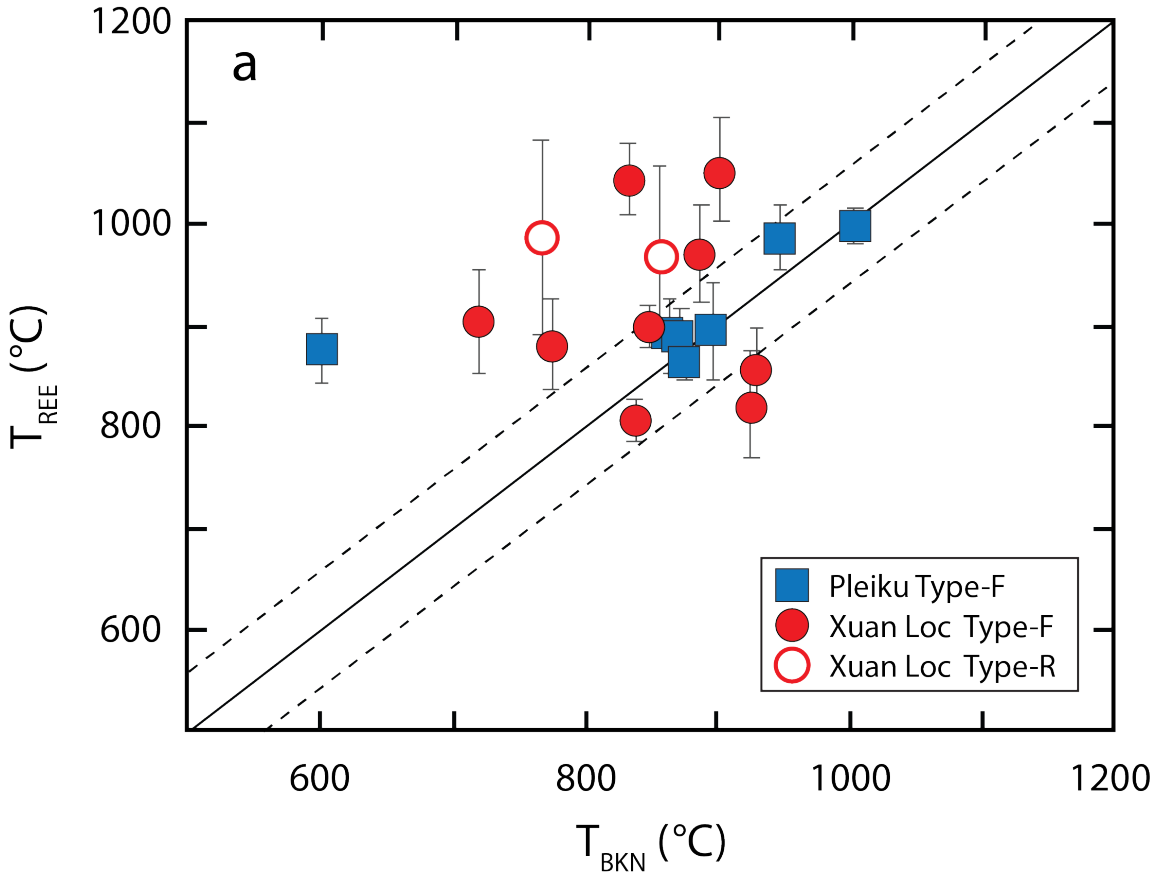

Figure 9. Comparison of equilibrium temperatures of Vietnam xenoliths with T_{REE} plotted against T_{BKN}. The uncertainties (1σ) for T_{BKN} are ±15 °C and the uncertainties for T_{REE} are shown with error bars. Black solid line is the 1:1 ratio with the dotted lines representing ±50 °C.

5. Discussion

5.1 History of magmatic processes beneath Indochina

The observed variations in major element, trace element, and isotopic compositions among Vietnam xenoliths are indicative of mantle residues that have undergone variable degrees of progressive melt extraction and other magmatic

processes (e.g., melt addition, refertilization, and metasomatism). There are two compositional groups of xenoliths, type-F and type-R, that suggest the SCLM beneath Indochina may record two distinct histories.

5.1.1 Extent of partial melting

Constraining the extent of prior melting experienced by lithospheric mantle xenoliths using incompatible element concentrations can help identify local lithospheric mantle histories and rock types. When estimating the degree of melting, sp Cr # and HREE concentrations in cpx are useful due to being highly correlated and having lower susceptibility to metasomatism (Warren, 2016). Fractional melting processes can account for extreme fractionation of LREE during melting and, thus, are a better fit than batch or equilibrium melting for many observed residual peridotites in the literature (Johnson et al., 1990; Hellebrand et al., 2001). The melting model of Hellebrand et al. (2001) utilizes the strong correlation between sp Cr# and HREE to calculate the degree of fractional melting as a function of sp Cr#, assuming an initial composition drawn from a LREE-depleted lherzolite from Loubet et al. (1975). The Hellebrand et al. (2001) empirical function was derived using the degrees of melting calculated from Dy, Er, and Yb, after the method of Johnson et al. (1990). Calculations using this model for Vietnam xenoliths yields values with a range of 15-17% for type-R xenoliths from Xuan Loc and values up to 6.1% melting for type-F xenoliths from both localities (Fig. 11). Applying this

melting model to the published Pleiku dataset by Nguyen and Kil (2019) yields melting degrees of 10.3-18.5% and up to 7.1% for type-R and type-F xenoliths, respectively.

Type-R harzburgites and dunites also exhibit major element and trace element compositions similar to mantle xenoliths from ancient SCLM (McDonough, 1990; Griffin et al., 2008), namely low cpx Al_2O_3 (1.72-3.15 wt%), high cpx Mg# (0.915-0.937) and high $(LREE/HREE)_{PM}$ (Fig. 10). These systematics are not unique to SCLM, however, as similar characteristics have been found in abyssal peridotites (Warren, 2016). Low modal cpx is indicative of previously fertile mantle peridotites where cpx was ultimately consumed by extensive melting (Herzberg, 1999). Type-R samples from Xuan Loc have high sp Cr#s and strong depletions in HREE (Appendix A; B), which also indicate a high degree of melt extraction. There is also a strong negative correlation between Ti and sp Cr# across all type-R xenoliths, indicating high degrees of partial melt extraction (Fig. 11). The refractory harzburgites from Pleiku (Nguyen and Kil, 2019) have major and trace element compositions that resemble type-R refractory samples from Xuan Loc, indicating that both the Pleiku and Xuan Loc volcanic centers overlie SCLM containing highly-depleted residues. However, all type-R xenoliths from Pleiku and Xuan Loc also have relatively high LREE enrichment, and the single type-R ε_{Nd} measurement (3.16) is relatively unradiogenic (Table 1), suggesting a further history of melt-rock interactions.

Type-F xenoliths from Vietnam contain cpx with relatively fertile major element compositions (e.g., Al_2O_3 = 5.70-7.17 wt%) that fall within the range of abyssal peridotites, though Vietnamese xenoliths are slightly less fertile than estimates for depleted mantle cpx compositions (7.87 wt. % Al_2O_3 in cpx) (Workman and Hart, 2005; Warren, 2016). The depleted and spoon-shaped REE_{PM} patterns exhibited by some type-F lherzolites from Pleiku and Xuan Loc is consistent with partial melting with subsequent enrichment during silicate-melt metasomatism. Clinopyroxenes from abyssal peridotites display similar LREE patterns to our xenoliths, although they typically display more extreme positive LREE to MREE slopes (Warren, 2016; and references therein). While Type-F lherzolites from Pleiku and Xuan Loc both exhibit depleted and spoon-shaped REE_{PM} in cpx, Pleiku displays a lower $(LREE/HREE)_{PM}$ than Xuan Loc ($(Ce/Yb)_{PM}$ of 0.17 versus 0.51, respectively). This likely indicates a difference in SCLM source compositions between the two locations and will be discussed further below. Sample XL-8 is an outlier in that it displays an elevated, enriched signature in LREE. However, it does show relative depletion in other incompatible trace elements (Rb, Nb, Pb, Zr, and Ti) and likely experienced metasomatism that overprinted any previous extraction of LREE.

Recent studies of abyssal peridotites indicate a globally heterogeneous upper mantle composition, and have revealed that there are ultradepleted mantle domains (i.e., isotopically more depleted than the Depleted MORB Mantle reservoir (DMM)) that have been preserved in the convecting upper mantle (Liu et al., 2008; Salters et

al., 2011; Stracke et al., 2011, 2019; Stracke, 2012; Byerly and Lassiter, 2014). Furthermore, xenoliths with fertile major and trace elements and depleted isotopic signatures have been found in several localities (e.g., Eastern and Western Europe, Rio Grande Rift, Zealandia) and attributed to juvenile mantle lithosphere that was recently emplaced from the convecting upper mantle (Downes, 2001; Byerly and Lassiter, 2012; Scott et al., 2014). Type-F xenoliths from Vietnam exhibit unradiogenic $^{87}Sr/^{86}Sr$ and highly variable but relatively radiogenic ε_{Nd} compositions that span the range of abyssal peridotites, from estimates of depleted mantle to a more depleted source (Fig. 8) (Salters and Stracke, 2004; Workman and Hart, 2005; Hofmann, 2007). Sample PL-2 from Pleiku is anomalous in that it has more radiogenic $^{87}Sr/^{86}Sr$ (0.703365) than would be expected given its very high ε_{Nd} value of +30.28. The relatively radiogenic $^{87}Sr/^{86}Sr$ ratio suggests ancient reenrichment in Rb by metasomatism (Alibert, 1994). Type-F xenoliths exhibit little to no metasomatism, which would be expected to occur from subduction-derived fluids during the emplacement of granitic crust in the Mesozoic (Nam et al., 2001; Shellnutt et al., 2013). Given the similarities in major, trace, and isotopic compositions between type-F xenoliths and the DMM, we interpret these xenoliths to be derived from recently emplaced asthenospheric mantle beneath Indochina.

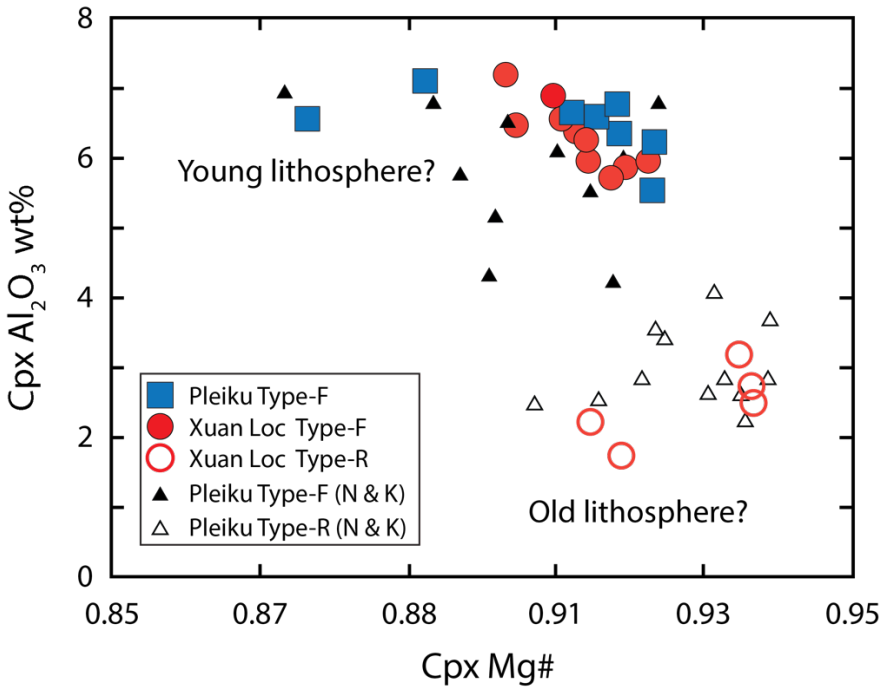

Figure 10. Cpx Al_2O_3 wt% vs cpx Mg# (molar Mg/(Mg + Fe)). Low Al_2O_3, and high cpx Mg# characterize xenoliths that have undergone extensive melt extraction. N & K = Pleiku xenoliths from Nguyen and Kil (2019).

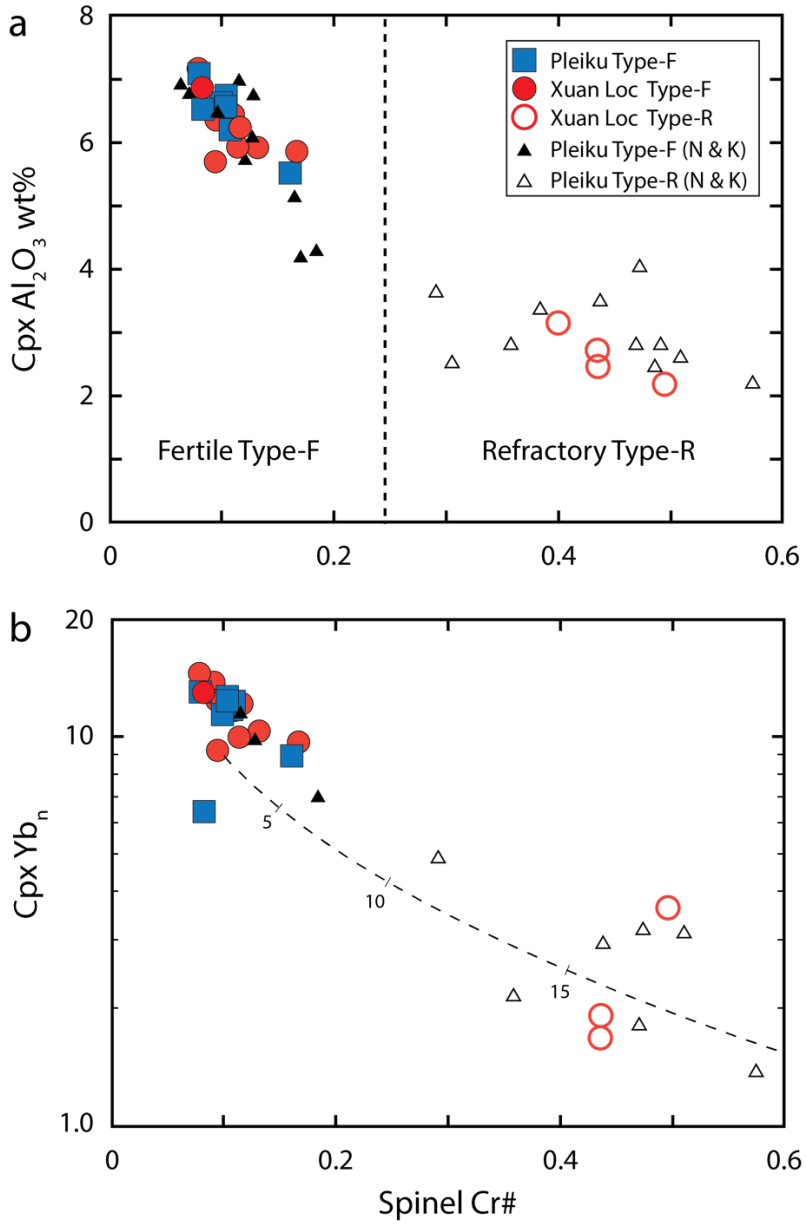

Figure 11. Spinel Cr# vs a) Al_2O_3 wt% in cpx and b) Yb in cpx normalized to chondrite. Low Al_2O_3, low Yb, and high sp Cr# characterize xenoliths that have undergone extensive melt extraction. The dashed line and tickmarks show the calculated degree of melting as a percentage, where the degrees of melting are a function of sp Cr# (Hellebrand et al., 2001) and Yb concentration (Johnson et al., 1990). N & K = Pleiku xenoliths from Nguyen and Kil (2019).

5.1.2 Metasomatism of the SCLM beneath Vietnam

Given that LREE are highly incompatible, they should be strongly depleted by removal from the source rock during partial melting. The apparent enrichment in these elements in type-R xenoliths and type-F xenoliths with "spoon-shaped" REE_{PM} patterns requires an additional explanation, and likely indicates metasomatism of incompatible-element depleted residues by the later addition of a LREE-enriched melt. Type-F xenoliths only display enrichment in the most incompatible elements. The lack of significant melt-rock interactions exhibited by type-F xenoliths may indicate that they were not a constituent of the SCLM beneath Indochina during previous emplacement of subduction-derived melts in the Mesozoic.

Depletions of Ti relative to HREE and enrichment in LREE in mantle rocks have previously been used to characterize the metasomatic agents responsible for melt-rock interactions (Coltorti et al., 1999). Given the notably low Ti/Eu (<1500) and high $(La/Yb)_n$ in type-R cpx from Xuan Loc, CO_2-rich silicate melts (i.e., subduction-related melts) may provide a potential metasomatic agent, a scenario that has previously been suggested for the refractory xenoliths from Pleiku (Nguyen and Kil, 2019). This scenario is supported by sample XL-1, which exhibits characteristics typical of metasomatism by a CO_2-rich silicate melt, with its extreme depletions in Nb, Zr, and Hf and the presence of cpx with no opx. However, recent studies have shown that Ti anomalies can instead be attributed to the slower

diffusion of high field strength elements (HFSE) compared to HREE within refractory mantle rocks (Byerly and Lassiter, 2015). This diffusion rate effect may cause refractory cpx to exhibit a lower Ti/Eu ratio than cpx from more fertile lherzolites. In support of the latter scenario, two of the type-R xenoliths from Xuan Loc (samples XL-4 and XL-5) with Ti/Eu < 1500 also exhibit high rim/core variations in TiO_2 wt % (rim/core ratio of 1.35 and 1.16, respectively), indicating that Ti is not in equilibrium, and these samples likewise do not have the extreme Hf and Zr depletions expected from metasomatism by CO_2 -rich melts. There are also positive anomalies of HFSE in opx (Fig. 6) in type-R xenoliths, which may offset the negative anomalies exhibited by cpx. Furthermore, subduction-derived, CO_2-rich silicate melts like those posited to have metasomatized Pleiku xenoliths (Nguyen and Kil, 2019) are expected to be enriched in Pb, Sr, and Rb and highly depleted in Nb (Ionov, 2002). Type-R xenoliths from Xuan Loc do exhibit slight Nb depletions compatible with interactions with such a magma, but they also have negative anomalies in Rb and Pb, making the carbonated magma scenario less consistent.

Chromatographic metasomatism during reactive porous flow from a CO_2-rich silicate melt may likewise have caused some of the observed variations between type-R and type-F xenoliths (Ionov, 2002), but chromatographic metasomatism typically induces strong fractionations in LREE ratios causing "U-shaped" REE_{PM} patterns (Orejana and Villaseca, 2008). It is thus difficult to broadly identify a single type metasomatism, and we observe evidence that subduction-related melt metasomatism has potentially affected some of the xenoliths and not others. The

Vietnam xenoliths do demonstrate evidence of interactions with small volumes of melt in the SCLM that overprinted preexisting REE depletion signatures, but not pervasively enough to fully erase the depletion history recorded in the major element compositions.

While type-F xenoliths from Pleiku and Xuan Loc share similar characteristics that may suggest similar processes have modified the SCLM in both locations, samples from the two sites exhibit a few distinct differences in trace element and isotopic composition. Specifically, Pleiku type-F xenoliths display higher levels of depletion in LREE, less radiogenic $^{208}Pb/^{204}Pb$, and more radiogenic ε_{Nd} than Xuan Loc xenoliths. This may indicate that the type-F xenoliths from Pleiku were initially derived from asthenosphere that had higher levels of ancient melt extraction than the Xuan Loc xenoliths. Another possibility is that metasomatism in Xuan Loc xenoliths enriched LREE concentrations while also contributing a more unradiogenic ε_{Nd} composition to the affected rocks, which could explain the notably more isotopically enriched composition of sample XL-8 (Fig. 8). The comparatively short half-lives of ^{238}U and ^{232}Th relative to ^{147}Sm and ^{87}Rb, in addition to the behavior of U and Th during metasomatism, could have contributed to the slightly elevated $^{208}Pb/^{204}Pb$ relative to $^{206}Pb/^{204}Pb$ observed in all Xuan Loc xenoliths, suggesting the Pb isotope signatures may likewise be a product of melt-rock interactions (Wittig et al., 2010). This interpretation requires a significant amount of time to produce the ingrowth of Pb. Another, more likely scenario, is that the elevated isotopic signatures preserve a noticeable difference in the source

composition between Xuan Loc and Pleiku xenoliths. This interpretation would indicate that Xuan Loc xenoliths have a source slightly more enriched in Th relative to U when compared to the source of Pleiku xenoliths.

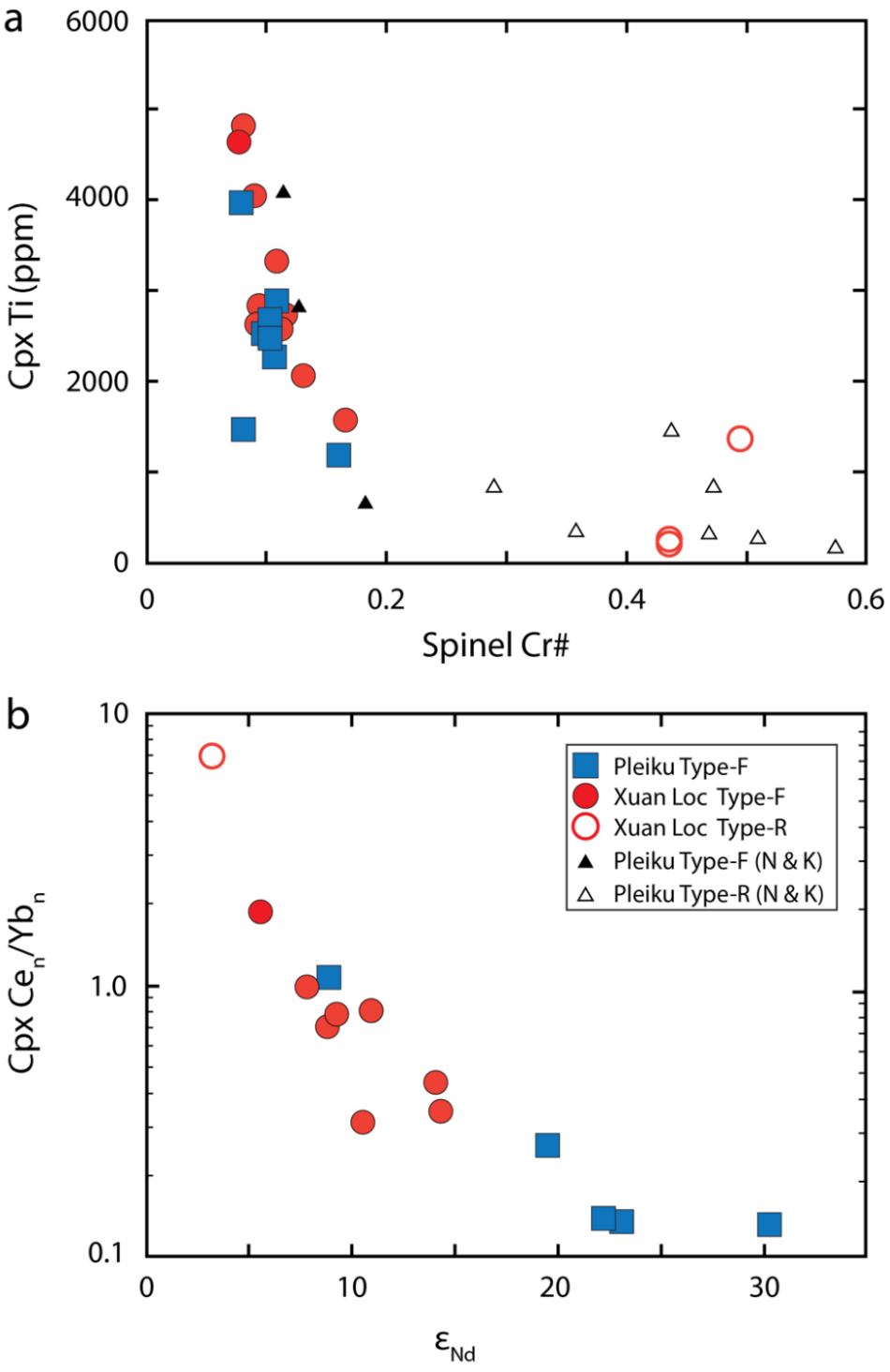

Figure 12. (a) Spinel Cr# vs [Ti] in cpx of Vietnam xenoliths. N & K = Pleiku xenoliths from Nguyen and Kil (2019). (b) ε_{Nd} in cpx vs (Ce/Yb) in cpx normalized to primitive mantle of Vietnam xenoliths.

5.2 Thermal state of the SCLM and equilibration depths of Vietnam xenoliths

Calculating equilibrium temperatures from mantle xenoliths will allow better constraints on the depths from which the xenoliths were derived and, thus, the depth to the SCLM. Equilibrium temperatures calculated from Vietnam xenoliths (721-1052ºC) indicate a relatively hot SCLM layer beneath Indochina (Table 2; Fig. 9). Temperatures are relatively consistent in the xenoliths across Pleiku and Xuan Loc. In general, we expect that discrepancies between calculated T_{BKN} and T_{REE} values for a xenolith rock may indicate a complex cooling history, possibly due to slower diffusion of trivalent REE compared to divalent Ca, Mg, and Fe in pyroxenes during slow cooling (Liang et al., 2013; Dygert and Liang, 2015). Such diffusion effects should produce a higher T_{REE} than T_{BKN} value for a single sample (Liang et al., 2013). Most T_{BKN} temperatures for Pleiku xenoliths (721-1005ºC) fall within the range calculated by Nguyen and Kil (2019) (841-1131ºC), except for our sample PL-6 (T_{BKN} = 601 °C). Due to the slower diffusion of REE and the relatively minor standard deviations of calculated T_{REE} values within each sample suite, we interpret T_{REE} values to best represent equilibrium conditions prior to exhumation and will use them to estimate the extraction depths of the xenoliths.

One method for determining the extraction depths of Vietnam xenoliths is to use heat flow data with the local geothermal gradient. Unfortunately, there are currently no local heat flow data in the immediate vicinity of the study areas, so best estimates come from regional datasets, which have been compiled into a heat flow map (Hall, 2002). From this map, the estimated heat flow values for our study areas

are 85 mW/m^2 and 90 mW/m^2 for Pleiku and Xuan Loc, respectively. The measured thickness of the crust is 32 km at Pleiku and 28 km at Xuan Loc, from broadband seismic data (Yu et al., 2017). We assumed average densities (ρ) of 2800 kg/m^3 and 3250 kg/m^3 for the crust and mantle, respectively, with thermal conductivities of 2.7 W/(m·K) for the crust and 4.0 W/(m·K) for the mantle (Turcotte and Schubert, 2002). The heat generation (HG) of the crust was calculated using the model of Hasterok and Chapman (2011):

$$HG = 10^{-5}\rho\left[3.5\mathrm{C}_{\mathrm{K_2O}} + 9.67\mathrm{C}_{\mathrm{U}} + 2.63\mathrm{C}_{\mathrm{Th}}\right]$$

where C_i values indicate concentrations for the species *i*. We used the estimated abundances of heat producing elements for average crust from Rudnick and Fountain (1995). Using these methods and our range of calculated T_{REE} values, the calculated range of extraction depths for Vietnam xenoliths is 35-45 km (9.8-13.0 kbar) for Pleiku and 29-45 km (8.0-13.0 kbar) for Xuan Loc (Fig. 13). There is no significant difference in depths of equilibration between type-F and type-R xenoliths. Due to the lack of local heat flow data, these estimates have high uncertainty. However, they are relatively consistent with the equilibrium pressures (Pleiku = 8.9-13.3 ±3.7 kbar; Xuan Loc = 7.4-14.1 ±3.7 kbar) calculated from the Putirka (2008) barometer.

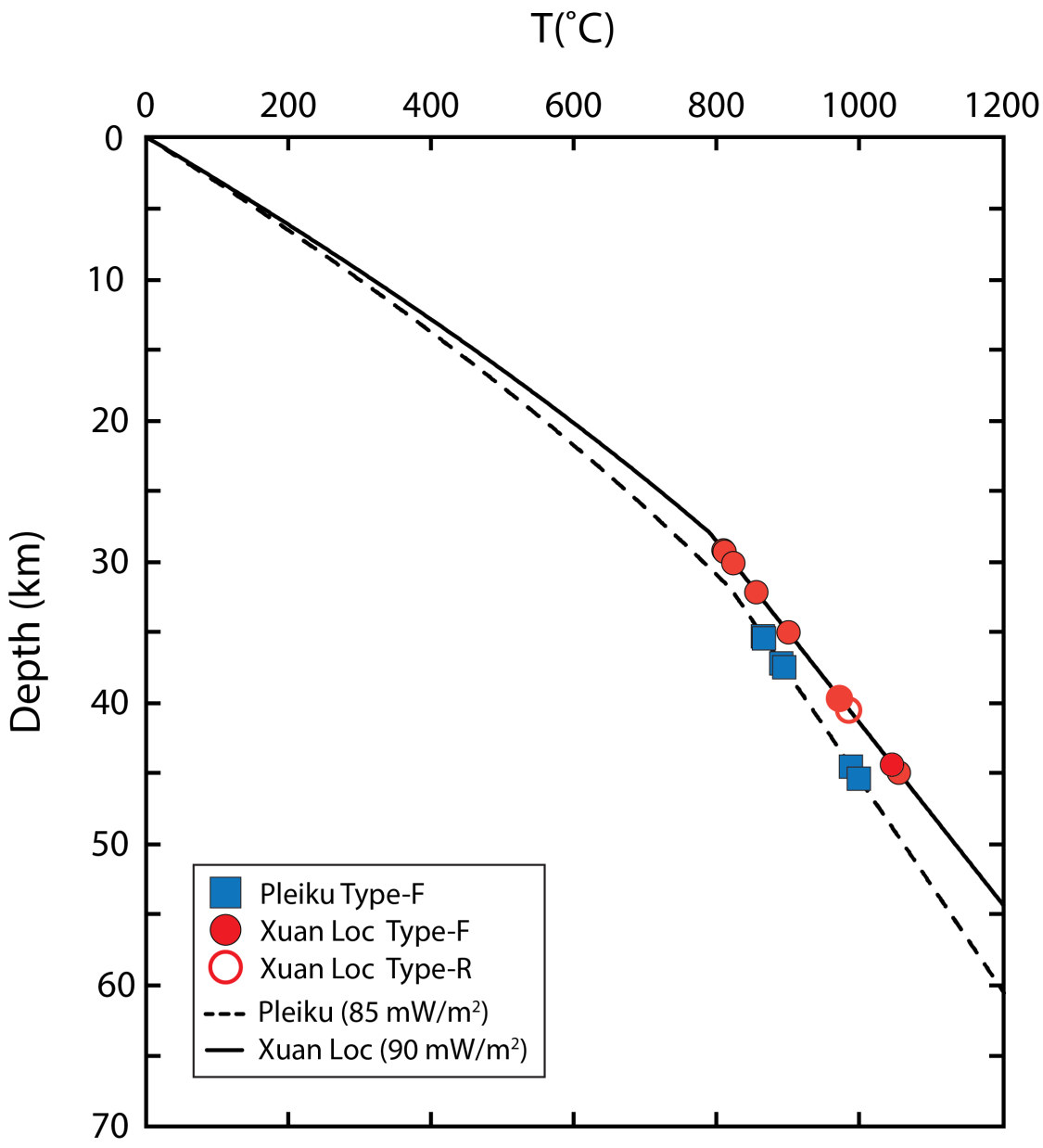

Figure 13. Our model of the geothermal gradient beneath Pleiku and Xuan Loc. Modelled using measured lithospheric thickness, estimated heat flow, and includes heat input from radioactive decay elements in the crust. The estimated depth of equilibration was based on T_{REE} temperatures. Heat flow values are from Hall (2002) and references therein.

5.4 Implications for extrusion tectonics

The presence of mantle xenoliths with an asthenospheric source composition at depths between 30-45 km (Fig. 13), and with inferred relatively young ages (inferred from the apparent lack of metasomatism from subduction-derived melts) implies that the SCLM beneath Vietnam has been relatively recently replaced by younger convecting asthenosphere, which suggests that older continental lithospheric mantle must have been partially removed during an earlier event. The type-F xenoliths exhibit $^{87}Sr/^{86}Sr$ (0.703724-0.703365) and ε_{Nd} isotopes (5.51-30.28) that range from values resembling ultra-depleted mantle (Cipriani et al., 2011; Stracke et al., 2011; Mallick et al., 2014) to those of MORB (Salters and Stracke, 2004; Workman and Hart, 2005; Hofmann, 2007). Type-F xenoliths also have relatively fertile compositions that likely experienced only small degrees of partial melting, suggesting the xenoliths were a part of the asthenospheric mantle that underwent decompression melting. In this scenario, the metasomatism expressed in the LREE (Fig. 5) and core/rim variations (Fig. 4) occurred after partial melting.

Determining the source of type-R xenoliths is more complex, given the high levels of overprinting of trace elements and isotopic compositions due to likely metasomatism (e.g., Fig. 5). Mantle xenoliths with similar trace element and isotopic characteristics are often attributed but are not unique to pre-Phanerozoic

lithosphere (e.g., Rio Grande Rift, Colarado Plateau, Zealandia, North China Craton, Central Asian Orogenic Belt) (McDonough, 1990; Byerly and Lassiter, 2012; Liu et al., 2012; Pan et al., 2013; Scott et al., 2014; Warren, 2016). Type-R xenoliths from Xuan Loc and from Pleiku (Nguyen and Kil, 2019) also exhibit characteristics of peridotites that have experienced high degrees of fractional melting, and the Xuan Loc type-R xenolith measured for radiogenic isotopes (XL-1) has an enriched isotopic signature ($^{87}Sr/^{86}Sr$ = 0.704050, and ε_{Nd} = 3.16), making type-R xenoliths a possible candidate for the residues of older lithospheric mantle that has been partially removed.

5.5 Working model for the SCLM beneath Vietnam

The presence of fertile and refractory mantle beneath Vietnam concurrent with high heat flow and voluminous basaltic eruptives across Indochina may indicate a history of partial lithospheric removal and replacement (Fig. 14). During the India-Eurasia collision Indochina was extruded along the Ailao Shan-Red River Fault Zone until the cessation of the South China Sea rifting (Zhu et al., 2009; Li et al., 2015). The lack of a "free boundary" during extrusion could have caused the hot convecting asthenosphere, which was flowing parallel to the direction of extrusion, to also upwell and thermally erode the refractory SCLM mantle resulting in the voluminous (70,000 km^2) first-stage eruption of tholeiites. In this scenario, subsequent upwelling of the underlying asthenosphere resulted in small degrees of

decompression melting and the eruption of alkali basalts. Melts derived from deeper in the asthenosphere may have interacted with younger, recently-emplaced lithosphere (type-F xenoliths) and the older, remnant refractory SCLM (type-R xenoliths), resulting in variable degrees of melt-rock metasomatism. This likely formed a relatively heterogeneous SCLM where young, asthenospheric mantle was emplaced adjacent to the older, refractory mantle.

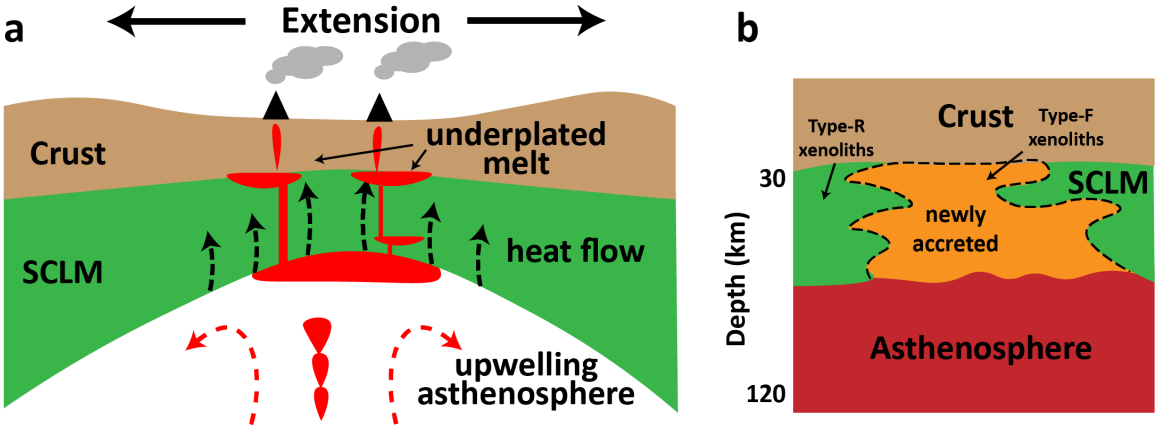

Figure 14. Diagram of lithospheric erosion beneath Vietnam. a) Local extension and erosion of the SCLM followed by the b) emplacement of the convecting mantle adjacent to refractory mantle. Modified after Pan et al. (2013).

6. Conclusions

In this study, we have characterized two suites of xenoliths from southern Vietnam. The measured major elements of peridotite mineral separates, trace elements of cpx and opx, and Sr-Nd-Pb isotopic compositions of cpx in the Pleiku

and Xuan Loc mantle peridotites provide the following insights into the lithospheric mantle of Vietnam:

(1) The lithospheric mantle beneath Vietnam experienced a complex history of partial melting and subsequent metasomatism which is preserved in spinel peridotites that can be divided into two groups based on their sp Cr#.

(2) Type-F spinel peridotites from Pleiku and Xuan Loc exhibit fertile compositions with depleted and spoon-shaped REE_{PM} patterns indicative of lithosphere that has undergone low degrees of partial melting and subsequent small degrees of melt metasomatism. They show Sr-Nd isotope compositions that resemble newly accreted SCLM.

(3) Type-R spinel peridotites from Xuan Loc display refractory compositions with enriched and S-shaped REE_{PM} patterns that indicate high degrees of partial melting followed by metasomatic enrichment and share characteristics typical of ancient refractory SCLM.

(4) The extrusion of Indochina may have induced asthenospheric upwelling (associated with later-emplaced type-F xenoliths) beneath Vietnam, causing thermal erosion and partial melting of older refractory lithosphere (resembling type-R xenoliths). The upwelling asthenosphere underwent decompressive melting and partial accretion to the subcontinental lithosphere. The current SCLM beneath Vietnam thus consists of young fertile mantle adjacent to refractory older mantle.

7. References

Alibert, C., 1994, Peridotite xenoliths from western Grand Canyon and The Thumb: A probe into the subcontinental mantle of the Colorado Plateau: Journal of Geophysical Research: Solid Earth, v. 99, p. 21605–21620, doi:10.1029/94JB01555.

Armstrong, J.T., 1988, Quantitative analysis of silicate and oxide materials: comparision of Monte Carlo, ZAF, and ϕ(ρZ) procedures: Microbeam Analysis, p. 239–246.

Ballhaus, C., Berry, R.F., and Green, D.H., 1991, High pressure experimental calibration of the olivine-orthopyroxene-spinel oxygen geobarometer: implications for the oxidation state of the upper mantle: Contributions to Mineralogy and Petrology, v. 107, p. 27–40, doi:10.1007/BF00311183.

Brey, G.P., and Kohler, T., 1990, Geothermobarometry in Four-phase Lherzolites II. New Thermobarometers, and Practical Assessment of Existing Thermobarometers: Journal of Petrology, v. 31, p. 1353–1378, doi:10.1093/petrology/31.6.1353.

Byerly, B.L., and Lassiter, J.C., 2012, Evidence from mantle xenoliths for lithosphere removal beneath the central Rio Grande Rift: Earth and Planetary Science Letters, v. 355–356, p. 82–93, doi:10.1016/j.epsl.2012.08.034.

Byerly, B.L., and Lassiter, J.C., 2014, Isotopically ultradepleted domains in the convecting upper mantle: Implications for MORB petrogenesis: Geology, v. 42, p. 203–206, doi:10.1130/G34757.1.

Byerly, B.L., and Lassiter, J.C., 2015, Trace element partitioning and Lu–Hf isotope systematics in spinel peridotites from the Rio Grande Rift and Colorado Plateau: Towards improved age assessment of clinopyroxene Lu/Hf–176Hf/177Hf in SCLM peridotite: Chemical Geology, v. 413, p. 146–158, doi:10.1016/j.chemgeo.2015.08.009.

Cipriani, A., Bonatti, E., and Carlson, R.W., 2011, Nonchondritic ^{142}Nd in suboceanic mantle peridotites: Geochemistry, Geophysics, Geosystems, v. 12, doi:10.1029/2010GC003415.

Coltorti, M., Bonadiman, C., Hinton, R.W., Siena, F., and Upton, B.G.J., 1999, Carbonatite Metasomatism of the Oceanic Upper Mantle: Evidence from Clinopyroxenes and Glasses in Ultramafic Xenoliths of Grande Comore, Indian Ocean: Journal of Petrology, v. 40, p. 133–165, doi:10.1093/petroj/40.1.133.

Cullen, A., Reemst, P., Henstra, G., Gozzard, S., and Ray, A., 2010, Rifting of the South China Sea: new perspectives: Petroleum Geoscience, v. 16, p. 273–282, doi:10.1144/1354-079309-908.

Dawson, J.B., 1984, Contrasting Types of Upper-Mantle Metasomatism?, in Kornprobst, J. ed., Developments in Petrology, Elsevier, v. 11, p. 289–294, doi:10.1016/B978-0-444-42274-3.50030-5.

Downes, H., 2001, Formation and Modification of the Shallow Sub-continental Lithospheric Mantle: a Review of Geochemical Evidence from Ultramafic Xenolith Suites and Tectonically Emplaced Ultramafic Massifs of Western and

Central Europe: Journal of Petrology, v. 42, p. 233–250, doi:10.1093/petrology/42.1.233.

Dygert, N., and Liang, Y., 2015, Temperatures and cooling rates recorded in REE in coexisting pyroxenes in ophiolitic and abyssal peridotites: Earth and Planetary Science Letters, v. 420, p. 151–161, doi:10.1016/j.epsl.2015.02.042.

Flower, M., Tamaki, K., and Hoang, N., 1998, Mantle extrusion: A model for dispersed volcanism and DUPAL-like asthenosphere in East Asia and the western Pacific, in Flower, M.F.J., Chung, S., Lo, C., and Lee, T. eds., Geodynamics Series, Washington, D. C., American Geophysical Union, v. 27, p. 67–88, doi:10.1029/GD027p0067.

Frey, F.A., and Green, D.H., 1974, The mineralogy, geochemistry and origin of Iherzolite inclusions in Victorian basanites: Geochimica et Cosmochimica Acta, v. 38, p. 1023–1059, doi:10.1016/0016-7037(74)90003-9.

Frey, F.A., and Prinz, M., 1978, Ultramafic inclusions from San Carlos, Arizona: Petrologic and geochemical data bearing on their petrogenesis: Earth and Planetary Science Letters, v. 38, p. 129–176, doi:10.1016/0012-821X(78)90130-9.

Gast, P.W., 1968, Trace element fractionation and the origin of tholeiitic and alkaline magma types: Geochimica et Cosmochimica Acta, v. 32, p. 1057–1086, doi:10.1016/0016-7037(68)90108-7.

Gibbons, A.D., Zahirovic, S., Müller, R.D., Whittaker, J.M., and Yatheesh, V., 2015, A tectonic model reconciling evidence for the collisions between India, Eurasia and intra-oceanic arcs of the central-eastern Tethys: Gondwana Research, v. 28, p. 451–492, doi:10.1016/j.gr.2015.01.001.

Griffin, W.L., O'Reilly, S.Y., Afonso, J.C., and Begg, G.C., 2008, The Composition and Evolution of Lithospheric Mantle: a Re-evaluation and its Tectonic Implications: Journal of Petrology, v. 50, p. 1185–1204, doi:10.1093/petrology/egn033.

Hall, R., 2002, SE Asian heatflow: call for new data: SEAPEX press, v. 5, p. 54–56.

Hart, S.R., 1984, A large-scale isotope anomaly in the Southern Hemisphere mantle: Nature, v. 309, p. 753–757, doi:10.1038/309753a0.

Hasterok, D., and Chapman, D.S., 2011, Heat production and geotherms for the continental lithosphere: Earth and Planetary Science Letters, v. 307, p. 59–70, doi:10.1016/j.epsl.2011.04.034.

Hellebrand, E., Snow, J.E., Dick, H.J.B., and Hofmann, A.W., 2001, Coupled major and trace elements as indicators of the extent of melting in mid-ocean-ridge peridotites: Nature, v. 410, p. 677–681, doi:10.1038/35070546.

Herzberg, C., 1999, Phase equilibrium constraints on the formation of cratonic mantle: Mantle Petrology: Field Observations and High Pressure Experimentation. Geochemical Society, Special Publications, v. 6, p. 241–257.

Hoang, N., and Flower, M., 1998, Petrogenesis of Cenozoic Basalts from Vietnam: Implication for Origins of a 'Diffuse Igneous Province': Journal of Petrology, v. 39, p. 369–395, doi:10.1093/petroj/39.3.369.

Hoang, N., Flower, M.F.J., and Carlson, R.W., 1996, Major, trace element, and isotopic compositions of Vietnamese basalts: Interaction of hydrous EM1-rich asthenosphere with thinned Eurasian lithosphere: Geochimica et Cosmochimica Acta, v. 60, p. 4329–4351, doi:10.1016/S0016-7037(96)00247-5.

Hoang, N., Flower, M.F.J., Chi, C.T., Xuan, P.T., Quy, H.V., and Son, T.T., 2013, Collision-induced basalt eruptions at Pleiku and Buôn Mê Thuột, south-central Viet Nam: Journal of Geodynamics, v. 69, p. 65–83, doi:10.1016/j.jog.2012.03.012.

Hofmann, A.W., 2007, Sampling Mantle Heterogeneity through Oceanic Basalts: Isotopes and Trace Elements, in Carlson, R.W., Holland, H.D., and Turekian, K.K. eds., Treatise on Geochemistry: The Mantle and Core, New York, Elsevier, p. 61–101.

Ionov, D.A., 2002, Mechanisms and Sources of Mantle Metasomatism: Major and Trace Element Compositions of Peridotite Xenoliths from Spitsbergen in the Context of Numerical Modelling: Journal of Petrology, v. 43, p. 2219–2259, doi:10.1093/petrology/43.12.2219.

Johnson, K.T.M., Dick, H.J.B., and Shimizu, N., 1990, Melting in the oceanic upper mantle: An ion microprobe study of diopsides in abyssal peridotites: Journal of Geophysical Research, v. 95, p. 2661, doi:10.1029/JB095iB03p02661.

Jolivet, L., Faccenna, C., Becker, T., Tesauro, M., Sternai, P., and Bouilhol, P., 2018, Mantle Flow and Deforming Continents: From India-Asia Convergence to Pacific Subduction: Tectonics, v. 37, p. 2887–2914, doi:10.1029/2018TC005036.

Lassiter, J.C., Blichert-Toft, J., Hauri, E.H., and Barsczus, H.G., 2003, Isotope and trace element variations in lavas from Raivavae and Rapa, Cook–Austral islands: constraints on the nature of HIMU- and EM-mantle and the origin of mid-plate volcanism in French Polynesia: Chemical Geology, v. 202, p. 115–138, doi:10.1016/j.chemgeo.2003.08.002.

Li, C.-F. et al., 2015, Seismic stratigraphy of the central South China Sea basin and implications for neotectonics: Journal of Geophysical Research: Solid Earth, v. 120, p. 1377–1399, doi:10.1002/2014JB011686.

Liang, Y., Sun, C., and Yao, L., 2013, A REE-in-two-pyroxene thermometer for mafic and ultramafic rocks: Geochimica et Cosmochimica Acta, v. 102, p. 246–260, doi:10.1016/j.gca.2012.10.035.

Liermann, H.P., and Ganguly, J., 2003, Fe2+–Mg fractionation between orthopyroxene and spinel: experimental calibration in the system FeO–MgO–Al2O3–Cr2O3–SiO2, and applications: Contributions to Mineralogy and Petrology, v. 145, p. 217–227, doi:10.1007/s00410-003-0444-3.

Liu, J., Carlson, R.W., Rudnick, R.L., Walker, R.J., Gao, S., and Wu, F., 2012, Comparative Sr–Nd–Hf–Os–Pb isotope systematics of xenolithic peridotites from Yangyuan, North China Craton: Additional evidence for a

Paleoproterozoic age: Chemical Geology, v. 332–333, p. 1–14, doi:10.1016/j.chemgeo.2012.09.013.

Liu, C.-Z., Snow, J.E., Hellebrand, E., Brügmann, G., von der Handt, A., Büchl, A., and Hofmann, A.W., 2008, Ancient, highly heterogeneous mantle beneath Gakkel ridge, Arctic Ocean: Nature, v. 452, p. 311–316, doi:10.1038/nature06688.

Loubet, M., Shimizu, N., and Allègre, C.J., 1975, Rare earth elements in alpine peridotites: Contributions to Mineralogy and Petrology, v. 53, p. 1–12, doi:10.1007/BF00402450.

Mallick, S., Dick, H.J.B., Sachi-Kocher, A., and Salters, V.J.M., 2014, Isotope and trace element insights into heterogeneity of subridge mantle: Geochemistry, Geophysics, Geosystems, v. 15, p. 2438–2453, doi:10.1002/2014GC005314.

McDonough, W.F., 1990, Constraints on the composition of the continental lithospheric mantle: Earth and Planetary Science Letters, v. 101, p. 1–18, doi:10.1016/0012-821X(90)90119-I.

Metcalfe, I., 2013, Gondwana dispersion and Asian accretion: Tectonic and palaeogeographic evolution of eastern Tethys: Journal of Asian Earth Sciences, v. 66, p. 1–33, doi:10.1016/j.jseaes.2012.12.020.

Michael, P.J., and Bonatti, E., 1985, Peridotite composition from the North Atlantic: regional and tectonic variations and implications for partial melting: Earth and Planetary Science Letters, v. 73, p. 91–104, doi:10.1016/0012-821X(85)90037-8.

Nam, T.N., Sano, Y., Terada, K., Toriumi, M., Van Quynh, P., and Dung, L.T., 2001, First SHRIMP U–Pb zircon dating of granulites from the Kontum massif (Vietnam) and tectonothermal implications: Journal of Asian Earth Sciences, v. 19, p. 77–84, doi:10.1016/S1367-9120(00)00015-8.

Navon, O., and Stolper, E., 1987, Geochemical Consequences of Melt Percolation: The Upper Mantle as a Chromatographic Column: The Journal of Geology, v. 95, p. 285–307, doi:10.1086/629131.

Nguyen, T.C., and Kil, Y., 2019, The evolution of the lithospheric mantle beneath Ia Bang, Pleiku plateau, Central Vietnam: Journal of Asian Earth Sciences, v. 174, p. 232–244, doi:10.1016/j.jseaes.2018.12.011.

Orejana, D., and Villaseca, C., 2008, Heterogeneous metasomatism in cumulate xenoliths from the Spanish Central System: Implications for percolative fractional crystallization of lamprophyric melts: Geological Society Special Publication, v. 293, p. 120, doi:10.1144/SP293.6.

Pan, S., Zheng, J., Chu, L., and Griffin, W.L., 2013, Coexistence of the moderately refractory and fertile mantle beneath the eastern Central Asian Orogenic Belt: Construction and Destruction of Cratons, v. 23, p. 176–189, doi:10.1016/j.gr.2012.03.001.

Phach, P.V., and Anh, L.D., 2018, Tectonic evolution of the southern part of Central Viet Nam and the adjacent area: Geodynamics & Tectonophysics, v. 9, p. 801–825, doi:10.5800/GT-2018-9-3-0372.

Putirka, K.D., 2008, Thermometers and Barometers for Volcanic Systems: Reviews in Mineralogy and Geochemistry, v. 69, p. 61–120, doi:10.2138/rmg.2008.69.3.

Rohrmann, A., Kapp, P., Carrapa, B., Reiners, P.W., Guynn, J., Ding, L., and Heizler, M., 2012, Thermochronologic evidence for plateau formation in central Tibet by 45 Ma: Geology, v. 40, p. 187–190, doi:10.1130/G32530.1.

Royden, L.H., Burchfiel, B.C., and van der Hilst, R.D., 2008, The Geological Evolution of the Tibetan Plateau: Science, v. 321, p. 1054–1058, doi:10.1126/science.1155371.

Rudnick, R.L., and Fountain, D.M., 1995, Nature and composition of the continental crust: A lower crustal perspective: Reviews of Geophysics, v. 33, p. 267–309, doi:10.1029/95RG01302.

Salters, V.J.M., Mallick, S., Hart, S.R., Langmuir, C.E., and Stracke, A., 2011, Domains of depleted mantle: New evidence from hafnium and neodymium isotopes: Geochemistry, Geophysics, Geosystems, v. 12, doi:10.1029/2011GC003617.

Salters, V.J.M., and Stracke, A., 2004, Composition of the depleted mantle: Geochemistry, Geophysics, Geosystems, v. 5, doi:10.1029/2003GC000597.

Scott, J.M., Hodgkinson, A., Palin, J.M., Waight, T.E., Van der Meer, Q.H.A., and Cooper, A.F., 2014, Ancient melt depletion overprinted by young carbonatitic metasomatism in the New Zealand lithospheric mantle: Contributions to Mineralogy and Petrology, v. 167, p. 963, doi:10.1007/s00410-014-0963-0.

Shaw, D.M., 1970, Trace element fractionation during anatexis: Geochimica et Cosmochimica Acta, v. 34, p. 237–243, doi:10.1016/0016-7037(70)90009-8.

Shellnutt, J.G., Lan, C.-Y., Van Long, T., Usuki, T., Yang, H.-J., Mertzman, S.A., Iizuka, Y., Chung, S.-L., Wang, K.-L., and Hsu, W.-Y., 2013, Formation of Cretaceous Cordilleran and post-orogenic granites and their microgranular enclaves from the Dalat zone, southern Vietnam: Tectonic implications for the evolution of Southeast Asia: Lithos, v. 182–183, p. 229–241, doi:10.1016/j.lithos.2013.09.016.

Stracke, A., 2012, Earth's heterogeneous mantle: A product of convection-driven interaction between crust and mantle: Chemical Geology, v. 330–331, p. 274–299, doi:10.1016/j.chemgeo.2012.08.007.

Stracke, A., Genske, F., Berndt, J., and Koornneef, J.M., 2019, Ubiquitous ultra-depleted domains in Earth's mantle: Nature Geoscience, v. 12, p. 851–855, doi:10.1038/s41561-019-0446-z.

Stracke, A., Snow, J.E., Hellebrand, E., von der Handt, A., Bourdon, B., Birbaum, K., and Günther, D., 2011, Abyssal peridotite Hf isotopes identify extreme mantle depletion: Earth and Planetary Science Letters, v. 308, p. 359–368, doi:10.1016/j.epsl.2011.06.012.

Sun, S-S., and McDonough, W.F., 1989, Chemical and isotopic systematics of oceanic basalts: implications for mantle composition and processes: Geological Society, London, Special Publications, v. 42, p. 313–345, doi:10.1144/GSL.SP.1989.042.01.19.

Toramaru, A., and Fujii, N., 1986, Connectivity of melt phase in a partially molten peridotite: Journal of Geophysical Research: Solid Earth, v. 91, p. 9239–9252, doi:10.1029/JB091iB09p09239.

Turcotte, D., and Schubert, G., 2002, Geodynamics, in Geodynamics, by Donald L. Turcotte and Gerald Schubert, pp. 472. ISBN 0521661862. Cambridge, UK: Cambridge University Press, March 2002., v. 450, doi:10.1017/CBO9780511807442.

Warren, J.M., 2016, Global variations in abyssal peridotite compositions: Lithos, v. 248–251, p. 193–219, doi:10.1016/j.lithos.2015.12.023.

Wittig, N., Webb, M., Pearson, D.G., Dale, C.W., Ottley, C.J., Hutchison, M., Jensen, S.M., and Luguet, A., 2010, Formation of the North Atlantic Craton: Timing and mechanisms constrained from Re–Os isotope and PGE data of peridotite xenoliths from S.W. Greenland: Chemical Geology, v. 276, p. 166–187, doi:10.1016/j.chemgeo.2010.06.002.

Workman, R.K., and Hart, S.R., 2005, Major and trace element composition of the depleted MORB mantle (DMM): Earth and Planetary Science Letters, v. 231, p. 53–72, doi:10.1016/j.epsl.2004.12.005.

Yu, Y., Hung, T.D., Yang, T., Xue, M., Liu, K.H., and Gao, S.S., 2017, Lateral variations of crustal structure beneath the Indochina Peninsula: Tectonophysics, v. 712–713, p. 193–199, doi:10.1016/j.tecto.2017.05.023.

Zhu, M., Graham, S., and McHargue, T., 2009, The Red River Fault zone in the Yinggehai Basin, South China Sea: Tectonophysics, v. 476, p. 397–417, doi:10.1016/j.tecto.2009.06.015.

APPENDIX A. Mineral Major Element Data

Appendix 1. Average major element compositions of core (c) and rim (r) measurements for Vietnam xenoliths. PL = Pleiku and XL = Xuan Loc

Sample	**PL-1 (C)**								**PL-1 (R)**							
	Sp		Opx		Cpx		Ol		Sp		Opx		Cpx		Ol	
	n = 5		n = 3		n = 5		n = 4		n = 5		n = 4		n = 5		n = 4	
SiO_2	0.22	±0.04	56.13	±0.11	52.19	±0.67	41.03	±0.38	0.19	±0.03	56.56	±0.12	51.71	±1.03	41.26	±0.14
TiO_2	0.05	±0.01	0.05	±0.01	0.20	±0.02	-		0.06	±0.02	0.05	±0.01	0.18	±0.02	-	
Al_2O_3	52.90	±0.41	3.39	±0.11	5.52	±0.26	-		52.77	±0.53	2.98	±0.11	4.58	±0.21	-	
Cr_2O_3	15.14	±0.64	0.41	±0.03	1.05	±0.06	-		14.99	±0.55	0.31	±0.02	0.84	±0.10	-	
FeO	11.90	±0.19	6.35	±0.06	2.29	±0.03	9.70	±0.04	11.68	±0.16	6.30	±0.06	2.26	±0.03	9.57	±0.08
MnO	0.14	±0.01	0.15	±0.01	0.07	±0.01	0.14	±0.00	0.14	±0.00	0.14	±0.00	0.07	±0.01	0.14	±0.01
MgO	19.51	±0.11	33.21	±0.10	15.39	±0.18	48.72	±0.08	19.65	±0.17	33.61	±0.14	15.91	±0.26	48.77	±0.11
CaO	-		0.49	±0.03	22.30	±0.43	0.04	±0.00	-		0.45	±0.01	23.05	±0.35	0.04	±0.00
Na_2O	0.05	±0.02	0.04	±0.01	1.47	±0.06	-		0.04	±0.04	0.04	±0.00	1.32	±0.05	-	
NiO	0.36	±0.02	0.10	±0.02	0.04	±0.01	0.39	±0.01	0.35	±0.02	0.09	±0.01	0.03	±0.01	0.38	±0.01
TOTAL	100.3		100.3		100.5		100.0		99.9		100.5		100.0		100.2	

Sample	**PL-2 (C)**								**PL-2 (R)**							
	n = 4		n = 4		n = 4		n = 5		n = 4		n = 2		n = 4		n = 3	
SiO_2	0.18	±0.02	55.70	±0.21	53.27	±0.17	41.06	±0.30	0.15	±0.02	55.56	±1.17	53.64	±0.48	41.26	±0.15
TiO_2	0.05	±0.02	0.08	±0.01	0.41	±0.01	-		0.06	±0.01	0.08	±0.01	0.41	±0.01	-	
Al_2O_3	58.01	±0.27	4.13	±0.19	6.21	±0.04	-		57.47	±0.66	3.99	±0.78	5.29	±0.13	-	
Cr_2O_3	10.41	±0.21	0.40	±0.05	0.87	±0.03	-		10.30	±0.17	0.37	±0.16	0.68	±0.03	-	
FeO	10.09	±0.04	6.03	±0.13	2.17	±0.03	9.21	±0.05	10.02	±0.08	5.91	±0.14	2.18	±0.01	9.23	±0.06
MnO	0.11	±0.00	0.14	±0.00	0.10	±0.00	0.13	±0.01	0.12	±0.01	0.14	±0.00	0.10	±0.00	0.14	±0.00
MgO	20.88	±0.20	33.09	±0.07	14.59	±0.07	48.99	±0.48	20.56	±0.34	32.77	±1.05	14.87	±0.14	49.08	±0.15
CaO	-		0.48	±0.04	21.11	±0.13	0.03	±0.00	-		0.45	±0.01	21.19	±0.16	0.03	±0.00
Na_2O	0.05	±0.04	0.07	±0.01	1.80	±0.01	-		-		0.06	±0.00	1.66	±0.03	-	
NiO	0.40	±0.01	0.09	±0.01	0.04	±0.00	0.41	±0.02	0.39	±0.01	0.09	±0.01	0.04	±0.00	0.41	±0.02
TOTAL	100.2		100.2		100.6		99.8		99.1		99.4		100.1		100.2	

Appendix 1. (continued)

Sample	**PL-3 (C)**								**PL-3 (R)**							
Mineral	Sp		Opx		Cpx		Ol		Sp		Opx		Cpx		Ol	
	n = 5		n = 5		n = 5		n = 5		n = 5		n = 4		n = 3		n = 4	
SiO_2	0.18	±0.02	55.81	±0.39	52.97	±0.36	41.06	±0.34	0.16	±0.02	56.09	±0.25	53.41	±0.51	40.97	±0.31
TiO_2	0.04	±0.01	0.10	±0.01	0.53	±0.03	-		0.08	±0.02	0.09	±0.01	0.53	±0.02	-	
Al_2O_3	57.86	±0.42	3.93	±0.45	6.34	±0.21	-		57.44	±0.31	3.69	±0.38	5.63	±0.17	-	
Cr_2O_3	10.62	±0.25	0.38	±0.07	0.91	±0.03	-		10.56	±0.30	0.33	±0.07	0.75	±0.03	-	
FeO	10.39	±0.07	6.32	±0.03	2.27	±0.01	9.69	±0.09	10.26	±0.08	6.27	±0.03	2.25	±0.05	9.58	±0.06
MnO	0.12	±0.01	0.14	±0.01	0.10	±0.01	0.14	±0.01	0.12	±0.00	0.14	±0.00	0.10	±0.00	0.13	±0.00
MgO	20.55	±0.10	33.01	±0.28	14.37	±0.21	48.67	±0.21	20.47	±0.06	33.21	±0.13	14.87	±0.30	48.30	±0.44
CaO	-		0.49	±0.06	20.94	±0.28	0.04	±0.00	-		0.47	±0.02	21.04	±0.44	0.04	±0.00
Na_2O	0.02	±0.02	0.07	±0.01	1.82	±0.04	-		-		0.06	±0.01	1.67	±0.06	-	
NiO	0.39	±0.00	0.09	±0.00	0.04	±0.00	0.40	±0.01	0.39	±0.03	0.10	±0.02	0.04	±0.00	0.39	±0.02
TOTAL	100.2		100.3		100.3		100.0		99.5		100.5		100.3		99.4	

Sample	**PL-5 (C)**								**PL-5 (R)**							
	n = 5		n = 5		n = 5		n = 5		n = 4		n = 3		n = 2		n = 3	
SiO_2	0.20	±0.02	55.16	±0.08	51.90	±0.70	40.91	±0.12	0.20	±0.01	55.25	±0.09	51.10	±0.10	40.91	±0.21
TiO_2	0.15	±0.02	0.16	±0.01	0.60	±0.03	-		0.16	±0.01	0.16	±0.01	0.56	±0.03	-	
Al_2O_3	58.98	±0.09	4.43	±0.06	7.09	±0.06	-		58.97	±0.21	4.50	±0.10	7.05	±0.03	-	
Cr_2O_3	7.58	±0.08	0.28	±0.02	0.63	±0.02	-		7.56	±0.08	0.28	±0.01	0.60	±0.02	0.01	±0.01
FeO	11.95	±0.04	6.86	±0.04	3.21	±0.03	10.65	±0.07	11.84	±0.16	6.85	±0.05	3.20	±0.04	10.65	±0.10
MnO	0.11	±0.01	0.15	±0.01	0.09	±0.00	0.15	±0.00	0.12	±0.00	0.16	±0.00	0.10	±0.00	0.15	±0.01
MgO	20.62	±0.06	31.98	±0.02	14.90	±0.05	47.71	±0.17	20.74	±0.02	32.00	±0.13	14.80	±0.13	47.57	±0.26
CaO	-		0.70	±0.03	20.19	±0.32	0.06	±0.00	-		0.69	±0.03	20.41	±0.11	0.08	±0.01
Na_2O	0.01	±0.01	0.12	±0.01	1.93	±0.02	-		-		0.11	±0.01	1.94	±0.03	-	
NiO	0.42	±0.00	0.10	±0.01	0.05	±0.01	0.38	±0.01	0.39	±0.01	0.09	±0.01	0.05	±0.01	0.37	±0.01
TOTAL	100.0		99.9		100.6		99.9		100.0		100.1		99.8		99.7	

Appendix 1. (continued)

Sample	**PL-6 (C)**								**PL-6 (R)**							
Mineral	Sp		Opx		Cpx		Ol		Sp		Opx		Cpx		Ol	
	n = 4		n = 5		n = 5		n = 3		n = 5		n = 3		n = 2		n = 3	
SiO_2	0.17	±0.01	55.82	±0.25	51.44	±0.48	41.11	±0.08	0.18	±0.01	56.17	±0.26	52.28	±1.06	41.15	±0.13
TiO_2	0.06	±0.01	0.10	±0.01	0.38	±0.02	-		0.07	±0.03	0.09	±0.01	0.39	±0.00	-	
Al_2O_3	58.18	±0.16	3.90	±0.29	6.75	±0.06	-		58.30	±0.18	3.58	±0.10	5.67	±0.05	-	
Cr_2O_3	10.03	±0.15	0.35	±0.05	0.86	±0.01	-		9.99	±0.15	0.30	±0.02	0.70	±0.03	-	
FeO	10.36	±0.05	6.36	±0.07	2.34	±0.08	9.87	±0.08	10.37	±0.04	6.33	±0.07	2.24	±0.02	9.89	±0.09
MnO	0.12	±0.00	0.15	±0.01	0.09	±0.01	0.14	±0.00	0.12	±0.00	0.14	±0.00	0.08	±0.01	0.14	±0.00
MgO	20.46	±0.08	32.90	±0.13	14.74	±0.07	48.39	±0.15	20.43	±0.08	33.28	±0.09	15.28	±0.13	48.32	±0.39
CaO	-		0.47	±0.03	21.84	±0.26	0.04	±0.00	-		0.46	±0.01	22.07	±0.35	0.04	±0.00
Na_2O	0.03	±0.02	0.05	±0.00	1.85	±0.04	-		0.03	±0.01	0.05	±0.01	1.65	±0.01	-	
NiO	0.37	±0.02	0.09	±0.01	0.03	±0.01	0.37	±0.03	0.38	±0.03	0.08	±0.01	0.04	±0.00	0.35	±0.01
TOTAL	99.8		100.2		100.3		99.9		99.9		100.5		100.4		99.9	
Sample	**PL-7 (C)**								**PL-7 (R)**							
	n = 5		n = 5		n = 5		n = 2		n = 5		n = 4		n = 5		n = 3	
SiO_2	0.18	±0.01	55.59	±0.45	52.79	±0.12	40.82	±0.20	0.16	±0.01	55.75	±0.47	52.96	±0.55	41.18	±0.15
TiO_2	0.05	±0.02	0.10	±0.01	0.48	±0.02	-		0.06	±0.02	0.09	±0.01	0.46	±0.03	-	
Al_2O_3	58.13	±0.14	4.11	±0.52	6.63	±0.30	0.02	±0.03	57.89	±0.38	3.84	±0.45	5.91	±0.74	-	
Cr_2O_3	9.55	±0.12	0.37	±0.07	0.88	±0.05	-		9.58	±0.16	0.33	±0.08	0.77	±0.13	-	
FeO	11.15	±0.04	6.54	±0.09	2.45	±0.01	10.09	±0.10	11.10	±0.07	6.44	±0.11	2.46	±0.02	10.11	±0.08
MnO	0.12	±0.01	0.15	±0.01	0.10	±0.01	0.14	±0.00	0.12	±0.01	0.14	±0.01	0.10	±0.01	0.14	±0.00
MgO	20.44	±0.07	32.68	±0.39	14.25	±0.13	49.07	±1.00	20.44	±0.13	32.76	±0.45	14.53	±0.43	48.58	±0.08
CaO	-		0.56	±0.13	20.82	±0.33	0.04	±0.01	-		0.51	±0.08	21.04	±0.30	0.03	±0.00
Na_2O	0.03	±0.01	0.06	±0.01	1.78	±0.07	0.02	±0.03	0.02	±0.03	0.06	±0.01	1.64	±0.14	-	
NiO	0.40	±0.03	0.09	±0.01	0.04	±0.00	0.41	±0.01	0.40	±0.03	0.09	±0.01	0.04	±0.01	0.40	±0.01
TOTAL	100.0		100.2		100.2		100.6		99.8		100.0		99.9		100.5	

Appendix 1. (continued)

Sample	**PL-8 (C)**								**PL-8 (R)**							
Mineral	Sp		Opx		Cpx		Ol		Sp		Opx		Cpx		Ol	
	n = 5		n = 5		n = 5		n = 4		n = 5		n = 4		n = 4		n = 4	
SiO_2	0.19	±0.01	54.97	±0.10	52.83	±0.12	40.49	±0.12	0.20	±0.02	55.01	±0.19	53.25	±0.44	40.42	±0.39
TiO_2	0.07	±0.02	0.07	±0.01	0.36	±0.02	-		0.10	±0.03	0.07	±0.00	0.34	±0.01	-	
Al_2O_3	58.16	±0.71	4.32	±0.08	6.53	±0.12	-		58.47	±0.21	4.28	±0.02	6.21	±0.10	-	
Cr_2O_3	7.84	±0.04	0.27	±0.01	0.63	±0.02	-		7.86	±0.06	0.27	±0.00	0.55	±0.01	-	
FeO	13.90	±0.07	8.48	±0.05	3.61	±0.01	13.58	±0.21	13.87	±0.09	8.39	±0.16	3.61	±0.02	13.44	±0.10
MnO	0.13	±0.01	0.17	±0.01	0.12	±0.00	0.17	±0.01	0.13	±0.00	0.17	±0.01	0.12	±0.00	0.17	±0.00
MgO	19.28	±0.06	31.08	±0.03	14.39	±0.10	45.88	±0.31	19.28	±0.08	30.99	±0.25	14.80	±0.19	45.71	±0.41
CaO	-		0.68	±0.01	19.81	±0.17	0.06	±0.00	-		0.69	±0.00	19.81	±0.18	0.06	±0.00
Na_2O	0.01	±0.02	0.10	±0.01	1.70	±0.02	-		-		0.10	±0.01	1.71	±0.04	-	
NiO	0.38	±0.02	0.09	±0.01	0.04	±0.00	0.33	±0.01	0.39	±0.02	0.08	±0.01	0.04	±0.00	0.33	±0.01
TOTAL	100.0		100.2		100.0		100.5		100.3		100.1		100.4		100.1	

Sample	**PL-9 (C)**								**PL-9 (R)**							
	n = 5		n = 5		n = 5		n = 5		n = 3		n = 3		n = 3		n = 5	
SiO_2	0.17	±0.01	55.74	±0.21	52.92	±0.13	40.95	±0.38	0.16	±0.02	56.33	±0.06	52.76	±0.38	41.05	±0.22
TiO_2	0.04	±0.01	0.10	±0.02	0.48	±0.03	-		0.04	±0.02	0.08	±0.00	0.52	±0.03	-	
Al_2O_3	58.32	±0.23	3.95	±0.29	6.57	±0.33	0.03	±0.06	58.18	±0.17	3.37	±0.21	5.76	±0.38	-	
Cr_2O_3	10.04	±0.22	0.36	±0.04	0.88	±0.04	-		9.97	±0.28	0.28	±0.03	0.78	±0.11	-	
FeO	10.47	±0.04	6.32	±0.13	2.37	±0.05	9.85	±0.10	10.47	±0.06	6.23	±0.11	2.25	±0.05	9.85	±0.06
MnO	0.12	±0.01	0.15	±0.00	0.10	±0.01	0.14	±0.00	0.12	±0.00	0.15	±0.00	0.10	±0.01	0.14	±0.00
MgO	20.54	±0.11	32.89	±0.18	14.42	±0.11	48.46	±0.25	20.48	±0.07	33.24	±0.16	14.70	±0.27	48.32	±0.29
CaO	-		0.46	±0.03	21.10	±0.22	0.04	±0.01	-		0.45	±0.00	21.59	±0.17	0.04	±0.00
Na_2O	0.01	±0.01	0.05	±0.00	1.75	±0.08	-		0.02	±0.01	0.05	±0.01	1.58	±0.05	-	
NiO	0.38	±0.01	0.08	±0.01	0.04	±0.01	0.38	±0.01	0.38	±0.02	0.08	±0.00	0.03	±0.01	0.39	±0.01
TOTAL	100.1		100.1		100.6		99.9		99.8		100.3		100.1		99.8	

Appendix 1. (continued)

Sample	XL-1 (C)								XL-1 (R)							
Mineral	Sp		Opx		Cpx		Ol		Sp		Opx		Cpx		Ol	
	n = 5		-		n = 4		n = 5		n = 4		-		n = 5		n = 5	
SiO_2	0.21	±0.05	-		54.00	±0.25	41.00	±0.11	0.22	±0.07	-		54.52	±0.47	40.80	±0.29
TiO_2	0.68	±0.04	-		0.28	±0.01	-		0.68	±0.06	-		0.26	±0.02	-	
Al_2O_3	23.98	±0.43	-		2.18	±0.13	-		24.13	±0.49	-		1.76	±0.23	-	
Cr_2O_3	35.25	±0.12	-		0.82	±0.07	-		35.30	±0.62	-		0.61	±0.13	-	
FeO	26.10	±0.49	-		2.71	±0.10	10.50	±0.09	25.55	±0.40	-		2.58	±0.05	10.48	±0.14
MnO	0.29	±0.01	-		0.11	±0.01	0.16	±0.01	0.28	±0.01	-		0.11	±0.01	0.15	±0.00
MgO	12.95	±0.29	-		16.28	±0.31	48.27	±0.13	13.44	±0.13	-		16.50	±0.12	48.03	±0.25
CaO	-		-		23.42	±0.11	0.03	±0.00	-		-		23.41	±0.32	0.03	±0.00
Na_2O	0.03	±0.04	-		0.54	±0.16	-		0.09	±0.14	-		0.48	±0.13	-	
NiO	0.22	±0.01	-		0.03	±0.00	0.32	±0.01	0.23	±0.03	-		0.04	±0.00	0.31	±0.01
TOTAL	99.7		-		100.4		100.3		99.9		-		100.3		99.8	

Sample	XL-3 (C)								XL-3 (R)							
	n = 5		n = 5		n = 5		n = 4		n = 4		n = 4		n = 4		n = 3	
SiO_2	0.20	±0.01	56.20	±0.41	53.23	±0.15	41.37	±0.02	0.16	±0.03	56.34	±0.36	53.45	±0.26	41.20	±0.22
TiO_2	0.05	±0.01	0.08	±0.01	0.38	±0.01	-		0.07	±0.01	0.08	±0.01	0.41	±0.03	-	
Al_2O_3	52.86	±0.30	3.26	±0.21	5.86	±0.17	-		52.39	±0.47	3.29	±0.26	5.30	±0.27	-	
Cr_2O_3	15.81	±0.34	0.42	±0.05	1.28	±0.06	-		15.98	±0.38	0.42	±0.07	1.12	±0.10	-	
FeO	10.77	±0.20	5.96	±0.07	2.24	±0.03	9.05	±0.05	10.35	±0.42	5.86	±0.06	2.12	±0.04	9.04	±0.11
MnO	0.14	±0.01	0.14	±0.01	0.10	±0.00	0.13	±0.00	0.13	±0.01	0.14	±0.00	0.09	±0.00	0.13	±0.01
MgO	19.75	±0.12	33.29	±0.33	14.32	±0.09	49.24	±0.09	19.77	±0.20	33.45	±0.29	14.65	±0.29	48.87	±0.43
CaO	-		0.51	±0.11	20.61	±0.23	0.03	±0.00	-		0.43	±0.05	20.97	±0.47	0.05	±0.02
Na_2O	0.06	±0.01	0.05	±0.01	1.77	±0.04	-		0.03	±0.04	0.06	±0.02	1.66	±0.06	-	
NiO	0.33	±0.02	0.09	±0.01	0.04	±0.01	0.39	±0.01	0.34	±0.02	0.08	±0.01	0.05	±0.01	0.35	±0.05
TOTAL	100.0		100.0		99.8		100.2		99.2		100.1		99.8		99.6	

Appendix 1. (continued)

Sample	**XL-4 (C)**							**XL-4 (R)**							
Mineral	Sp		Opx		Cpx		Ol		Sp		Opx		Cpx		Ol	
	-		n = 2		n = 5		n = 5		-		-		n = 2		n = 5	
SiO_2	-		56.87	±0.01	55.50	±0.81	41.11	±0.15	-		-		55.69	±0.54	41.08	±0.17
TiO_2	-		0.09	±0.01	0.08	±0.10	-		-		-		0.05	±0.02	-	
Al_2O_3	-		2.16	±0.06	1.85	±0.30	-		-		-		1.79	±0.04	-	
Cr_2O_3	-		0.40	±0.06	0.83	±0.38	-		-		-		0.82	±0.10	-	
FeO	-		6.59	±0.10	2.50	±0.18	9.89	±0.07	-		-		2.71	±0.36	9.75	±0.06
MnO	-		0.16	±0.00	0.07	±0.01	0.15	±0.01	-		-		0.07	±0.00	0.16	±0.00
MgO	-		33.28	±0.06	16.16	±0.16	48.95	±0.21	-		-		16.05	±0.17	48.91	±0.57
CaO	-		0.56	±0.07	21.96	±0.82	0.03	±0.01	-		-		21.67	±0.11	0.02	±0.00
Na_2O	-		0.05	±0.04	1.47	±0.35	-		-		-		1.58	±0.17	-	
NiO	-		0.07	±0.00	0.03	±0.01	0.34	±0.01	-		-		0.03	±0.00	0.35	±0.02
TOTAL	-		100.2		100.4		100.5		-		-		100.5		100.3	

Sample	**XL-5 (C)**							**XL-5 (R)**							
	n = 4		n = 4		n = 5		n = 4		n = 5		n = 3		n = 5		n = 4	
SiO_2	0.19	±0.02	57.22	±0.16	54.74	±0.21	41.42	±0.11	0.22	±0.02	57.34	±0.30	54.91	±0.38	41.25	±0.51
TiO_2	0.06	±0.01	0.01	±0.00	0.03	±0.00	-		0.03	±0.02	0.02	±0.01	0.04	±0.01	-	
Al_2O_3	32.32	±0.55	2.00	±0.15	2.46	±0.18	-		32.65	±0.62	2.00	±0.16	2.26	±0.12	-	
Cr_2O_3	37.34	±0.38	0.52	±0.08	1.20	±0.12	-		37.09	±0.64	0.54	±0.09	1.05	±0.14	-	
FeO	13.76	±0.36	5.73	±0.15	1.96	±0.05	8.76	±0.05	13.61	±0.45	5.54	±0.06	1.91	±0.06	8.65	±0.05
MnO	0.24	±0.01	0.14	±0.01	0.10	±0.01	0.13	±0.01	0.23	±0.01	0.13	±0.01	0.09	±0.00	0.13	±0.01
MgO	16.13	±0.38	34.21	±0.17	16.23	±0.09	49.85	±0.18	16.22	±0.37	34.22	±0.19	16.41	±0.17	49.77	±0.31
CaO	-		0.51	±0.06	22.44	±0.11	0.03	±0.00	-		0.48	±0.05	22.74	±0.23	0.05	±0.03
Na_2O	0.05	±0.04	0.03	±0.01	0.97	±0.04	-		0.06	±0.03	0.03	±0.00	0.91	±0.05	-	
NiO	0.16	±0.01	0.08	±0.01	0.04	±0.00	0.41	±0.01	0.17	±0.02	0.08	±0.01	0.05	±0.01	0.41	±0.01
TOTAL	100.2		100.5		100.2		100.6		100.3		100.4		100.4		100.3	

Appendix 1. (continued)

Sample	XL-7 (C)								XL-7 (R)							
Mineral	Sp		Opx		Cpx		Ol		Sp		Opx		Cpx		Ol	
	n = 5		n = 4		n = 4		n = 2		n = 3		n = 5		n = 3		n = 5	
SiO_2	0.17	±0.01	55.78	±0.50	53.09	±0.60	41.20	±0.19	0.18	±0.02	55.86	±0.64	53.11	±0.59	40.73	±0.12
TiO_2	0.05	±0.02	0.10	±0.03	0.45	±0.18	-		0.08	±0.04	0.10	±0.04	0.38	±0.16	-	
Al_2O_3	58.73	±0.28	3.89	±0.46	6.36	±0.37	-		58.79	±0.53	3.75	±0.53	5.87	±0.48	-	
Cr_2O_3	9.17	±0.16	0.42	±0.18	1.01	±0.29	-		9.22	±0.26	0.37	±0.17	0.99	±0.32	-	
FeO	11.10	±0.14	6.49	±0.45	2.46	±0.21	10.43	±0.01	11.00	±0.17	6.42	±0.46	2.34	±0.20	10.34	±0.10
MnO	0.12	±0.00	0.15	±0.02	0.08	±0.01	0.14	±0.00	0.12	±0.00	0.15	±0.01	0.07	±0.00	0.14	±0.00
MgO	20.25	±0.04	32.96	±0.39	14.43	±0.20	48.42	±0.14	20.24	±0.09	33.00	±0.59	14.57	±0.24	47.95	±0.13
CaO	-		0.45	±0.03	20.83	±0.39	0.03	±0.00	-		0.58	±0.26	21.20	±0.25	0.04	±0.01
Na_2O	0.03	±0.02	0.04	±0.01	1.79	±0.07	-		0.04	±0.02	0.05	±0.03	1.72	±0.11	-	
NiO	0.38	±0.02	0.09	±0.02	0.04	±0.01	0.39	±0.00	0.38	±0.02	0.09	±0.01	0.03	±0.01	0.37	±0.02
TOTAL	100.0		100.4		100.5		100.6		100.0		100.4		100.3		99.6	

Sample	XL-8 (C)								XL-8 (R)							
	n = 5		n = 6		n = 5		n = 3		n = 2		n = 4		n = 5		n = 2	
SiO_2	0.19	±0.02	55.75	±0.50	52.02	±0.04	41.10	±0.34	0.56	±0.21	55.53	±0.49	52.61	±0.44	40.81	±0.17
TiO_2	0.06	±0.02	0.16	±0.04	0.69	±0.03	-		0.08	±0.01	0.19	±0.01	0.73	±0.06	-	
Al_2O_3	59.80	±1.98	3.75	±0.64	6.87	±0.09	0.10	±0.18	59.81	±1.55	4.12	±0.27	6.70	±0.22	-	
Cr_2O_3	8.00	±1.76	0.28	±0.05	0.82	±0.06	-		7.54	±2.49	0.33	±0.03	0.78	±0.07	-	
FeO	10.91	±0.29	6.78	±0.12	2.52	±0.05	10.61	±0.03	10.81	±0.46	6.83	±0.06	2.54	±0.13	10.57	±0.01
MnO	0.12	±0.01	0.16	±0.00	0.09	±0.01	0.15	±0.00	0.11	±0.01	0.16	±0.01	0.08	±0.01	0.16	±0.01
MgO	20.49	±0.55	32.54	±0.38	14.23	±0.09	48.14	±0.66	20.40	±0.32	32.47	±0.30	14.55	±0.45	47.98	±0.43
CaO	-		0.45	±0.05	21.33	±0.07	0.04	±0.01	-		0.50	±0.03	20.87	±0.55	0.03	±0.00
Na_2O	0.04	±0.05	0.04	±0.00	1.66	±0.04	-		0.09	±0.01	0.04	±0.01	1.61	±0.06	-	
NiO	0.39	±0.03	0.08	±0.01	0.03	±0.00	0.33	±0.00	0.36	±0.03	0.08	±0.01	0.03	±0.01	0.33	±0.00
TOTAL	100.0		100.0		100.2		100.5		99.8		100.2		100.5		99.9	

Appendix 1. (continued)

Sample	XL-9 (C)								XL-9 (R)							
Mineral	Sp		Opx		Cpx		Ol		Sp		Opx		Cpx		Ol	
	n = 5		n = 5		n = 5		n = 5		n = 5		n = 3		n = 5		n = 3	
SiO_2	0.17	±0.00	55.88	±0.25	52.97	±0.19	41.21	±0.13	0.17	±0.01	56.11	±0.31	53.30	±0.34	40.39	±1.20
TiO_2	0.03	±0.02	0.12	±0.01	0.64	±0.04	-		0.05	±0.02	0.11	±0.01	0.66	±0.05	-	
Al_2O_3	57.26	±0.19	3.78	±0.22	6.24	±0.36	-		57.29	±0.34	3.57	±0.09	5.88	±0.49	0.03	±0.06
Cr_2O_3	11.25	±0.15	0.35	±0.00	0.92	±0.07	-		11.28	±0.21	0.32	±0.03	0.84	±0.10	-	
FeO	10.49	±0.26	6.48	±0.10	2.37	±0.13	9.97	±0.07	9.99	±0.40	6.32	±0.03	2.31	±0.12	9.97	±0.10
MnO	0.12	±0.01	0.15	±0.00	0.10	±0.01	0.14	±0.01	0.12	±0.00	0.15	±0.01	0.10	±0.00	0.14	±0.01
MgO	20.29	±0.12	32.98	±0.15	14.19	±0.14	48.99	±0.40	20.46	±0.18	33.01	±0.33	14.37	±0.27	48.76	±0.36
CaO	-		0.47	±0.05	20.48	±0.26	0.03	±0.00	-		0.41	±0.04	20.69	±0.22	0.04	±0.01
Na_2O	0.03	±0.01	0.05	±0.01	1.80	±0.05	-		0.02	±0.02	0.06	±0.01	1.72	±0.07	-	
NiO	0.37	±0.01	0.08	±0.01	0.04	±0.01	0.39	±0.01	0.36	±0.03	0.08	±0.01	0.04	±0.01	0.40	±0.02
TOTAL	100.0		100.3		99.8		100.7		99.7		100.1		99.9		99.7	

Sample	XL-11 (C)								XL-11 (R)							
	n = 3		n = 4		n = 3		n = 5		n = 4		n = 4		n = 3		n = 5	
SiO_2	0.22	±0.02	57.46	±0.25	54.17	±0.21	41.54	±0.26	0.26	±0.07	57.53	±0.23	54.45	±0.58	41.29	±0.27
TiO_2	0.05	±0.01	0.01	±0.01	0.03	±0.01	-		0.04	±0.01	0.01	±0.01	0.02	±0.01	-	
Al_2O_3	32.36	±0.17	1.86	±0.14	2.72	±0.30	0.02	±0.04	32.04	±0.60	1.81	±0.20	2.78	±0.22	0.02	±0.04
Cr_2O_3	37.34	±0.21	0.47	±0.07	1.17	±0.24	-		37.00	±0.43	0.44	±0.08	1.22	±0.15	-	
FeO	13.67	±0.12	5.53	±0.03	2.01	±0.01	8.53	±0.08	13.48	±0.32	5.48	±0.10	2.06	±0.05	8.51	±0.04
MnO	0.24	±0.01	0.14	±0.01	0.07	±0.00	0.12	±0.00	0.24	±0.01	0.14	±0.00	0.07	±0.00	0.12	±0.01
MgO	16.25	±0.13	34.32	±0.14	16.55	±0.28	49.69	±0.33	16.81	±0.43	34.46	±0.18	16.39	±0.10	49.70	±0.16
CaO	-		0.46	±0.06	23.01	±0.29	0.03	±0.00	-		0.44	±0.03	22.72	±0.09	0.06	±0.04
Na_2O	0.09	±0.03	0.03	±0.01	0.94	±0.07	-		0.24	±0.22	0.04	±0.00	0.94	±0.06	-	
NiO	0.16	±0.01	0.08	±0.01	0.05	±0.01	0.40	±0.02	0.17	±0.01	0.09	±0.01	0.04	±0.01	0.39	±0.02
TOTAL	100.4		100.4		100.7		100.3		100.3		100.4		100.7		100.1	

Appendix 1. (continued)

Sample	XL-12 (C)								XL-12 (R)							
Mineral	Sp		Opx		Cpx		Ol		Sp		Opx		Cpx		Ol	
	n = 5		n = 5		n = 2		n = 4		n = 3		n = 2		n = 2		n = 3	
SiO_2	0.27	±0.09	57.09	±0.15	54.13	±0.27	41.25	±0.30	0.21	±0.01	56.74	±0.53	54.35	±0.37	41.48	±0.14
TiO_2	0.27	±0.04	0.16	±0.00	0.53	±0.02	-		0.27	±0.04	0.16	±0.02	0.46	±0.16	-	
Al_2O_3	34.56	±0.30	2.06	±0.14	3.15	±0.02	-		34.94	±0.31	2.21	±0.08	2.41	±0.67	-	
Cr_2O_3	34.52	±0.32	0.51	±0.08	1.31	±0.04	-		34.70	±0.32	0.56	±0.00	1.27	±0.25	-	
FeO	13.06	±0.30	5.60	±0.05	1.98	±0.01	8.35	±0.07	12.50	±0.15	5.55	±0.06	2.03	±0.05	8.29	±0.04
MnO	0.21	±0.00	0.13	±0.00	0.09	±0.00	0.12	±0.00	0.21	±0.01	0.13	±0.01	0.09	±0.00	0.12	±0.00
MgO	16.70	±0.34	34.32	±0.10	15.90	±0.13	50.19	±0.52	17.09	±0.22	34.00	±0.47	16.54	±0.94	50.03	±0.39
CaO	-		0.46	±0.07	22.28	±0.04	0.03	±0.01	-		0.53	±0.05	22.05	±0.49	0.05	±0.03
Na_2O	0.05	±0.04	0.04	±0.01	1.18	±0.06	-		0.06	±0.05	0.03	±0.01	1.07	±0.01	-	
NiO	0.19	±0.02	0.08	±0.00	0.04	±0.00	0.39	±0.02	0.20	±0.03	0.07	±0.01	0.04	±0.00	0.41	±0.01
TOTAL	99.8		100.5		100.6		100.3		100.2		100.0		100.3		100.4	

Sample	XL-14 (C)								XL-14 (R)							
	n = 4		n = 5		n = 5		n = 5		n = 4		n = 4		n = 3		n = 4	
SiO_2	0.17	±0.02	55.96	±0.13	52.73	±0.41	41.15	±0.15	0.18	±0.02	55.85	±0.15	52.04	±0.49	41.16	±0.11
TiO_2	0.03	±0.02	0.11	±0.01	0.56	±0.03	-		0.04	±0.02	0.11	±0.02	0.53	±0.05	-	
Al_2O_3	59.16	±0.19	3.60	±0.23	6.54	±0.33	-		59.22	±0.24	3.62	±0.34	5.64	±1.13	-	
Cr_2O_3	8.90	±0.15	0.27	±0.02	0.76	±0.05	-		8.94	±0.15	0.28	±0.04	0.69	±0.05	-	
FeO	10.59	±0.27	6.63	±0.08	2.52	±0.13	10.16	±0.10	10.44	±0.32	6.54	±0.07	2.47	±0.09	10.21	±0.06
MnO	0.12	±0.00	0.16	±0.01	0.08	±0.00	0.15	±0.00	0.12	±0.00	0.15	±0.00	0.08	±0.00	0.14	±0.00
MgO	20.47	±0.05	32.82	±0.12	14.45	±0.19	48.47	±0.51	20.61	±0.16	32.81	±0.36	14.89	±0.77	48.32	±0.28
CaO	-		0.42	±0.04	21.30	±0.54	0.03	±0.00	-		0.46	±0.09	22.24	±1.05	0.04	±0.01
Na_2O	0.02	±0.02	0.04	±0.00	1.77	±0.02	-		0.02	±0.02	0.04	±0.01	1.46	±0.38	-	
NiO	0.39	±0.02	0.08	±0.01	0.03	±0.00	0.36	±0.01	0.38	±0.02	0.07	±0.01	0.04	±0.01	0.35	±0.02
TOTAL	99.8		100.1		100.7		100.3		100.0		100.0		100.1		100.2	

Appendix 1. (continued)

Sample	**XL-15 (C)**								**XL-15 (R)**							
Mineral	Sp		Opx		Cpx		Ol		Sp		Opx		Cpx		Ol	
	n = 5		n = 5		n = 4		n = 3		n = 3		n = 5		-		n = 5	
SiO_2	0.24	±0.13	56.08	±0.25	53.53	±0.10	41.19	±0.14	0.19	±0.01	56.48	±0.34	-		41.10	±0.30
TiO_2	0.04	±0.02	0.07	±0.01	0.36	±0.01	-		0.03	±0.00	0.06	±0.01	-		-	
Al_2O_3	55.73	±0.35	3.52	±0.26	5.92	±0.29	-		56.10	±0.40	3.02	±0.22	-		-	
Cr_2O_3	12.63	±0.23	0.38	±0.04	1.02	±0.06	-		12.69	±0.39	0.28	±0.04	-		-	
FeO	10.87	±0.13	6.37	±0.05	2.45	±0.05	9.60	±0.09	9.98	±0.25	6.30	±0.09	-		9.55	±0.08
MnO	0.12	±0.01	0.15	±0.00	0.10	±0.01	0.14	±0.00	0.12	±0.00	0.15	±0.01	-		0.13	±0.00
MgO	19.99	±0.08	33.03	±0.28	14.69	±0.21	48.78	±0.09	20.40	±0.14	33.36	±0.32	-		48.84	±0.13
CaO	-		0.50	±0.13	21.33	±0.31	0.03	±0.00	-		0.39	±0.03	-		0.04	±0.03
Na_2O	0.07	±0.08	0.05	±0.01	1.82	±0.07	-		0.06	±0.01	0.03	±0.01	-		-	
NiO	0.38	±0.01	0.09	±0.01	0.04	±0.01	0.40	±0.00	0.36	±0.01	0.09	±0.01	-		0.38	±0.03
TOTAL	100.1		100.2		101.3		100.1		99.9		100.2				100.0	

Sample	**XL-16 (C)**								**XL-16 (R)**							
	n = 3		n = 5		n = 5		-		n = 4		n = 2		n = 5		-	
SiO_2	0.18	±0.01	55.94	±0.13	53.01	±0.32	-		0.17	±0.01	56.23	±0.18	53.26	±0.47	-	
TiO_2	0.01	±0.01	0.08	±0.01	0.45	±0.05	-		0.03	±0.02	0.08	±0.00	0.46	±0.02	-	
Al_2O_3	59.40	±0.13	3.74	±0.14	5.70	±1.39	-		59.40	±0.17	3.26	±0.09	5.82	±0.34	-	
Cr_2O_3	9.19	±0.17	0.31	±0.01	0.79	±0.05	-		9.19	±0.23	0.23	±0.00	0.74	±0.06	-	
FeO	10.11	±0.03	6.24	±0.11	2.36	±0.06	-		9.67	±0.32	6.06	±0.05	2.27	±0.03	-	
MnO	0.12	±0.00	0.15	±0.01	0.10	±0.01	-		0.12	±0.01	0.15	±0.01	0.10	±0.01	-	
MgO	20.74	±0.10	32.98	±0.07	14.71	±0.84	-		20.80	±0.28	33.15	±0.37	14.68	±0.20	-	
CaO	-		0.49	±0.07	21.30	±0.61	-		-		0.45	±0.08	21.37	±0.19	-	
Na_2O	0.02	±0.02	0.06	±0.01	1.49	±0.42	-		0.01	±0.02	0.05	±0.00	1.64	±0.06	-	
NiO	0.37	±0.01	0.09	±0.00	0.04	±0.00	-		0.38	±0.04	0.09	±0.00	0.04	±0.01	-	
TOTAL	100.2		100.1		100.0		-		99.8		99.7		100.4		-	

Appendix 1. (continued)

Sample	XL-18 (C)								XL-18 (R)							
Mineral	Sp		Opx		Cpx		Ol		Sp		Opx		Cpx		Ol	
	n = 5		n = 4		n = 5		n = 3		n = 4		n = 2		n = 4		n = 3	
SiO_2	0.20	±0.06	55.67	±0.06	52.14	±0.43	41.22	±0.14	0.16	±0.01	55.72	±0.50	52.27	±0.58	41.27	±0.18
TiO_2	0.06	±0.01	0.13	±0.01	0.62	±0.04	-		0.09	±0.03	0.12	±0.02	0.64	±0.02	-	
Al_2O_3	60.04	±0.57	3.86	±0.18	7.17	±0.16	-		59.81	±0.34	3.50	±0.13	6.72	±0.53	-	
Cr_2O_3	7.64	±0.33	0.26	±0.02	0.71	±0.07	-		7.64	±0.19	0.23	±0.01	0.64	±0.10	-	
FeO	11.04	±0.19	6.77	±0.07	2.69	±0.09	10.30	±0.07	11.07	±0.17	6.69	±0.08	2.63	±0.05	10.44	±0.06
MnO	0.11	±0.00	0.16	±0.01	0.09	±0.01	0.14	±0.00	0.12	±0.00	0.16	±0.00	0.09	±0.01	0.15	±0.00
MgO	20.55	±0.16	32.53	±0.12	14.08	±0.15	48.22	±0.20	20.41	±0.20	32.90	±0.08	14.29	±0.29	48.35	±0.32
CaO	-		0.52	±0.07	20.92	±0.43	0.03	±0.00	-		0.43	±0.07	21.36	±0.55	0.03	±0.00
Na_2O	0.06	±0.06	0.05	±0.01	1.88	±0.08	-	±0.00	0.02	±0.02	0.04	±0.00	1.81	±0.10	-	
NiO	0.43	±0.02	0.09	±0.01	0.05	±0.02	0.37	±0.01	0.40	±0.03	0.09	±0.00	0.04	±0.01	0.38	±0.02
TOTAL	100.1		100.1		100.3		100.3		99.7		99.9		100.5		100.6	

Sample	XL-19 (C)								XL-19 (R)							
	n = 5		n = 5		n = 5		n = 4		n = 5		n = 3		n = 5		n = 4	
SiO_2	0.18	±0.01	55.61	±0.19	52.22	±0.62	41.19	±0.13	0.17	±0.01	56.21	±0.55	52.74	±0.55	41.13	±0.29
TiO_2	0.05	±0.02	0.11	±0.01	0.43	±0.04	-		0.06	±0.01	0.09	±0.01	0.43	±0.04	-	±0.00
Al_2O_3	57.15	±0.19	3.95	±0.18	6.45	±0.37	-		57.19	±0.29	3.49	±0.46	5.69	±0.78	-	±0.00
Cr_2O_3	10.53	±0.21	0.37	±0.03	0.84	±0.10	-		10.60	±0.38	0.33	±0.07	0.77	±0.13	-	±0.00
FeO	11.53	±0.25	6.52	±0.05	2.70	±0.09	9.79	±0.08	11.28	±0.42	6.41	±0.07	2.56	±0.16	9.76	±0.09
MnO	0.12	±0.00	0.15	±0.01	0.08	±0.01	0.14	±0.00	0.12	±0.00	0.15	±0.00	0.08	±0.00	0.14	±0.00
MgO	20.13	±0.06	32.77	±0.27	14.37	±0.28	48.88	±0.10	20.13	±0.10	33.33	±0.17	14.71	±0.55	48.78	±0.32
CaO	-		0.56	±0.17	21.40	±0.27	0.03	±0.00	-		0.39	±0.06	21.82	±0.45	0.03	±0.00
Na_2O	0.04	±0.02	0.05	±0.02	1.93	±0.12	-		0.02	±0.02	0.04	±0.01	1.68	±0.30	-	±0.00
NiO	0.38	±0.02	0.07	±0.01	0.03	±0.01	0.40	±0.01	0.39	±0.01	0.08	±0.01	0.04	±0.01	0.39	±0.00
TOTAL	100.1		100.2		100.4		100.4		100.0		100.5		100.5		100.2	

Appendix 1. (continued)

Sample	XL-20 (C)								XL-20 (R)							
Mineral	Sp		Opx		Cpx		Ol		Sp		Opx		Cpx		Ol	
	n = 4		n = 5		n = 4		n = 3		n = 3		n = 4		n = 3		n = 4	
SiO_2	0.17	±0.00	55.65	±0.30	53.00	±0.33	41.12	±0.10	0.17	±0.00	55.90	±0.55	53.22	±0.22	41.16	±0.57
TiO_2	0.04	±0.01	0.09	±0.01	0.40	±0.03	-		0.02	±0.00	0.08	±0.01	0.41	±0.01	-	
Al_2O_3	57.34	±0.27	4.04	±0.37	5.93	±0.19	-		57.22	±0.24	3.60	±0.56	5.65	±0.71	-	
Cr_2O_3	11.01	±0.25	0.41	±0.07	0.86	±0.04	-		11.12	±0.32	0.36	±0.09	0.78	±0.17	-	
FeO	10.30	±0.11	6.40	±0.17	2.21	±0.17	9.68	±0.08	10.25	±0.17	6.24	±0.20	2.26	±0.01	9.58	±0.08
MnO	0.12	±0.00	0.15	±0.01	0.07	±0.01	0.14	±0.01	0.12	±0.01	0.15	±0.01	0.07	±0.01	0.13	±0.01
MgO	20.44	±0.06	32.91	±0.20	14.73	±0.07	48.80	±0.17	20.34	±0.03	32.86	±0.38	14.93	±0.41	48.67	±0.31
CaO	-		0.50	±0.10	21.52	±0.20	0.03	±0.00	-		0.38	±0.01	21.77	±0.48	0.02	±0.00
Na_2O	0.02	±0.02	0.05	±0.00	1.79	±0.28	-		0.01	±0.01	0.05	±0.02	1.62	±0.20	-	
NiO	0.37	±0.03	0.09	±0.01	0.04	±0.01	0.40	±0.02	0.36	±0.00	0.09	±0.00	0.03	±0.00	0.38	±0.01
TOTAL	99.8		100.3		100.6		100.2		99.6		99.7		100.7		100.0	

Stds	NMNH S218		NMNH 164905	
	n = 18		n = 24	
SiO_2	-		51.24	±0.78
TiO_2	-		0.52	±0.14
Al_2O_3	73.18	±0.82	7.36	±0.33
Cr_2O_3	-		0.89	±0.23
FeO	-		4.83	±0.48
MnO	-		0.13	±0.26
MgO	27.01	±0.48	16.90	±0.21
CaO	0.02		17.21	±0.66
Na_2O			0.86	±0.45
NiO	-		0.05	±0.13
TOTAL	100.2		100.0	

APPENDIX B. Clinopyroxene and Orthopyroxene Trace Element Data

Appendix B. Average trace element composition (ppm ±1σ) of clinopyroxene (cpx) and orthopyroxene (opx).

Pleiku	**PL-1**		**PL-2**		**PL-3**		**PL-5**	
Type	F		F		F		F	
Mineral	Cpx	Opx	Cpx	Opx	Cpx	Opx	Cpx	Opx
	n = 4	n = 5	n = 4	n = 5	n = 5	n = 5	n = 2	n = 5
Ti	1149 ±82	361.3 ±12.1	2246 ±80	498.8 ±30.6	2863 ±65	609.5 ±39.2	3950 ±160	897.2 ±23.3
Rb	-	0.002 ±0.009	0.010 ±0.014	0.004 ±0.008	-	0.004 ±0.011	0.008 ±0.008	0.004 ±0.005
Sr	12.78 ±0.28	0.040 ±0.034	30.91 ±0.75	0.111 ±0.073	47.43 ±0.35	0.102 ±0.146	109.9 ±6.2	0.212 ±0.051
Y	13.01 ±0.37	0.511 ±0.032	17.46 ±0.24	0.670 ±0.091	19.15 ±0.36	0.749 ±0.098	21.64 ±1.28	1.03 ±0.05
Zr	5.95 ±0.20	0.238 ±0.027	5.36 ±0.21	0.184 ±0.033	18.39 ±0.26	0.579 ±0.086	45.16 ±0.24	1.95 ±0.10
Nb	0.029 ±0.006	0.005 ±0.002	1.27 ±0.14	0.023 ±0.009	0.120 ±0.018	0.004 ±0.002	0.958 ±0.085	0.027 ±0.007
La	0.118 ±0.006	0.001 ±0.001	0.656 ±0.066	0.004 ±0.003	0.908 ±0.313	0.007 ±0.009	3.56 ±0.22	0.007 ±0.001
Ce	0.616 ±0.013	0.004 ±0.004	0.938 ±0.034	0.004 ±0.003	1.92 ±0.17	0.008 ±0.010	8.43 ±0.60	0.023 ±0.004
Pr	0.139 ±0.002	0.001 ±0.001	0.189 ±0.007	0.001 ±0.001	0.380 ±0.011	0.001 ±0.001	1.16 ±0.09	0.005 ±0.001
Nd	0.986 ±0.041	0.006 ±0.006	1.48 ±0.039	0.012 ±0.005	2.77 ±0.10	0.011 ±0.010	5.67 ±0.19	0.029 ±0.004
Sm	0.743 ±0.043	0.007 ±0.004	0.946 ±0.029	0.009 ±0.005	1.40 ±0.03	0.011 ±0.006	2.07 ±0.16	0.020 ±0.005
Eu	0.312 ±0.009	0.003 ±0.001	0.425 ±0.017	0.004 ±0.001	0.606 ±0.017	0.005 ±0.002	0.820 ±0.052	0.012 ±0.002
Gd	1.35 ±0.07	0.021 ±0.002	1.83 ±0.04	0.024 ±0.010	2.28 ±0.07	0.029 ±0.004	2.98 ±0.13	0.050 ±0.008
Tb	0.274 ±0.017	0.008 ±0.002	0.367 ±0.007	0.007 ±0.001	0.437 ±0.006	0.008 ±0.002	0.522 ±0.036	0.012 ±0.002
Dy	2.25 ±0.08	0.064 ±0.011	2.99 ±0.141	0.087 ±0.021	3.34 ±0.07	0.081 ±0.014	4.01 ±0.22	0.133 ±0.009
Ho	0.494 ±0.028	0.019 ±0.002	0.682 ±0.016	0.027 ±0.007	0.752 ±0.034	0.028 ±0.006	0.838 ±0.022	0.040 ±0.004
Er	1.57 ±0.07	0.074 ±0.015	2.10 ±0.03	0.108 ±0.023	2.22 ±0.11	0.118 ±0.005	2.47 ±0.16	0.144 ±0.012
Tm	0.232 ±0.010	0.016 ±0.001	0.294 ±0.023	0.022 ±0.002	0.320 ±0.016	0.026 ±0.003	0.358 ±0.007	0.028 ±0.003
Yb	1.52 ±0.09	0.168 ±0.016	2.00 ±0.05	0.195 ±0.025	2.10 ±0.02	0.197 ±0.013	2.22 ±0.11	0.251 ±0.017
Lu	0.224 ±0.019	0.031 ±0.004	0.286 ±0.009	0.034 ±0.005	0.290 ±0.015	0.041 ±0.002	0.308 ±0.016	0.047 ±0.003
Hf	0.279 ±0.021	0.015 ±0.004	0.326 ±0.019	0.015 ±0.005	0.676 ±0.019	0.030 ±0.003	1.34 ±0.01	0.052 ±0.006
Pb	0.017 ±0.005	0.007 ±0.002	0.074 ±0.002	0.004 ±0.002	0.031 ±0.007	0.007 ±0.004	0.287 ±0.030	0.027 ±0.043
Th	0.005 ±0.001	0.003 ±0.001	0.048 ±0.007	0.004 ±0.001	0.015 ±0.006	0.004 ±0.002	0.214 ±0.009	0.004 ±0.003
U	0.005 ±0.000	0.002 ±0.003	0.135 ±0.011	0.006 ±0.002	0.010 ±0.004	0.002 ±0.002	0.066 ±0.006	0.004 ±0.001

Appendix B. (continued)

Pleiku	**PL-6**		**PL-7**		**PL-8**		**PL-9**	
Type	F		F		F		F	
Mineral	Cpx	Opx	Cpx	Opx	Cpx	Opx	Cpx	Opx
	n = 5	n = 5	n = 5	n = 5	n = 5	n = 5	n = 5	n = 5
Ti	2454 ±186	609.1 ±26.4	2494 ±136	566.8 ±50.2	1453 ±36	433.7 ±11.4	2660 ±166	574.6 ±60.2
Rb	-	0.003 ±0.005	0.006 ±0.009	0.000 ±0.004	0.005 ±0.015	0.005 ±0.007	0.004 ±0.011	-
Sr	25.14 ±1.07	0.033 ±0.025	34.96 ±0.24	0.089 ±0.112	103.4 ±3.3	0.172 ±0.010	24.63 ±0.31	0.018 ±0.006
Y	19.26 ±0.65	0.631 ±0.069	17.29 ±0.38	0.632 ±0.115	9.36 ±0.17	0.467 ±0.022	18.64 ±0.81	0.638 ±0.046
Zr	13.90 ±0.80	0.448 ±0.074	14.23 ±0.69	0.517 ±0.183	7.65 ±0.19	0.332 ±0.034	14.12 ±0.95	0.430 ±0.074
Nb	0.087 ±0.018	0.004 ±0.001	0.078 ±0.016	0.006 ±0.002	0.696 ±0.07	0.015 ±0.004	0.083 ±0.019	0.003 ±0.001
La	0.213 ±0.011	0.001 ±0.000	0.267 ±0.006	0.001 ±0.001	1.01 ±0.11	0.002 ±0.001	0.208 ±0.007	0.001 ±0.001
Ce	1.07 ±0.05	0.002 ±0.001	1.32 ±0.04	0.004 ±0.005	1.75 ±0.22	0.007 ±0.002	1.01 ±0.05	0.001 ±0.001
Pr	0.287 ±0.015	0.001 ±0.000	0.330 ±0.012	0.001 ±0.001	0.229 ±0.017	0.001 ±0.001	0.279 ±0.011	0.000 ±0.000
Nd	2.15 ±0.09	0.008 ±0.006	2.46 ±0.070	0.009 ±0.004	1.29 ±0.04	0.010 ±0.004	2.25 ±0.05	0.005 ±0.002
Sm	1.36 ±0.06	0.007 ±0.004	1.25 ±0.041	0.011 ±0.004	0.714 ±0.015	0.011 ±0.002	1.30 ±0.05	0.005 ±0.002
Eu	0.554 ±0.015	0.003 ±0.000	0.547 ±0.019	0.006 ±0.002	0.437 ±0.006	0.007 ±0.001	0.557 ±0.014	0.004 ±0.001
Gd	2.24 ±0.05	0.024 ±0.007	2.04 ±0.056	0.023 ±0.010	1.24 ±0.01	0.024 ±0.001	2.15 ±0.07	0.021 ±0.005
Tb	0.423 ±0.015	0.008 ±0.002	0.389 ±0.015	0.008 ±0.001	0.237 ±0.009	0.006 ±0.002	0.424 ±0.012	0.007 ±0.001
Dy	3.36 ±0.16	0.081 ±0.011	3.13 ±0.13	0.079 ±0.020	1.79 ±0.03	0.069 ±0.006	3.29 ±0.14	0.076 ±0.010
Ho	0.730 ±0.030	0.022 ±0.002	0.670 ±0.032	0.025 ±0.006	0.388 ±0.018	0.020 ±0.004	0.730 ±0.037	0.024 ±0.005
Er	2.20 ±0.10	0.103 ±0.018	2.00 ±0.07	0.101 ±0.013	1.15 ±0.04	0.078 ±0.009	2.19 ±0.11	0.102 ±0.010
Tm	0.325 ±0.011	0.022 ±0.002	0.301 ±0.016	0.020 ±0.003	0.165 ±0.008	0.015 ±0.002	0.321 ±0.023	0.021 ±0.004
Yb	2.16 ±0.09	0.189 ±0.013	1.94 ±0.07	0.201 ±0.038	1.09 ±0.04	0.127 ±0.015	2.10 ±0.12	0.186 ±0.023
Lu	0.310 ±0.013	0.039 ±0.006	0.281 ±0.019	0.032 ±0.006	0.154 ±0.010	0.027 ±0.004	0.309 ±0.015	0.037 ±0.005
Hf	0.616 ±0.047	0.024 ±0.007	0.578 ±0.017	0.026 ±0.005	0.325 ±0.015	0.014 ±0.003	0.601 ±0.038	0.022 ±0.009
Pb	0.031 ±0.008	0.007 ±0.003	0.044 ±0.002	0.009 ±0.002	0.105 ±0.004	0.009 ±0.002	0.031 ±0.003	0.008 ±0.002
Th	0.011 ±0.006	0.003 ±0.001	0.010 ±0.002	0.004 ±0.002	0.202 ±0.013	0.004 ±0.001	0.012 ±0.004	0.003 ±0.002
U	0.005 ±0.002	0.001 ±0.001	0.008 ±0.004	0.002 ±0.002	0.061 ±0.009	0.004 ±0.003	0.005 ±0.002	0.003 ±0.002

Appendix B. (continued)

Xuan Loc	**XL-1**		**XL-3**		**XL-5**		**XL-7**	
Type	R		F		R		F	
Mineral	Cpx	Opx	Cpx	Opx	Cpx	Opx	Cpx	Opx
	n = 9	-	n = 5	n = 5	n = 4	n = 5	n = 4	n = 5
Ti	1329 ±305	-	1550 ±39	445.9 ±30.5	175.3 ±33.1	77.87 ±2.41	2817 ±953	689.7 ±170.5
Rb	0.006 ±0.015	-	0.002 ±0.012	-	0.519 ±0.995	0.002 ±0.008	0.005 ±0.015	-
Sr	138.7 ±12.9	-	90.05 ±1.58	0.214 ±0.324	56.39 ±9.78	0.324 ±0.376	54.19 ±38.06	0.629 ±1.04
Y	8.49 ±0.40	-	15.50 ±0.46	0.439 ±0.046	2.06 ±0.50	0.083 ±0.020	14.27 ±3.16	0.900 ±0.351
Zr	17.63 ±1.71	-	23.44 ±0.75	0.549 ±0.078	12.17 ±1.52	0.433 ±0.057	17.07 ±2.01	0.916 ±0.446
Nb	0.008 ±0.003	-	0.105 ±0.007	0.001 ±0.002	0.190 ±0.091	0.009 ±0.004	0.039 ±0.044	0.006 ±0.003
La	4.57 ±1.24	-	1.40 ±0.08	0.020 ±0.037	5.10 ±1.58	0.030 ±0.031	0.696 ±0.661	0.009 ±0.019
Ce	15.27 ±2.01	-	4.73 ±0.11	0.055 ±0.095	10.60 ±3.44	0.051 ±0.041	2.76 ±1.84	0.034 ±0.054
Pr	2.58 ±0.22	-	0.749 ±0.015	0.007 ±0.010	1.05 ±0.40	0.006 ±0.004	0.524 ±0.200	0.006 ±0.009
Nd	13.48 ±1.19	-	3.69 ±0.07	0.026 ±0.032	3.35 ±1.24	0.017 ±0.014	3.28 ±0.51	0.046 ±0.061
Sm	4.16 ±0.23	-	1.48 ±0.07	0.013 ±0.012	0.626 ±0.233	0.008 ±0.006	1.37 ±0.14	0.028 ±0.023
Eu	1.31 ±0.08	-	0.584 ±0.017	0.011 ±0.014	0.192 ±0.065	0.003 ±0.002	0.567 ±0.066	0.012 ±0.010
Gd	3.56 ±0.18	-	2.08 ±0.09	0.020 ±0.006	0.464 ±0.146	0.010 ±0.005	1.86 ±0.34	0.050 ±0.040
Tb	0.444 ±0.025	-	0.379 ±0.013	0.006 ±0.002	0.064 ±0.021	0.003 ±0.002	0.351 ±0.077	0.013 ±0.009
Dy	2.28 ±0.13	-	2.94 ±0.11	0.060 ±0.006	0.366 ±0.113	0.018 ±0.004	2.61 ±0.52	0.113 ±0.063
Ho	0.358 ±0.020	-	0.606 ±0.034	0.015 ±0.001	0.072 ±0.016	0.005 ±0.001	0.558 ±0.132	0.034 ±0.013
Er	0.836 ±0.059	-	1.84 ±0.08	0.074 ±0.008	0.245 ±0.033	0.018 ±0.004	1.60 ±0.39	0.124 ±0.044
Tm	0.106 ±0.009	-	0.267 ±0.016	0.013 ±0.003	0.041 ±0.008	0.006 ±0.002	0.231 ±0.065	0.028 ±0.007
Yb	0.616 ±0.050	-	1.64 ±0.05	0.129 ±0.019	0.326 ±0.025	0.045 ±0.011	1.57 ±0.44	0.240 ±0.066
Lu	0.086 ±0.007	-	0.225 ±0.022	0.025 ±0.002	0.055 ±0.003	0.010 ±0.001	0.213 ±0.071	0.044 ±0.011
Hf	0.774 ±0.067	-	0.660 ±0.027	0.015 ±0.002	0.271 ±0.037	0.014 ±0.004	0.563 ±0.103	0.041 ±0.017
Pb	0.592 ±0.361	-	0.123 ±0.027	0.003 ±0.002	0.424 ±0.405	0.016 ±0.005	0.077 ±0.025	0.006 ±0.003
Th	0.954 ±0.371	-	0.036 ±0.017	0.008 ±0.007	0.848 ±0.315	0.016 ±0.010	0.009 ±0.005	0.004 ±0.003
U	0.359 ±0.108	-	0.010 ±0.004	0.007 ±0.005	0.259 ±0.036	0.010 ±0.005	0.005 ±0.004	0.003 ±0.002

Appendix B. (continued)

Xuan Loc	**XL-8**		**XL-9**		**XL-11**		**XL-14**	
Type	F		F		R		F	
Mineral	Cpx	Opx	Cpx	Opx	Cpx	Opx	Cpx	Opx
	n = 5	n = 5	n = 5	n = 5	n = 6	n = 4	n = 5	n = 5
Ti	4811 ±523	1289 ±177	2696 ±205	709.7 ±45.8	218.7 ±13.1	79.50 ±3.06	4036 ±123	688.4 ±78.2
Rb	0.007 ±0.009	0.003 ±0.010	0.052 ±0.068	-	0.297 ±0.662	-	0.006 ±0.015	0.004 ±0.013
Sr	81.71 ±1.80	0.433 ±0.867	71.05 ±9.32	0.354 ±0.567	46.66 ±3.49	0.249 ±0.297	28.67 ±5.10	0.058 ±0.075
Y	19.33 ±0.86	1.27 ±0.49	19.33 ±0.88	0.593 ±0.061	1.64 ±0.13	0.089 ±0.059	23.95 ±0.50	0.545 ±0.052
Zr	36.03 ±2.18	2.14 ±0.95	28.26 ±1.85	0.767 ±0.120	12.54 ±1.00	0.394 ±0.066	20.85 ±0.52	0.428 ±0.093
Nb	1.54 ±0.09	0.017 ±0.016	0.012 ±0.005	0.004 ±0.001	0.434 ±0.677	0.003 ±0.001	0.011 ±0.010	0.000 ±0.001
La	5.81 ±0.12	0.038 ±0.076	3.47 ±3.02	0.027 ±0.051	3.33 ±0.83	0.028 ±0.037	1.42 ±1.91	0.004 ±0.003
Ce	14.64 ±0.17	0.092 ±0.178	7.25 ±5.00	0.045 ±0.081	6.24 ±1.60	0.058 ±0.055	2.63 ±2.55	0.011 ±0.012
Pr	1.94 ±0.07	0.013 ±0.025	0.906 ±0.355	0.005 ±0.005	0.619 ±0.171	0.006 ±0.004	0.470 ±0.187	0.001 ±0.002
Nd	8.87 ±0.35	0.080 ±0.126	4.34 ±0.80	0.016 ±0.015	2.28 ±0.56	0.021 ±0.015	3.53 ±0.47	0.007 ±0.009
Sm	2.42 ±0.16	0.028 ±0.030	1.88 ±0.09	0.013 ±0.006	0.410 ±0.081	0.004 ±0.005	1.81 ±0.05	0.008 ±0.003
Eu	0.911 ±0.015	0.013 ±0.014	0.716 ±0.019	0.007 ±0.002	0.125 ±0.020	0.002 ±0.001	0.722 ±0.043	0.003 ±0.000
Gd	2.86 ±0.12	0.062 ±0.050	2.66 ±0.11	0.022 ±0.007	0.331 ±0.064	0.008 ±0.006	2.74 ±0.05	0.018 ±0.005
Tb	0.495 ±0.037	0.013 ±0.008	0.485 ±0.014	0.008 ±0.001	0.046 ±0.008	0.002 ±0.001	0.503 ±0.016	0.006 ±0.001
Dy	3.53 ±0.22	0.121 ±0.042	3.63 ±0.11	0.078 ±0.019	0.276 ±0.043	0.011 ±0.003	3.86 ±0.15	0.060 ±0.018
Ho	0.761 ±0.059	0.042 ±0.017	0.753 ±0.032	0.021 ±0.004	0.058 ±0.007	0.004 ±0.001	0.854 ±0.035	0.021 ±0.004
Er	2.29 ±0.08	0.163 ±0.046	2.28 ±0.13	0.097 ±0.011	0.195 ±0.017	0.016 ±0.006	2.51 ±0.05	0.083 ±0.015
Tm	0.332 ±0.007	0.035 ±0.007	0.332 ±0.023	0.022 ±0.004	0.036 ±0.002	0.004 ±0.001	0.350 ±0.016	0.020 ±0.002
Yb	2.21 ±0.18	0.315 ±0.064	2.07 ±0.09	0.190 ±0.035	0.285 ±0.038	0.039 ±0.009	2.35 ±0.09	0.158 ±0.017
Lu	0.305 ±0.018	0.067 ±0.006	0.307 ±0.024	0.034 ±0.004	0.047 ±0.009	0.009 ±0.001	0.335 ±0.024	0.035 ±0.005
Hf	0.929 ±0.114	0.061 ±0.029	1.00 ±0.05	0.034 ±0.006	0.237 ±0.023	0.005 ±0.001	0.846 ±0.018	0.022 ±0.005
Pb	0.527 ±0.073	0.015 ±0.011	0.229 ±0.089	0.014 ±0.004	0.134 ±0.045	0.003 ±0.002	0.245 ±0.233	0.010 ±0.017
Th	0.400 ±0.083	0.008 ±0.012	1.14 ±0.94	0.025 ±0.042	0.488 ±0.068	0.014 ±0.011	0.370 ±0.554	0.010 ±0.003
U	0.113 ±0.036	0.005 ±0.004	0.379 ±0.355	0.010 ±0.008	0.135 ±0.027	0.007 ±0.005	0.110 ±0.151	0.005 ±0.003

Appendix B. (continued)

Xuan Loc	**XL-15**		**XL-16**		**XL-18**		**XL-19**	
Type	F		F		F		F	
Mineral	Cpx	Opx		Opx	Cpx	Opx	Cpx	Opx
	n = 5	n = 5	n = 5	n = 5	n = 6	n = 4	n = 5	n = 4
Ti	2032 ±62	447.8 ±41.3	2606 ±129	574.6 ±28.2	4613 ±276	877.9 ±101.0	3301 ±135	655.6 ±19.0
Rb	0.087 ±0.158	-	0.095 ±0.173	0.016 ±0.019	0.013 ±0.016	0.003 ±0.008	0.009 ±0.009	0.006 ±0.009
Sr	57.36 ±1.63	0.480 ±0.910	21.36 ±2.30	0.302 ±0.323	48.68 ±0.84	0.071 ±0.076	56.57 ±1.63	0.251 ±0.111
Y	15.58 ±0.31	0.462 ±0.080	17.46 ±0.36	0.982 ±0.070	24.54 ±1.29	0.882 ±0.135	19.99 ±1.47	0.701 ±0.073
Zr	16.53 ±0.45	0.395 ±0.120	11.74 ±0.58	0.538 ±0.075	31.74 ±3.37	1.07 ±0.13	19.83 ±1.04	0.643 ±0.084
Nb	0.122 ±0.015	0.001 ±0.002	0.102 ±0.034	0.012 ±0.014	0.830 ±0.232	0.009 ±0.003	0.374 ±0.029	0.006 ±0.004
La	0.829 ±0.011	0.001 ±0.003	1.96 ±1.08	0.060 ±0.074	2.17 ±0.07	0.001 ±0.001	0.739 ±0.043	0.003 ±0.002
Ce	2.75 ±0.07	0.008 ±0.007	3.84 ±2.14	0.143 ±0.165	6.21 ±0.18	0.005 ±0.002	2.44 ±0.08	0.014 ±0.006
Pr	0.474 ±0.017	0.002 ±0.001	0.449 ±0.197	0.016 ±0.017	1.03 ±0.04	0.002 ±0.001	0.484 ±0.020	0.003 ±0.002
Nd	2.78 ±0.06	0.003 ±0.004	2.31 ±0.64	0.076 ±0.077	6.12 ±0.25	0.018 ±0.005	3.38 ±0.24	0.022 ±0.013
Sm	1.12 ±0.03	0.006 ±0.002	1.13 ±0.11	0.028 ±0.020	2.30 ±0.09	0.014 ±0.003	1.51 ±0.10	0.012 ±0.007
Eu	0.465 ±0.009	0.002 ±0.001	0.527 ±0.026	0.011 ±0.006	0.854 ±0.028	0.009 ±0.004	0.592 ±0.028	0.007 ±0.002
Gd	1.77 ±0.04	0.012 ±0.007	1.95 ±0.07	0.040 ±0.019	3.15 ±0.16	0.033 ±0.006	2.25 ±0.16	0.030 ±0.006
Tb	0.348 ±0.011	0.005 ±0.001	0.403 ±0.016	0.011 ±0.002	0.571 ±0.040	0.010 ±0.002	0.428 ±0.020	0.009 ±0.003
Dy	2.72 ±0.05	0.053 ±0.013	3.06 ±0.05	0.109 ±0.009	4.12 ±0.14	0.095 ±0.013	3.15 ±0.15	0.095 ±0.008
Ho	0.607 ±0.018	0.016 ±0.005	0.686 ±0.036	0.032 ±0.005	0.902 ±0.038	0.031 ±0.002	0.698 ±0.032	0.026 ±0.004
Er	1.84 ±0.06	0.073 ±0.013	2.05 ±0.09	0.123 ±0.011	2.64 ±0.12	0.119 ±0.015	2.08 ±0.07	0.107 ±0.015
Tm	0.267 ±0.010	0.015 ±0.002	0.305 ±0.013	0.029 ±0.004	0.386 ±0.022	0.024 ±0.003	0.299 ±0.011	0.023 ±0.003
Yb	1.76 ±0.05	0.155 ±0.023	2.11 ±0.08	0.257 ±0.018	2.47 ±0.20	0.259 ±0.027	1.99 ±0.09	0.186 ±0.016
Lu	0.250 ±0.007	0.028 ±0.003	0.297 ±0.013	0.053 ±0.003	0.350 ±0.015	0.048 ±0.011	0.279 ±0.016	0.034 ±0.003
Hf	0.532 ±0.013	0.014 ±0.006	0.501 ±0.014	0.029 ±0.007	1.02 ±0.09	0.037 ±0.007	0.678 ±0.038	0.027 ±0.005
Pb	0.131 ±0.062	0.004 ±0.006	0.161 ±0.043	0.014 ±0.007	0.097 ±0.015	0.007 ±0.002	0.061 ±0.016	0.009 ±0.003
Th	0.034 ±0.007	0.002 ±0.001	0.372 ±0.173	0.030 ±0.027	0.109 ±0.015	0.004 ±0.002	0.057 ±0.011	0.007 ±0.003
U	0.009 ±0.001	0.003 ±0.002	0.094 ±0.031	0.009 ±0.006	0.018 ±0.004	0.006 ±0.006	0.019 ±0.004	0.004 ±0.002

Appendix B. (continued)

Xuan Loc	**XL-20**					
Type	F					
Mineral	Cpx	Opx	**Standards**	**NIST 610**	**BHVO-2G**	**NIST 616**
	n = 5	n = 3		n = 27	n = 27	n = 27
Ti	2545 ±343	583.8 ±2.9	Ti	468.6 ±20.1	16277±1789	5.61 ±1.02
Rb	0.039 ±0.051	0.003 ±0.014	Rb	419.2 ±4.6	9.36 ±0.66	0.105 ±0.017
Sr	62.50 ±24.53	0.037 ±0.006	Sr	511.9 ±6.0	394.2 ±7.3	42.03 ±0.77
Y	15.43 ±0.47	0.533 ±0.030	Y	471.5 ±17.7	24.88 ±2.07	0.027 ±0.004
Zr	13.38 ±1.30	0.431 ±0.031	Zr	460.5 ±18.9	172.4 ±14.4	0.095 ±0.014
Nb	0.079 ±0.011	0.003 ±0.001	Nb	482.2 ±10.5	18.20 ±0.77	0.022 ±0.005
La	2.36 ±1.74	0.002 ±0.001	La	441.4 ±9.1	15.40 ±0.65	0.029 ±0.002
Ce	4.72 ±2.83	0.004 ±0.002	Ce	456.5 ±4.4	37.19 ±0.67	0.030 ±0.002
Pr	0.575 ±0.198	0.001 ±0.001	Pr	441.2 ±6.7	5.10 ±0.19	0.015 ±0.002
Nd	2.99 ±0.31	0.007 ±0.005	Nd	436.2 ±12.8	26.70 ±7.91	0.020 ±0.006
Sm	1.24 ±0.04	0.011 ±0.004	Sm	460.9 ±13.7	6.21 ±0.39	0.017 ±0.005
Eu	0.476 ±0.025	0.004 ±0.000	Eu	441.0 ±9.4	2.02 ±0.07	0.016 ±0.003
Gd	1.80 ±0.06	0.024 ±0.005	Gd	442.8 ±14.6	6.07 ±0.37	0.018 ±0.005
Tb	0.350 ±0.011	0.007 ±0.001	Tb	435.9 ±14.3	0.883 ±0.054	0.014 ±0.002
Dy	2.65 ±0.07	0.069 ±0.013	Dy	452.5 ±16.3	5.39 ±0.35	0.023 ±0.007
Ho	0.577 ±0.014	0.019 ±0.002	Ho	464.2 ±16.3	0.984 ±0.067	0.015 ±0.003
Er	1.84 ±0.08	0.085 ±0.006	Er	465.8 ±17.0	2.59 ±0.17	0.019 ±0.005
Tm	0.267 ±0.012	0.017 ±0.004	Tm	462.8 ±17.7	0.335 ±0.020	0.014 ±0.002
Yb	1.69 ±0.08	0.179 ±0.013	Yb	473.2 ±15.3	2.04 ±0.16	0.023 ±0.006
Lu	0.249 ±0.013	0.033 ±0.005	Lu	454.5 ±18.1	0.276 ±0.022	0.014 ±0.002
Hf	0.493 ±0.036	0.020 ±0.004	Hf	422.2 ±17.3	4.30 ±0.29	0.014 ±0.003
Pb	0.354 ±0.242	0.007 ±0.004	Pb	436.7 ±7.6	1.93 ±0.78	1.79 ±0.07
Th	0.876 ±0.714	0.003 ±0.003	Th	470.3 ±16.9	1.26 ±0.06	0.026 ±0.004
U	0.219 ±0.173	0.003 ±0.001	U	462.1 ±10.8	0.425 ±0.028	0.072 ±0.006

APPENDIX C. T_{REE} Inversion Diagrams

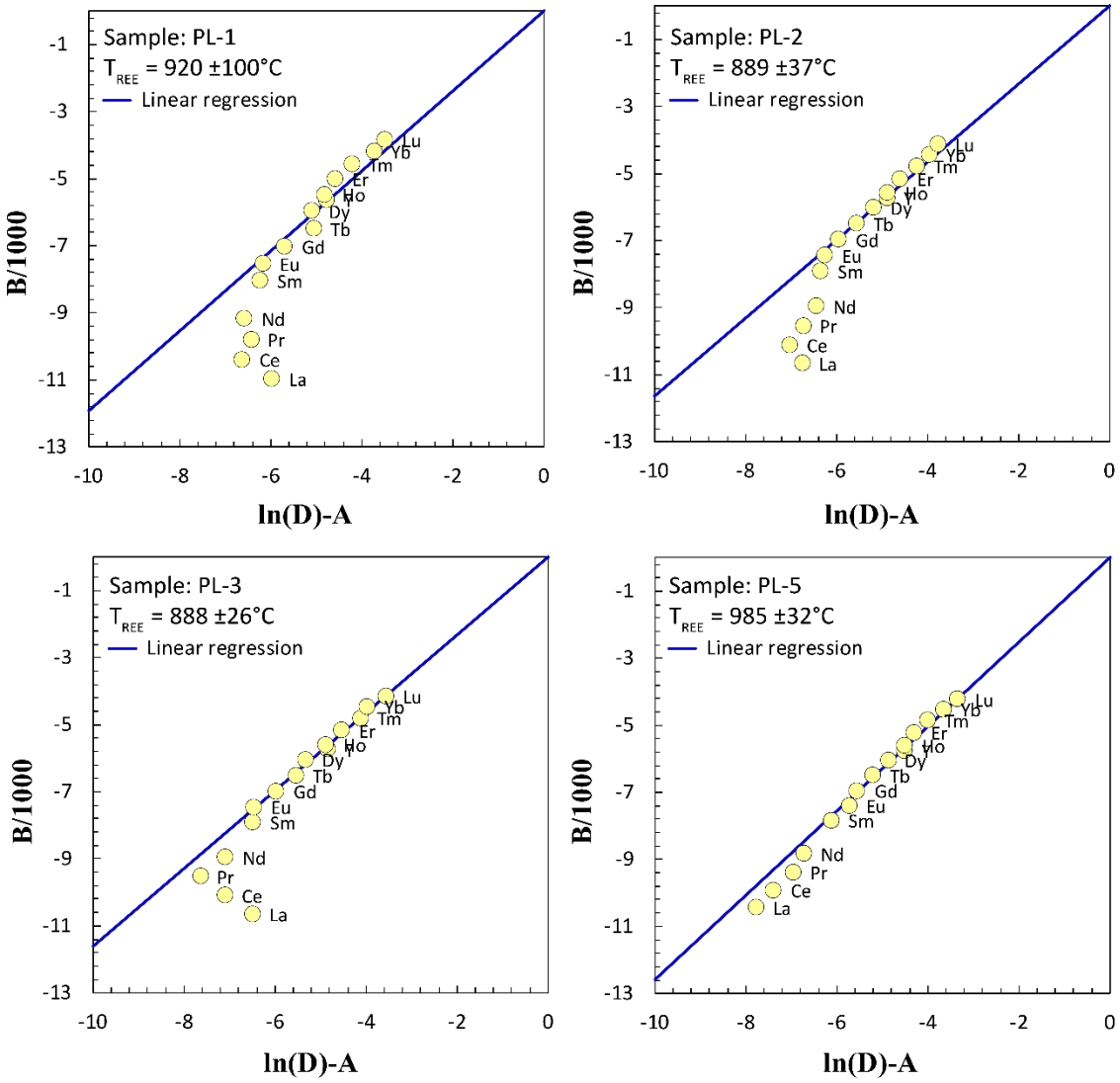
Sample: PL-1
T REE = 920 ±100°C
Linear regression
Sample: PL-2
T REE = 889 ±37°C
Linear regression
Sample: PL-3
T REE = 888 ±26°C
Linear regression
Sample: PL-5
T REE = 985 ±32°C
Linear regression
B/1000
ln(D)-A
Lu
Yb
Tm
Er
Ho
Dy
Tb
Gd
Eu
Sm
Nd
Pr
Ce
La

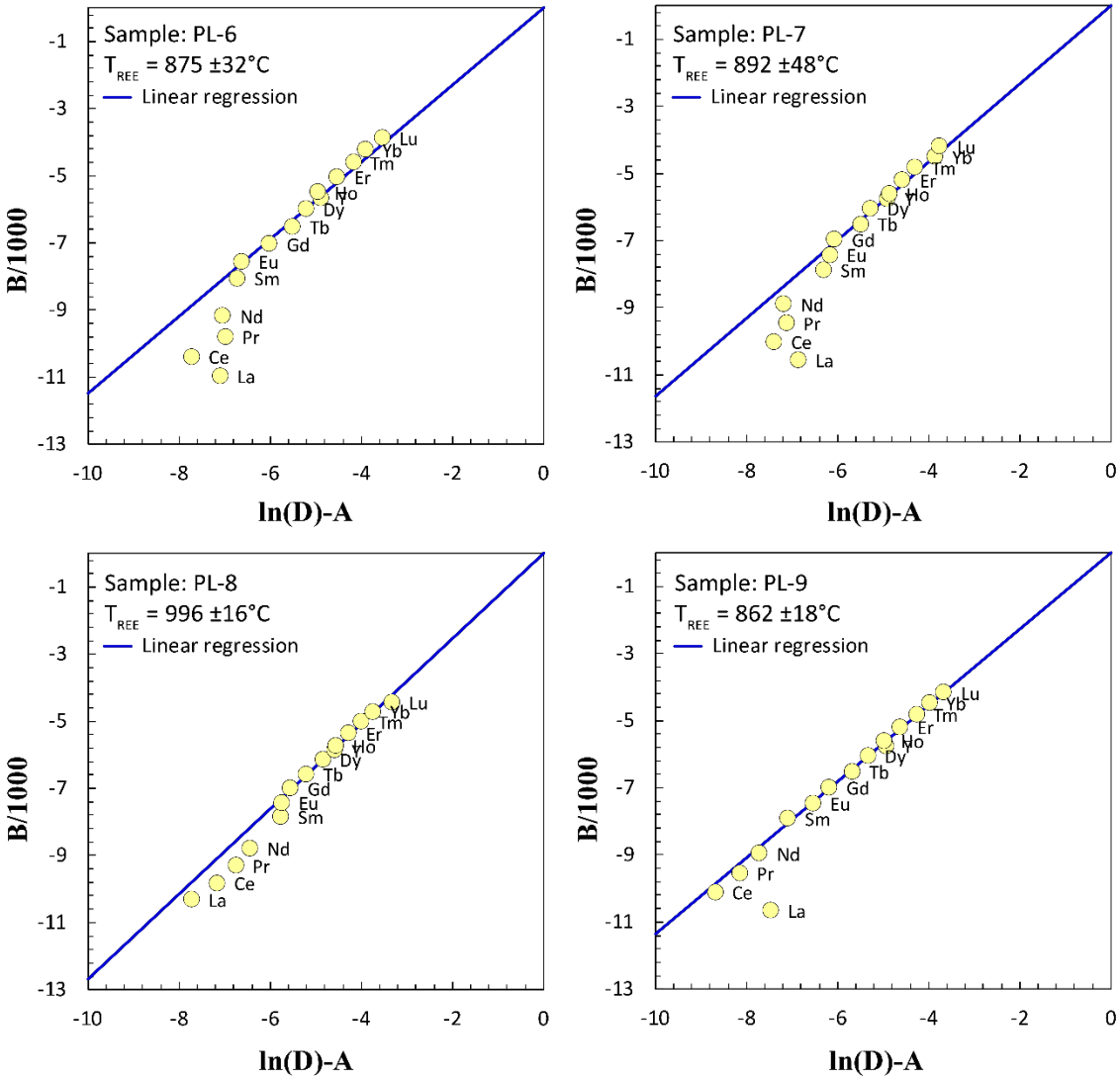
Sample: PL-6
T REE = 875 ±32°C
Linear regression
Lu
Yb
Tm
Er
Ho
Dy
Tb
Gd
Eu
Sm
Nd
Pr
Ce
La
B/1000
ln(D)-A
Sample: PL-7
T REE = 892 ±48°C
Linear regression
Lu
Yb
Tm
Er
Ho
Dy
Tb
Gd
Eu
Sm
Nd
Pr
Ce
La
B/1000
ln(D)-A
Sample: PL-8
T REE = 996 ±16°C
Linear regression
Lu
Yb
Tm
Er
Ho
Dy
Tb
Gd
Eu
Sm
Nd
Pr
Ce
La
B/1000
ln(D)-A
Sample: PL-9
T REE = 862 ±18°C
Linear regression
Lu
Yb
Tm
Er
Ho
Dy
Tb
Gd
Eu
Sm
Nd
Pr
Ce
La
B/1000
ln(D)-A

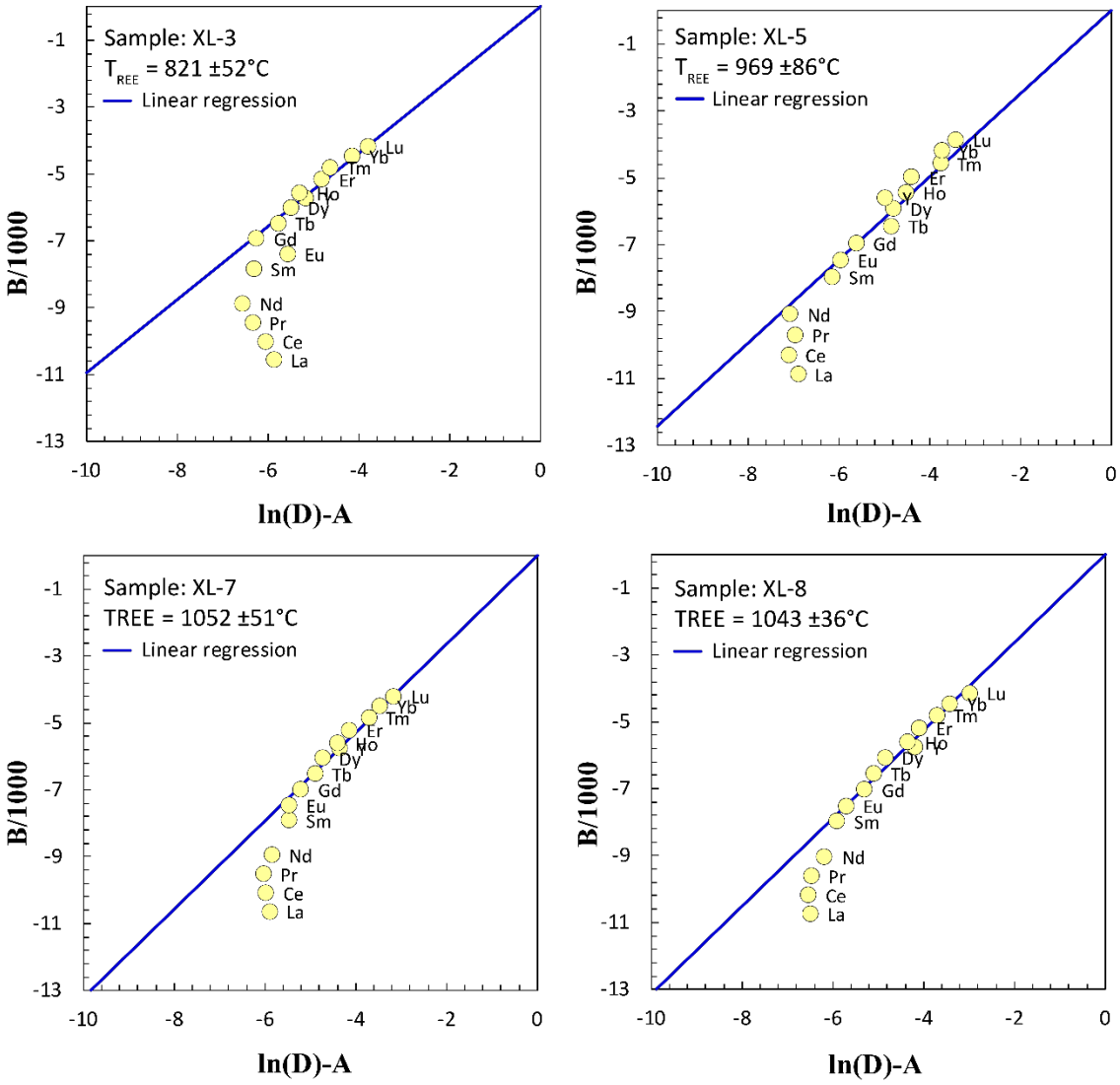
Sample: XL-3
T REE = 821 ±52°C
Linear regression
Sample: XL-5
T REE = 969 ±86°C
Linear regression
Sample: XL-7
TREE = 1052 ±51°C
Linear regression
Sample: XL-8
TREE = 1043 ±36°C
Linear regression
B/1000
ln(D)-A
Lu
Yb
Tm
Er
Ho
Dy
Tb
Gd
Eu
Sm
Nd
Pr
Ce
La

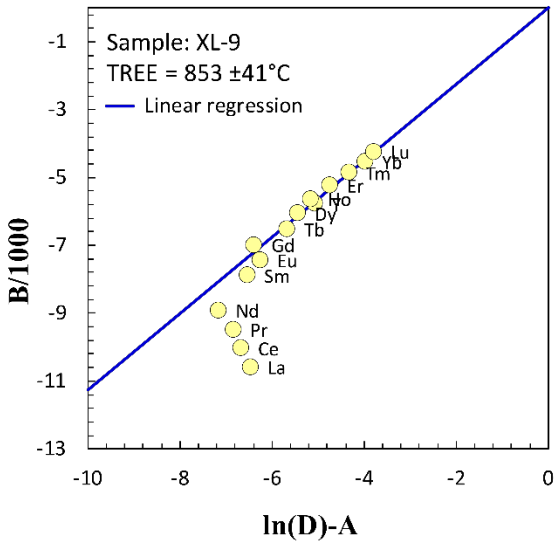
Sample: XL-9
TREE = 853 ±41°C
Linear regression
Lu
Yb
Tm
Er
Ho
Dy
Tb
Gd
Eu
Sm
Nd
Pr
Ce
La
B/1000
ln(D)-A

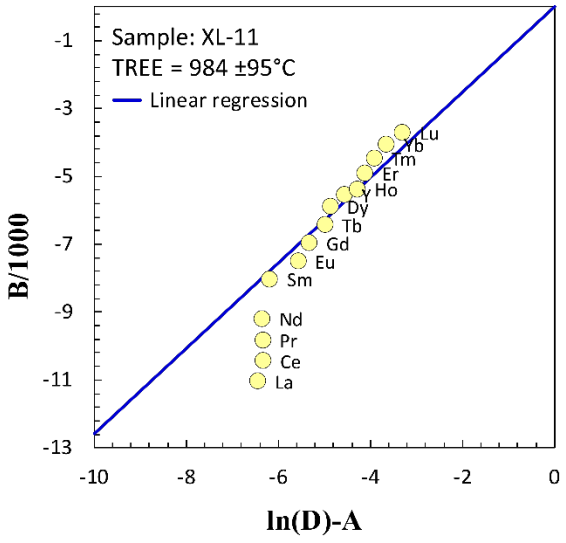
Sample: XL-11
TREE = 984 ±95°C
Linear regression
Lu
Yb
Tm
Er
Ho
Dy
Tb
Gd
Eu
Sm
Nd
Pr
Ce
La
B/1000
ln(D)-A

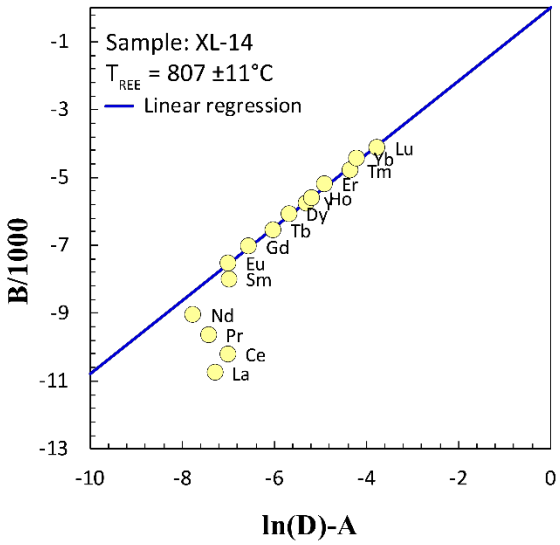
Sample: XL-14
T REE = 807 ±11°C
Linear regression
Lu
Yb
Tm
Er
Ho
Dy
Tb
Gd
Eu
Sm
Nd
Pr
Ce
La
B/1000
ln(D)-A

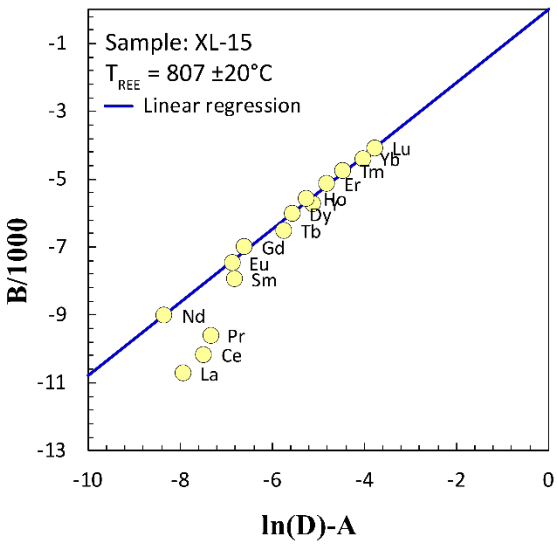
Sample: XL-15
T REE = 807 ±20°C
Linear regression
Lu
Yb
Tm
Er
Ho
Dy
Tb
Gd
Eu
Sm
Nd
Pr
Ce
La
B/1000
ln(D)-A

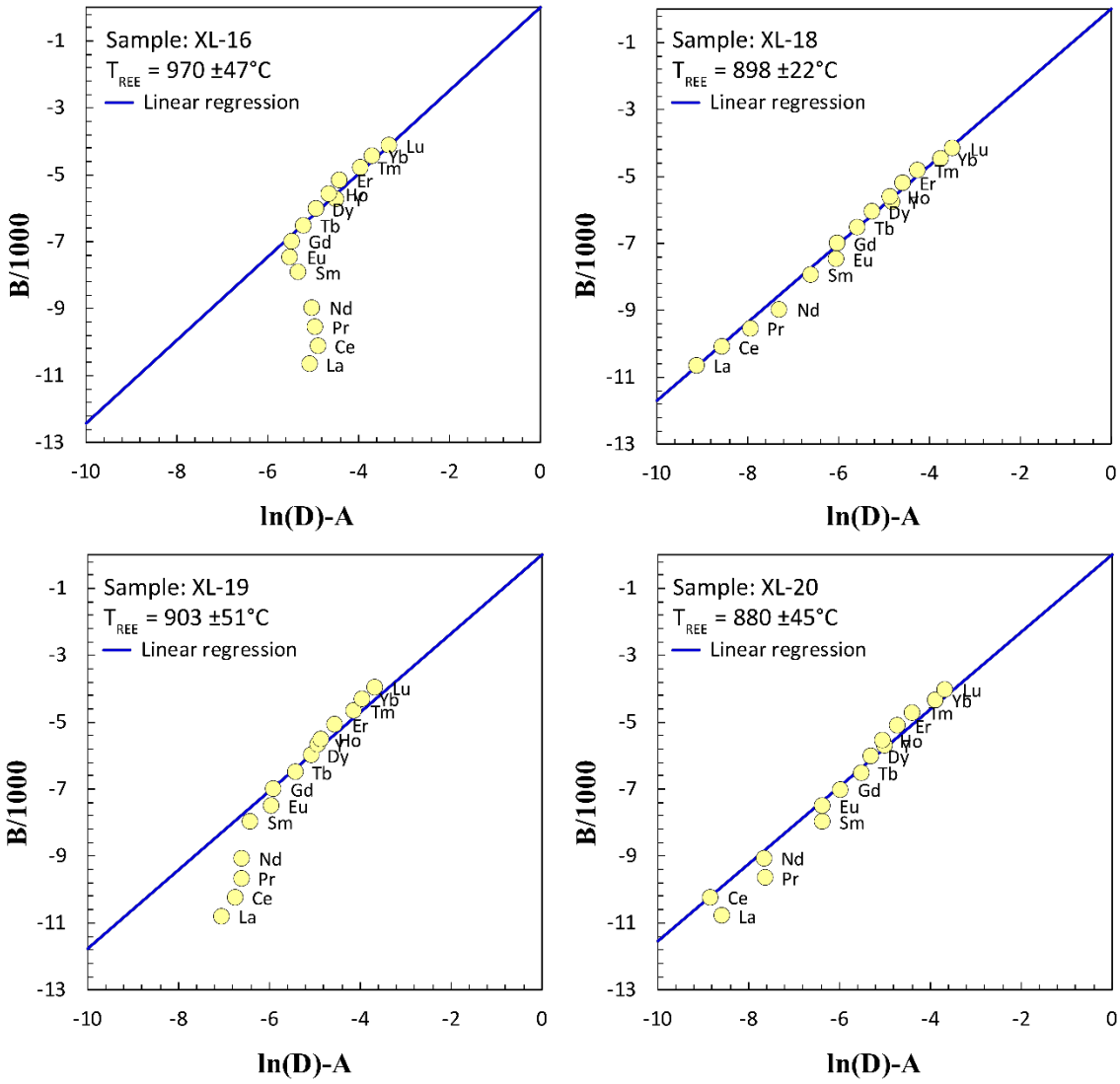
Sample: XL-16
T REE = 970 ±47°C
Linear regression
Sample: XL-18
T REE = 898 ±22°C
Linear regression
Sample: XL-19
T REE = 903 ±51°C
Linear regression
Sample: XL-20
T REE = 880 ±45°C
Linear regression
B/1000
ln(D)-A
-1
-3
-5
-7
-9
-11
-13
-10
-8
-6
-4
-2
0
La
Ce
Pr
Nd
Sm
Eu
Gd
Tb
Dy
Ho
Er
Tm
Yb
Lu